Master's thesis

Studies on the Sensitivity of Multi-PMT Optical Modules to the Energy Spectrum of MeV Supernova Neutrinos for Future IceCube Extensions

submitted by
Florian Sprenger

— January 2019 —

"*In a sky of a million stars it flickers, flickers*"

One More Light - Linkin Park

Contents

1 Preface

Astronomy is one of the oldest and most captivating fields of science in human history. Massive ancient constructions as Stonehenge or the pyramids of Giza are linked, besides cultural and social rituals, to astronomic functions as well. The mathematical description of astronomical events gave us laws of gravitation which led us to the knowledge of our place within the universe, its origin, content and possible development in the future. Also observations of stars with many different telescopes on Earth and in space which record the whole range of the electromagnetic spectrum are possible. To reach deeper insights into galactic and extragalactic objects there is a need for new messengers.

A milestone for deeper insights was the discovery of the neutron star merger via gravitational waves and a gamma-ray burst in 2017 [1] which led to the quote *"that the era of multi-messenger astronomy has officially begun"*. To support this statement, in October 2018 the evidence for a coincidence between the flaring of the gamma-ray blazar TXS 0506+056 and a new member in multi-messenger astronomy - a high-energetic neutrino was reported [2, 3]. Indeed the neutrino was already well known in multi-messenger astronomy. In 1987, the electromagnetic radiation of SN1987A was discovered. It was a type II supernova (SN) meaning the progenitor star's core collapsed under its own gravitational pressure. Linked to this observation there were in total 25 antineutrinos found in the neutrino detecntors of Kamiokande-II, IMB and Baksan [4, 5, 6].

With this direct observation of SN neutrinos, theoretical SN models confirmed that neutrinos carry away $\sim 99\%$ of the nascent energy in a core collapse [7]. Furthermore, the 25 detected neutrinos are consistent with the estimation of models that predicted a neutrino luminosity of $\sim 10^{58}$ neutrinos. The fact that *only* 25 of these SN1987A neutrinos were detected shows directly how difficult it is to do neutrino astronomy. Nevertheless there is still much information yield from a SN neutrino flux as the inner process during the core collapse, the energy distribution and the ordering of neutrino masses are still unknown. Therefore, the aim is to collect more neutrinos and distinguish them with more sensitivity for future supernovae events.

An extremely high amount of neutrinos from galactic and extragalactic

sources, as for example $6.5 \times 10^{10}\,\mathrm{cm}^{-2}\,\mathrm{s}^{-1}$ neutrinos from the Sun [8], in a wide energy spectrum reaches the Earth every second and most of them traverse it without any interaction. On one hand this small interaction rate makes neutrinos quite mysterious since some of their properties are still unknown. On the other hand a proper detection of neutrinos would give direct information about their sources because neutrinos are not absorbed or deflected in their path. To find out still unknown neutrino properties as well as the sources of the highest energetic neutrinos in the universe, detectors in different sizes were developed in various location on Earth.

One large neutrino telescopes is IceCube. It is located at the Amundson-Scott station at the South Pole and detects neutrinos via Cherenkov radiation in the ice. Its framework consists of 86 strings with each holding 60 Digital Optical Modules (DOMs) in a volume of $1\,\mathrm{km}^3$ ice. IceCube's main target is the detection and path reconstruction of high-energetic neutrinos. Additionally, IceCube is able to identify supernovae by a collective rise over all DOMs and therefore it is part of the Supernova Early Warning Systems (SNEWS) [9]. But, apart from supernova identification, IceCube is not capable of filtering further information as the SN neutrino energy spectrum.

The future Icecube extensions, IceCube-Upgrade and IceCube-Gen2, will give the opportunity to employ new optical modules. One of the new proposed modules is the multi-PMT Optical Module (mDOM) [10]. It consists of 24 photomultipliers (PMTs) which are spherically located in one module which allows to measure local coincidences. These coincidences give the mDOM the potential to be more sensitive towards low energetic events and motivate the investigation of the mDOM sensitivity to the energy spectrum of SN neutrinos.

2 Neutrinos & Supernovae

When we talk about neutrinos (ν) and supernovae (SN), we consider nearly massless elementary particles [11] and extremely heavy ($\geq 8\,\mathrm{M}_\odot$) objects [12]. One may wonder how these antipodes work together. In this chapter the properties of both, as well as the mutual influence on each other are studied.

2.1 Neutrino Properties

The story of the neutrino began in 1930 when Wolfgang Pauli postulated a new particle[1] to explain the continuous β^- decay spectrum without violating the law of energy conservation. This problem had already given the physics community a lot of headache for more than 20 years [14]. The first direct detection of such a particle was done more than 20 years later in 1956 [15], when physicists were able to see the interaction of an electron antineutrino $\bar{\nu}_e$ in a cloud chamber experiment. Today three neutrino families are known; electron, muon (ν_μ) [16], and tau neutrino (ν_τ) [17].
These three particles belong to the lepton family in the standard model of particle physics. Their counterparts are electron, muon and tau with which they build up the three families of leptons. All elementary particles in the standard model have their own antiparticle with same mass but opposite electric charge. The antineutrinos are denoted by $\bar{\nu}$.
Since neutrinos[2] are neutrally charged leptons. They only interact via weak interaction with other particles as seen in the β^- decay. The cross section of the weak interaction allows them to travel through nearly all matter without any change of direction because most neutrinos simply do not interact with this matter. That means detected neutrinos point directly towards the source if it is managed to identify the neutrinos' direction which makes detection and reconstruction a major challenge for experimenters in the field of neutrino astronomy.
Another unique characteristic of neutrinos is the ability to oscillate

[1] In his famous letter to the "radioactive ladies and gentlemen" he firstly named it "neutron" until the neutron itself was discovered two years later [13].

[2] If not explicitly announced from now on neutrinos and antineutrinos are always considered when denoting "neutrinos".

(including the Mikheyev–Smirnov–Wolfenstein [18] effect) which solved the more than 40 years lasting solar neutrino problem [19]. Deduced from that observation, neutrinos hold masses which is not included in the standard model of particle physics. The mass of one neutrino flavor is the superposition of mass eigenstates. Since it was merely possible to measure the squared difference of the mass eigenstates, it is still unknown if the ordering of these mass eigenstates follows $m_1 \leq m_2 \leq m_3$ ("normal hierarchy") or $m_3 \leq m_1 \leq m_2$ ("inverted hierarchy"). Even though the study of SN neutrinos could help to set new constrains in hierarchy ordering, oscillation of neutrinos is not considered in these studies.

2.2 Sources of Neutrinos

Similar to photons, neutrinos can be found over a large energetic spectrum. Fig. 2.1 shows a compilation of the fluxes of different neutrino sources versus their energy. On the outer edges hypothetical neutrino sources and their fluxes are predicted. The cosmological neutrinos, also known as relic neutrinos, are the neutrino counterpart to the cosmological microwave background (CMB). Those are assumed to hold an energy $\sim 1.9\,\mathrm{K}$ (corresponding to an energy range from μeV to meV) since they decoupled even earlier than photons in the early universe ($\sim 1\,\mathrm{s}$ after the Big Bang) [20]. On the high-energy border there are the fluxes of cosmogenic neutrinos which are associated with ultra-high energetic cosmic rays (UHECRs) interacting with the CMB and decoupling these highest-energetic neutrinos (from PeV up to EeV) [20]. Neutrinos in this energy range were detected for the first time in 2013 by IceCube [21]. From TeV to PeV, neutrinos from active galactic nuclei (AGN) dominate. Evidence for this assumption is provided by the detection of a neutrino with a flaring blazar, an AGN with one relativistic jet pointing towards Earth, in 2018 by IceCube in conjunction with Fermi-LAT and MAGIC [2]. Neutrinos with lower energy (from $\sim 100\,\mathrm{MeV}$ to TeV) are directly generated in our atmosphere, named atmospheric neutrinos. Those are byproducts of cosmic ray interactions producing weakly-decaying

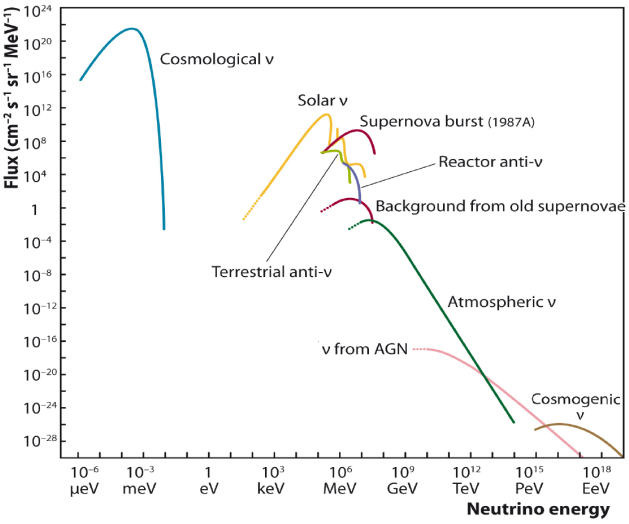

Figure 2.1: Fluxes from natural and reactor neutrino sources. Figure taken from [20].

mesons[22]. In the region of $\sim 10\,\mathrm{MeV}$ there is an accumulation of different neutrino sources. The main component in this energy region is a burst of SN neutrinos such as SN1987A [4]. Those SN neutrinos are of main interest in this thesis. Besides, slightly less energetic ($\sim 1\,\mathrm{keV}$ to $1\,\mathrm{MeV}$) neutrinos from the sun also have a non-negligible flux at the SN neutrino energies. Especially solar neutrinos from the decay

$$^{8}\mathrm{B} \rightarrow ^{8}\mathrm{Be}^{*} + e^{-} + \nu_e \tag{2.1}$$

can have energies up to $18\,\mathrm{MeV}$ [8]. Around that region are also lower fluxes of neutrinos from nuclear reactors, as well as terrestrial neutrinos from β-decays in the earth crust[23] which are not considered in this work. The same holds for background neutrinos from old SN.

2.3 Neutrino Driven Supernovae

The life of each star begins as a gas cloud of light elements, mostly hydrogen. Due to gravitation the cloud compresses the temperature in the star rises until atoms collide at such high energies that they overcome the Coulomb barrier and undergo nuclear fusion. This fusion of hydrogen to helium releases energy due to the larger binding energy per nucleon (see Fig. 2.2) which stabilizes the newborn star against the gravitational forces. The longest stable time period of a star begins which is called the *main-sequence stage*. But while the hydrogen burning of our Sun lasts for $\sim 10 \times 10^{9}\,\mathrm{yr}$, the hydrogen burning phase of a star $> 8\,\mathrm{M}_{\odot}$ lasts only for some tens of millions of years [25]. At some time the released fusion energy is not sufficient anymore to stabilize the star, because nearly all hydrogen was used. Due to its compression a higher temperature arises and a subsequent nuclear burning phase begins. The burning phases are:

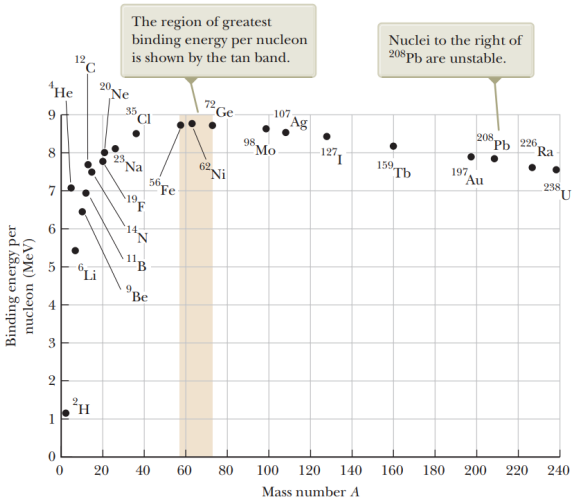

Figure 2.2: Binding energy per nucleon versus mass number for nuclei that lie along the line of stability. Figure taken from [24].

$$\text{hydrogen} \rightarrow \text{helium} \rightarrow \text{carbon} \rightarrow \text{neon} \rightarrow \text{oxygen} \rightarrow \text{silicon} \rightarrow \text{iron}.$$

For further reading on the total evolution of a massive star see [26].

As shown in Fig. 2.2 iron possesses one of the greatest binding energy per nucleon. Any further burning phase cannot gain any more energy which is necessary to stabilize the star again. Depending on their mass not all stars reach the phase of silicon burning and cool down becoming a white dwarf. Stars with masses larger than $8\,M_\odot$ usually reach this last burning phase and undergo a different type of death depending on their total mass. In these studies only stars from $8\,M_\odot$ up to $30\,M_\odot$ are considered which die in a core-collapsing supernova (SN), more detailed type II SN, and where a neutron star is created [27].

Before its death this type of star features an onion-shell structure which is exemplary shown in Fig. 2.3. If the iron core of the star exceeds a critical mass around the Chandrasekhar limit of $\sim 1.44\,M_\odot$ the gravitational pressure overwhelms and the inner core contracts [28].

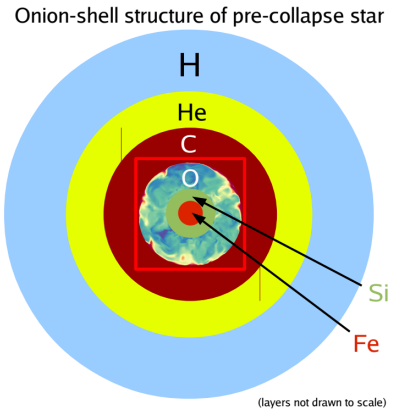

Figure 2.3: Onion-shell structure of a SN progenitor star before the stellar core collapse. All different burning phases are still active in different layers of the star. The red box marks the inner core of the star which a closer look is taken at during the core collapse. Figure taken from [12].

Through the compression (Fig. 2.4 left) its temperature and density rise inside the iron core. When the temperature exceeds $\sim 10 \times 10^9\,\mathrm{K}$ there is blackbody radiation $\sim 3\,\mathrm{MeV}$ which include photons with enough energy ($\sim 8\,\mathrm{MeV}$) to desintegrate the nuclei into α particles, neutrons and protons called photodisintegration.

$$\gamma + {}^{56}\mathrm{Fe} \rightarrow 13\alpha + 4n \tag{2.2}$$

$$\gamma + \alpha \rightarrow 2p + 2n \tag{2.3}$$

This process drains even more energy from the core which accelerates the collapse further. Eventually the density of

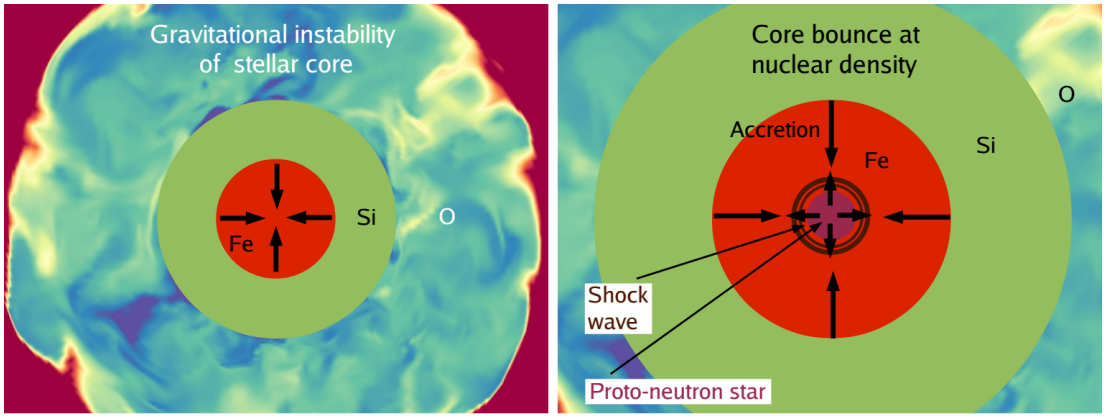

Figure 2.4: Beginning of the SN by the compression of the progenitor star due to gravitational instability (left) and core bounce when the inner core reaches the nuclear saturation density (right). Figure taken from [12].

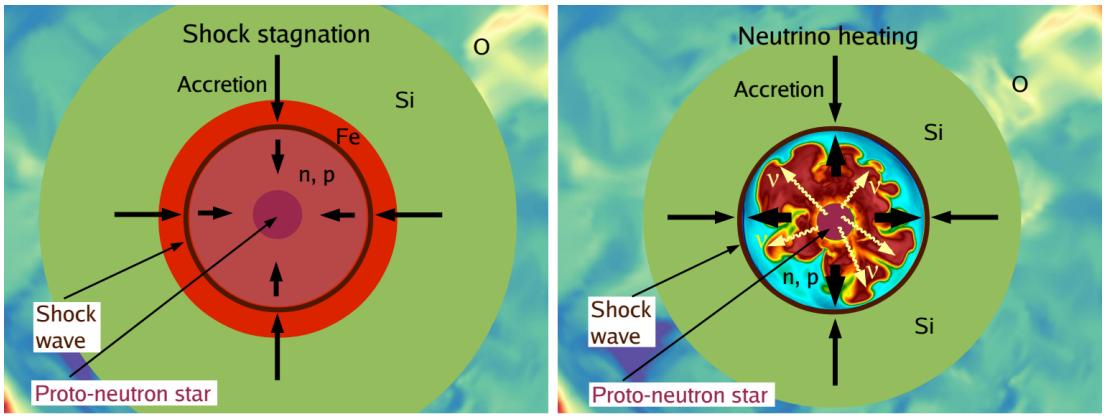

Figure 2.5: Stagnation of the bounce shock due to missing energy (left) and accretion phase with neutrino heating of infalling matter (right). The mushroom-like structures around the inner core stand for the entropy distribution. Figure taken from [12].

the core raises until the electrons behave like a degenerated Fermi gas where no two fermions can be in the same quantum state. At a density above $\sim 10^9\,\mathrm{g\,cm^{-3}}$, electrons reach energies to capture on free protons and heavy nuclei (above 2.25 MeV) [12].

$$e^- + p \rightarrow \nu_e + n \tag{2.4}$$

$$e^- + (\mathrm{A,Z}) \rightarrow \nu_e + (\mathrm{A,Z\text{-}1}) \tag{2.5}$$

The degenerated electron gas as main source of pressure in the inner core decreases by these processes called neutronization since the resulting particles are neutrinos, neutrons and neutron-rich nuclei. It leads to another acceleration of the collapse nearly to free fall. The density rises to more than $10^{12}\,\mathrm{g\,cm^{-3}}$ which means the diffusion time of neutrinos (due to coherent scattering on nuclei) becomes larger than the collapse time [29]. Thus, a huge amount of neutrinos produced by the neutronization is trapped inside the core. The implosion of the inner core stops suddenly when the central density reaches the nuclear saturation density ($\rho_0 \approx 2.7 \times 10^{14}\,\mathrm{g\,cm^{-3}}$) where the strongly repulsive part of the strong force occurs. The collapsing core overshoots this density and the infalling matter bounces off the most inner core. The expansion of the rebound core creates a shock wave (Fig. 2.4 right).

The shock wave disintegrate the iron nuclei as in Eq. 2.2 and 2.3 which destroys all burning phases in the inner core. The proto-neutron star (PNS) is born. The disintegration decelerates the shock wave. Furthermore, it decreases the density inside the PNS that neutrinos can escape in a luminous flash called the neutrino burst. Both processes take away enough energy from the shock wave until its outward velocity fades to zero (Fig. 2.5 left). The bounce is held up and turns into an accretion shock. The PNS itself gets stabilized due to the pressure of the degenerate electron gas which

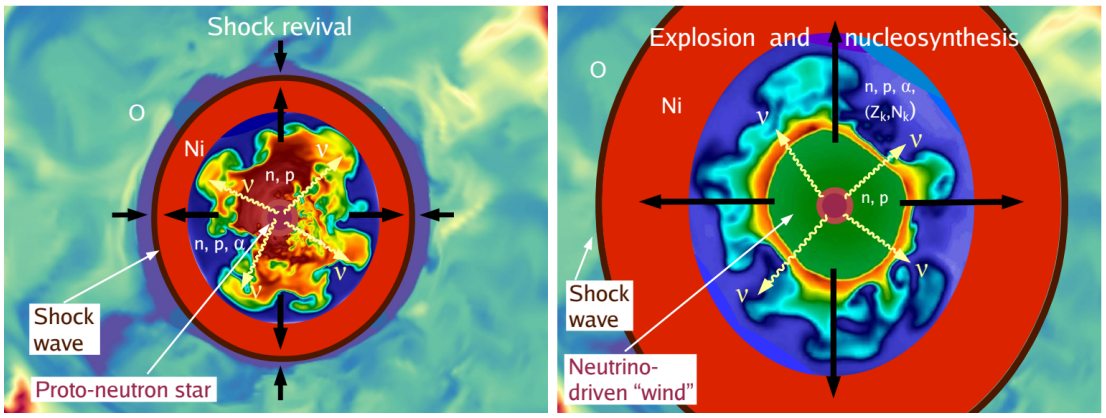

Figure 2.6: Revival of the shock bounce (left) and outward acceleration of the neutrino-powered SN shock front (right). Figure taken from [12].

cannot escape from the PNS because the electrons' free mean path is larger than the PNS's radius. Some escaping electron neutrinos and antineutrinos which are formed at the so-called "neutrinosphere" [29] get absorbed by free neutrons and protons

$$\nu_e + n \rightarrow p + e^-, \tag{2.6}$$
$$\bar{\nu}_e + p \rightarrow n + e^+, \tag{2.7}$$

closer to the shock surface (Fig. 2.5 right). This transfers new energy to the stalled shock, a mechanism called neutrino heating [30], and raises the postshock pressure in this region. At the same time neutrinos and antineutrinos of all flavors are produced in the surrounding plasma via

$$e^+ + e^- \rightarrow \nu_{e,\nu,\tau} + \bar{\nu}_{e,\nu,\tau}. \tag{2.8}$$

If the neutrino heating is strong enough the outwards going shock revives and the SN explosion finally takes place (Fig. 2.6 left). For this the energy deposition of neutrinos causes a negative entropy gradient through which different non-radial fluid instabilities can occur in the heated layer [12]. The high-entropy mushroom-like structures are outlined in the postshock region of Fig. 2.5 right. The instabilities assist the neutrino heating mechanism in several ways. Convection fluxes for example can transport hot material out of the heated layer and replace it by cooler material falling down. This hydrodynamic process performs the SN explosion in bubbles of matter which have enough energy to escape. Less and less material obstructs this process.

Neutrinos not only helped the star to explode but also cool down the new born neutron star with the so-called neutrino-driven wind [12]. Proton- or neutron-rich nuclei can be created in this wind and undergo nucleosynthesis (Fig. 2.6 right). The whole collapse only takes about 10 s but radioactive nuclei power the electromagnetic radiation of the SN remnant for many

years.
In contrast to the electromagnetic radiation which originates from the outer layers of the SN, the detection of SN neutrinos provide diverse information from the dense core of the SN explosion. One example is the measurement of the rotation of a SN and its progenitor star [31]. The main motivation for the study of the energy spectrum of SN neutrinos are the unclear thermodynamics and equation of state (EoS) of the inner core during the SN explosion. Therefore, the character of the energy spectrum is investigated further in the next section.

2.4 Supernova Burst Models & Energy Spectra

Since the SN explosion process is not totally well understood yet, different models are used. In this work two different progenitor stars are used whose data was kindly provided by H.-T. Janka [32]. The heavy case contributed by a star of $27.0\,\mathrm{M}_\odot$ resulting in a neutron star of $1.77\,\mathrm{M}_\odot$ and a light case from a star of $9.6\,\mathrm{M}_\odot$ giving a NS of $1.36\,\mathrm{M}_\odot$. Both cases give a upper and lower limit since stars with more than $\sim 30\,\mathrm{M}_\odot$ collapse into black holes and stars with less than $\sim 8\,\mathrm{M}_\odot$ produce white dwarfs [32]. Furthermore, one EoS needs to be used which is the *LS220 (Lattimer-Swesty's)* EoS [33] in this work. For these cases from the data of the luminosity of SN neutrinos and antineutrinos the flux Φ of particles reaching the Earth can be calculated with the expression

$$\Phi(t) = \frac{1}{4\pi d^2} \cdot \frac{L(t)}{\langle E \rangle(t)}, \tag{2.9}$$

where d is the distance of the SN to the observer (if not differently denoted, usually a SN in a distance of 10 kpc is assumed in these studies). The flux for different SN neutrinos and antineutrinos for the time after the core bounce are given in Fig. 2.7.

When different times of the SN explosion are considered (Fig. 2.8), it is clear that SN neutrinos do not follow a simple blackbody spectrum, because the neutrinos get partially absorbed (as shown in Eq. 2.6 & 2.7) and scattered during the transport to the PNS surface. Therefore a modified energy spectrum is assumed [36, 35] by the form

$$f_\alpha(E) = \left(\frac{E}{\langle E \rangle}\right)^\alpha \cdot \exp\left(-(\alpha+1)\frac{E}{\langle E \rangle}\right) \tag{2.10}$$

where $\langle E \rangle$ is the mean energy and α, obtained from

$$\frac{\langle E^2 \rangle}{\langle E \rangle^2} = \frac{2+\alpha}{1+\alpha}, \tag{2.11}$$

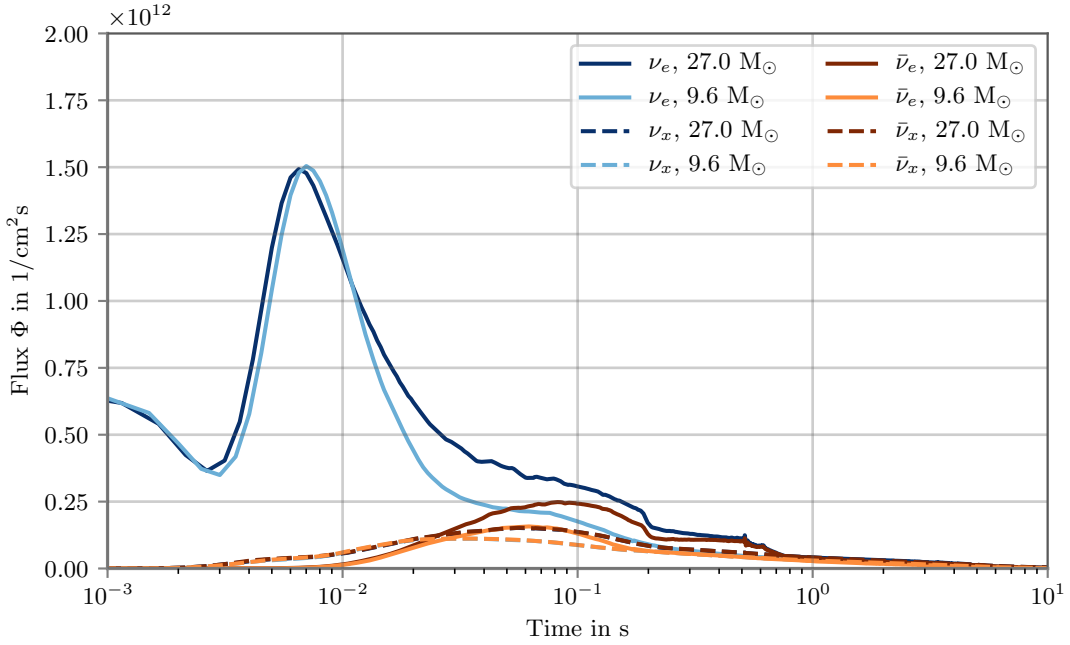

Figure 2.7: Flux of SN neutrinos as a function of the time after the core bounce. Solid lines are for electron neutrinos (blueish colors) and electron antineutrinos (reddish color), while dashed lines are for muon/tau neutrinos and antineutrinos ($x = \mu, \tau$). Two cases (heavy and light progenitor star) are implemented. Data kindly provided by *H.-T. Janka* [32].

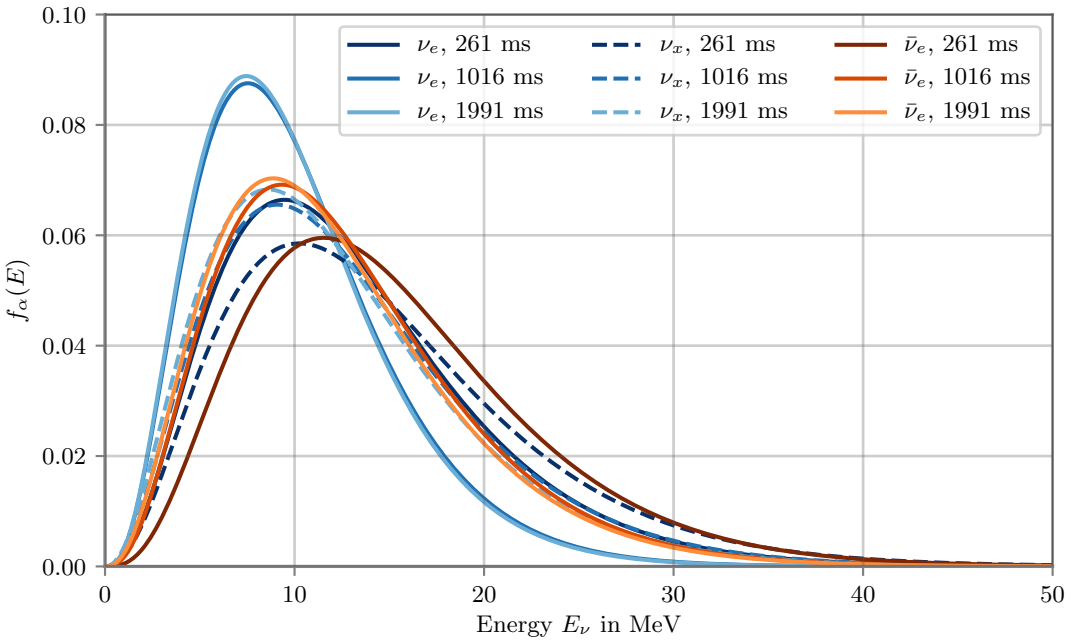

Figure 2.8: Energy distributions of SN neutrinos for a $15\,M_\odot$ progenitor star from [34] at different times after the core bounce. Solid lines are for electron neutrinos (blueish colors) and electron antineutrinos (reddish color), while dashed lines are for muon/tau neutrinos ($x = \mu, \tau$). Data taken from [35].

the spectral pinching parameter, where $\langle E^2 \rangle$ is the mean of the squared energies.

Eq. 2.11 shows how the mean energy and α are correlated. Since the energy spectrum of SN neutrinos is parameterized in both, mean energy $\langle E \rangle$ and α, it is necessary to investigate the sensitivity towards the mean energy $\langle E \rangle$ as well as towards the α parameter at the same time. Therefore the development of the mean energy (Fig. 2.9) and the development of the α parameter (Fig. 2.10) during the SN explosion are shown here.

Particle	**Progenitor Star**	$\langle E \rangle$	α
ν_e	$27\,\mathrm{M}_\odot$	9.2 MeV	2.8
	$9.6\,\mathrm{M}_\odot$	8.1 MeV	2.8
ν_x	$27\,\mathrm{M}_\odot$	10.9 MeV	2.3
	$9.6\,\mathrm{M}_\odot$	9.7 MeV	2.5
$\bar{\nu}_e$	$27\,\mathrm{M}_\odot$	11.4 MeV	2.4
	$9.6\,\mathrm{M}_\odot$	10.0 MeV	2.5
$\bar{\nu}_x$	$27\,\mathrm{M}_\odot$	11.5 MeV	2.2
	$9.6\,\mathrm{M}_\odot$	10.1 MeV	2.5

Table 2.1: Table of the mean of $\langle E \rangle$ and α for neutrino and antineutrino types from a heavy ($27.0\,\mathrm{M}_\odot$) or a light ($9.6\,\mathrm{M}_\odot$) progenitor star.

Using Fig. 2.9 and Fig. 2.10 the mean of $\langle E \rangle$ and of α can calculated by integrating over for the 10 s SN burst and dividing by 10 s. The $\langle E \rangle$, α values for the different neutrino types are given in Tab. 2.1.

With the flux $\Phi(t)$, the mean energy $\langle E \rangle(t)$, and the α parameter $\alpha(t)$ there are all components that are needed to distinguish between different EoS as well as between different masses of progenitor stars.

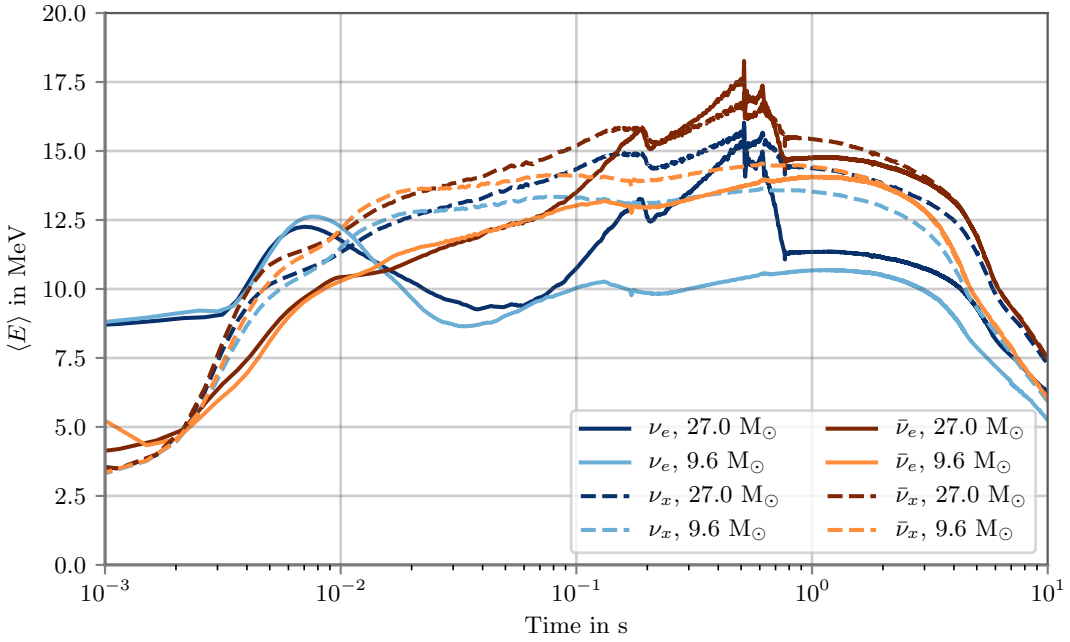

Figure 2.9: Mean energy as a function of the time after the core bounce. Solid lines are for electron neutrinos (blueish colors) and electron antineutrinos (reddish color), while dashed lines are for muon/tau neutrinos and antineutrinos ($x = \mu, \tau$). Two cases (heavy and light progenitor star) are implemented. Data kindly provided by *H.-T. Janka* [32].

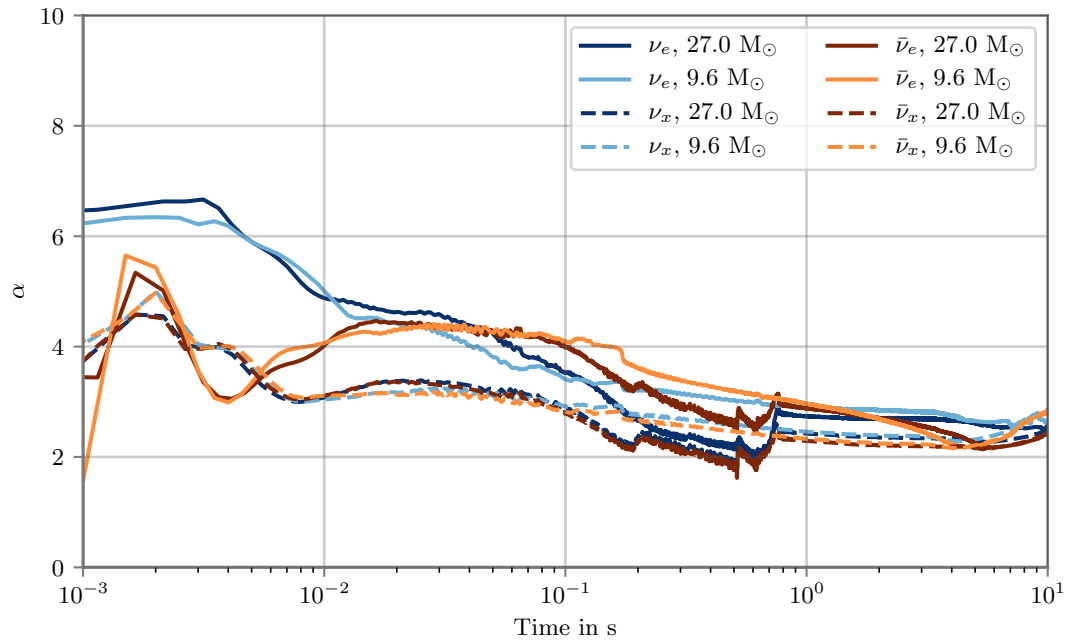

Figure 2.10: α parameter as a function of the time after the core bounce. Solid lines are for electron neutrinos (blueish colors) and electron antineutrinos (reddish color), while dashed lines are for muon/tau neutrinos and antineutrinos ($x = \mu, \tau$). Two cases (heavy and light progenitor star) are implemented. Data kindly provided by *H.-T. Janka* [32].

3 The IceCube Neutrino Telescope

Since neutrinos cannot be detected directly, the focus lays on the detection of secondary particles that are created in a neutrino interaction. These secondary particles can be detected in different ways. In this chapter the IceCube Neutrino Telescope, which uses Cherenkov radiation to detect secondary particles from neutrino interactions, is discussed. It is deployed in the arctic glacier at South Pole. Because only charged particles can produce Cherenkov radiation, one firstly needs to know how MeV neutrinos interact in ice to produce such charged secondary particles. In a further step future IceCube extensions and one proposed new optical module are introduced.

3.1 Interactions of MeV Neutrinos in Ice

As discussed in Sec. 2.1 neutrinos interact via the weak interaction with matter with the Z^0 boson as mediator for neutral current interactions and the W bosons as mediators for charged current interactions. Elastic scattering (ES) is possible for each particle interacting weakly, including neutrinos and antineutrinos of all flavours. ES of electron neutrinos with electrons is depicted in Fig. 3.1 once as a neutral current and once as a charged current interaction. Same as Fig. 3.1 it is for any other flavoured neutrino or antineutrino. The basic interaction is

$$\nu_e + e^- \rightarrow \nu_e + e^-. \tag{3.1}$$

It is possible with any of the 16 electrons of one H_2O molecule. The total cross section of ES is different for the neutrino

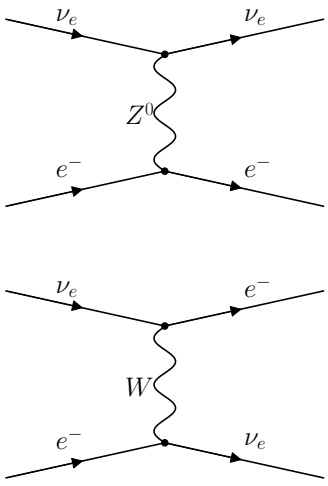

Figure 3.1: Feynman diagrams of electron neutrino scattering on electron. The upper one shows the case for a neutral current interaction, the lower one shows the case for a charged current interaction.

Process	**Total cross section $\sigma_{\mathbf{tot}}$**
$\nu_e + e^-$	$\sigma_{\text{tot}} = \frac{G_F^2 s}{4\pi}\left[\frac{1}{3}(1+2\sin^2\vartheta_W)+4\sin^4\vartheta_W\right]$ $\simeq 93\times10^{-46}\,\text{cm}^2\cdot s\,\text{MeV}^{-2}$
$\nu_x + e^-$	$\sigma_{\text{tot}} = \frac{G_F^2 s}{4\pi}\left[(1-2\sin^2\vartheta_W)+\frac{4}{3}\sin^4\vartheta_W\right]$ $\simeq 15\times10^{-46}\,\text{cm}^2\cdot s\,\text{MeV}^{-2}$
$\bar{\nu}_e + e^-$	$\sigma_{\text{tot}} = \frac{G_F^2 s}{4\pi}\left[\frac{1}{3}(1+2\sin^2\vartheta_W)+4\sin^4\vartheta_W\right]$ $\simeq 39\times10^{-46}\,\text{cm}^2\cdot s\,\text{MeV}^{-2}$
$\bar{\nu}_x + e^-$	$\sigma_{\text{tot}} = \frac{G_F^2 s}{4\pi}\left[\frac{1}{3}(1-2\sin^2\vartheta_W)+4\sin^4\vartheta_W\right]$ $\simeq 13\times10^{-46}\,\text{cm}^2\cdot s\,\text{MeV}^{-2}$

Table 3.1: Total neutrino-electron ES cross sections from [37].

and antineutrino flavours. They are derived in [37] and given in Tab. 3.1. The cross sections in this table are given with $h = c = 1$, where $G_F = 1.166\times10^{-11}\,\text{MeV}^{-2}$ is the Fermi constant, ϑ_W the weak mixing Weinberg angle, which will be taken as $\sin^2\vartheta_W = 0.231$, and s the total squared energy, which is in the laboratory frame $s = 2m_e\cdot E_\nu$.

Another interaction process with which only electron antineutrinos can interact in ice is the Inverse Beta Decay (IBD). The basic interaction is

$$\bar{\nu}_e + p \to n + e^+, \tag{3.2}$$

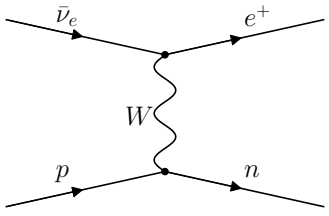

Figure 3.2: Feynman diagram of the Inverse Beta Decay

also depicted as Feynman diagram in Fig. 3.2. The IBD requires unbound protons, so the 2 protons of hydrogen in one H_2O molecule are contemplable. Assuming the proton being in rest, the electron antineutrino gives most of its energy to the positron while the neutron usually stays in the nucleus. Since the IBD and the common beta decay are totally symmetric the total cross section of this interaction for low-energetic antineutrinos is given by [38]:

$$\sigma_{\text{tot}} = \frac{2\pi^2/m_e^5}{f_{p.s.}^R\tau_n}(E_\nu-\Delta)\sqrt{(E_\nu-\Delta)^2-m_e^2} \tag{3.3}$$

with $h = c = 1$, where m_e is the positron mass, $f_{p.s.}^R = 1.7152$ the phase space factor, τ_n the neutron lifetime, $\Delta = m_n - m_p$ the difference of the neutron and proton mass, and E_ν the antineutrino energy. This total cross section is given for the interaction with a free nucleon but is nevertheless accurate for an interaction with a proton bound into a H_2O molecule [39].

The energy transfer between the electron antineutrino and the positron in the IBD is given in first order by [38]:

$$E_e^{(1)} = E_e^{(0)} \left(1 - \frac{E_\nu}{m_p}(1 - v_e \cos\theta\right) - \frac{(\Delta^2 - m_e^2)^2}{4m_p}, \tag{3.4}$$

where $E_e^{(0)} = E_\nu - \Delta$ is the zeroth order energy transfer, $v_e = \frac{\sqrt{E_e^2 - m_e^2}}{E_e}$ the velocity of the positron, and θ the angle between the incoming antineutrino and the outgoing positron.

To investigate which interaction rate it can be expected, the total cross sections is plotted σ_{tot} against the neutrino energy E_ν which is depicted in Fig. 3.3. The IBD has a much larger cross section than each of the ES processes, at least two magnitudes higher for the relevant energies than the ES of electron neutrinos. This affects the interaction rate of SN neutrinos. For this purpose the flux Φ (Fig. 2.7) is multiplied by the total cross section σ_{tot} for the mean energy $\langle E \rangle$ corresponding to the time and the density of target particles N_{target} which is given by:

$$N_{\text{target}} = \frac{\rho \cdot N_a \cdot n}{M}, M \tag{3.5}$$

where ρ is the density of ice, N_a the Avogadro constant, M the molar mass of H_2O and n the number of interaction partners per molecule for the different interactions which is 2 for IBD and 10 for ES. The expected event rate is depicted in Fig. 3.4.

Although the neutrino burst only consists of electron neutrinos, there is a higher event rate of electron antineutrinos due to the higher cross section of the IBD. Thus these studies consider firstly electron antineutrinos emitted from a SN. The total signal fraction of SN neutrinos for these introduced interactions and other occuring interactions in IceCube can be found in [39].

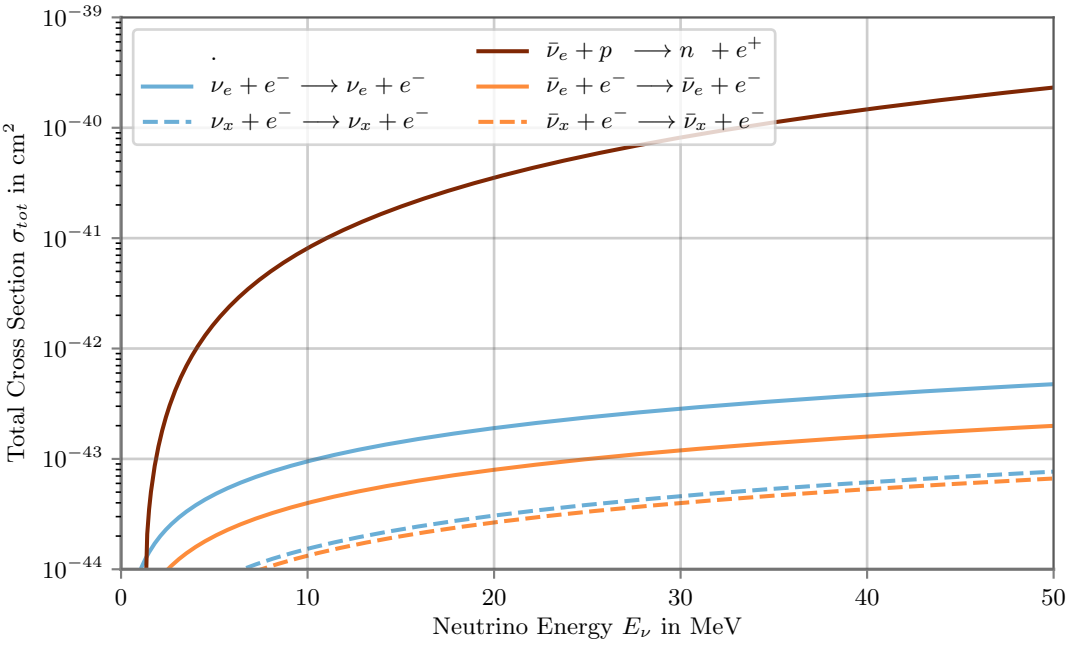

Figure 3.3: The total cross section σ_{tot} vs. the neutrino energy E_ν. The cross section of Electron Scattering (ES) of all flavoured neutrinos and antineutrinos as well as Inverse Beta Decay (IBD) of electron antineutrinos are depicted.

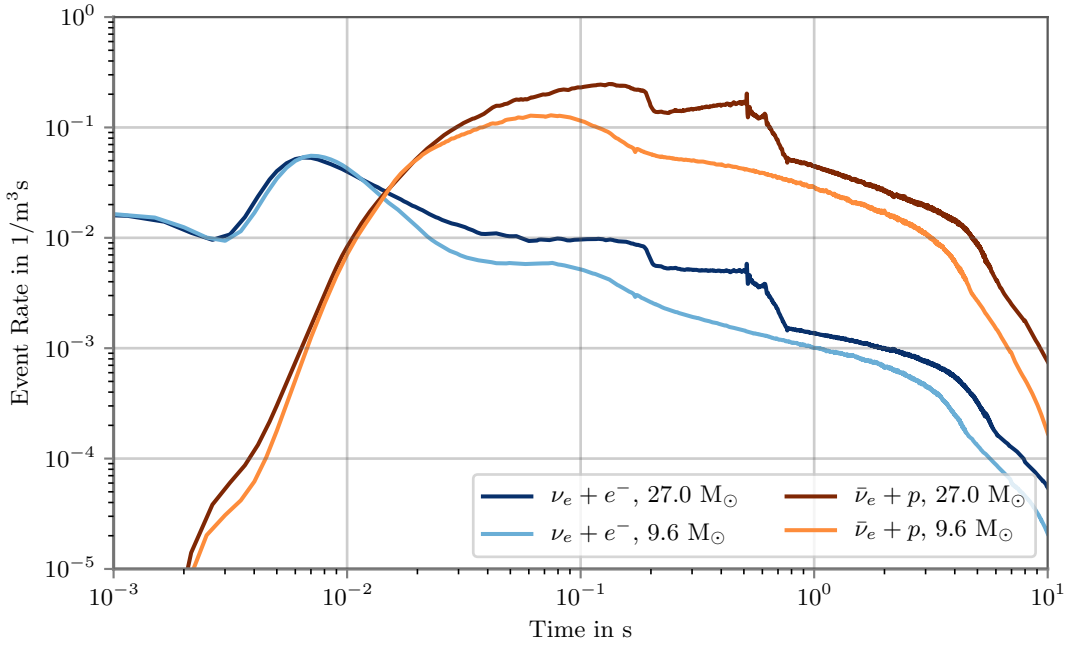

Figure 3.4: Event rate of SN electron neutrinos interacting via Electron Scattering (blueish lines) and electron antineutrinos interacting via Inverse Beta Decay (reddish lines) as a function of the time after the core bounce. Both cases (heavy and light progenitor star) are implemented

3.2 Cherenkov Detectors

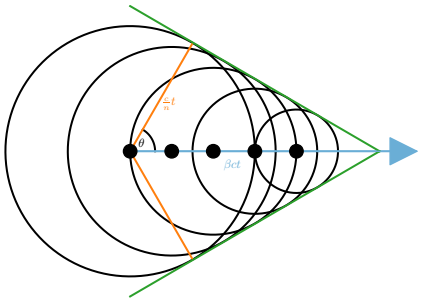

Figure 3.5: Sketch of Cherenkov radiation. The path of the positron (blue) is depicted creating waves (black). Those waves produce a shockwave (green). The radiation is emitted under the angle θ_C a Cherenkov cone (orange) is created.

When charged particles such as the positrons created in the IBD travel through dielectric medium such as ice the environment gets briefly polarized due to disturbance of the electromagnetic fields in the medium. These disturbances usually relax elastically back. If the charged particles travel with a velocity faster than the speed of light in that medium the disturbance cannot relax and the energy is released in a coherent shock wave of photons [40, 41]. This causes a light cone under a fixed angle θ_C as depicted in Fig. 3.5. The angle can directly be calculated [41]:

$$\cos\theta_C = \frac{\frac{c}{n}t}{\beta ct} = \frac{1}{n\beta} \tag{3.6}$$

where $\beta = \frac{v_p}{c}$ is the relativistic speed of the particle and n the refractive index of the surrounding medium. The spectrum of this effect and the number of emitted photons N_γ per unit length x can be approximated by the Frank-Tamm formula (derived in [10]):

$$\frac{d^2N_\gamma}{dxd\lambda} = \frac{2\pi\alpha}{\lambda^2}\cdot\left(1-\frac{1}{\beta^2n^2}\right) \tag{3.7}$$

with the wavelength λ, the fine structure constant $\alpha \approx \frac{1}{137}$, β and n as before.

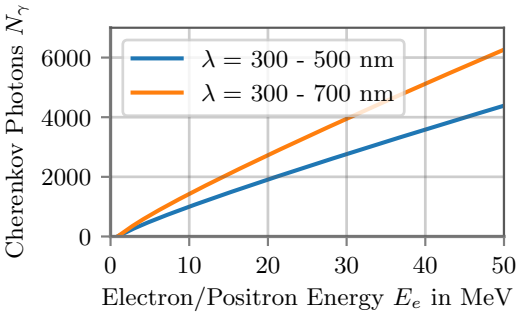

Figure 3.6: Amount of photons N_γ emitted by the Cherenkov effect from one positron in ice vs. the positron energy E_e. The orange line covers photons in the visible range (from 300 to 700 nm), the blue line covers higher energetic photons (from 300 to 700 nm).

To determine how many Cherenkov photons of which wavelength can be expected from a single positron induced by a SN electron antineutrino interaction in the ice, the Bethe formula [42] is used to estimate the length of the positron in which it creates Cherenkov photons and multiply it by Eq. 3.7. This is depicted in Fig. 3.6. Even from low energetic MeV neutrinos there is a sufficient number of photons to be detected. How the collection of Cherenkov radiation from SN

neutrino interactions is done in the IceCube Neutrino Observatory is part of the next two subchapters.

3.3 The IceCube Neutrino Observatory

The largest Cherenkov detector today is the IceCube Neutrino Observatory [43] with 1 km^3 antarctic ice as instrumented volume. A schematic layout of IceCube is given in Fig. 3.7 left. It consists of three parts: the IceCube Array, DeepCore and IceTop.

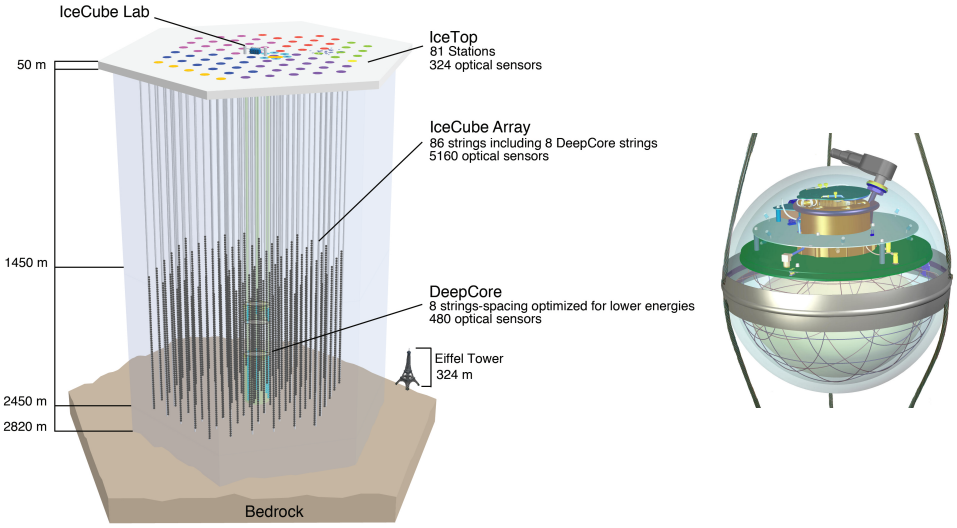

Figure 3.7: Schematic layout of the IceCube Neutrino Observatory with the IceCube Array, DeepCore and IceTop (left) & represantation of a digital optical module (DOM) with one photomultiplier facing downwards (right). Courtesy of the IceCube collaboration [44].

Its main part is the IceCube Array which consists of 86 strings equipped with in total 5160 digital optical modules (DOMs). These strings are drilled into the ice in between 1450 m and 2450 m below the surface. The DOM, which is schematically shown in Fig. 3.7 right, is situated in a borehole with refrozen ice. The main component of a DOM is its ~ 25 cm diameter photomultiplier (PMT) [45]. On one string the DOMs are separated by 17 m, while the strings are in a horizontal string distance of 125 m apart from each other. This configuration was chosen to detect astrophysical neutrinos in the energy range of TeV to PeV [43].

Eight of these strings with a total number of 480 DOMs belong to a denser array which is named DeepCore. Horizontally the strings are 72 m apart from each other, vertically the distance of modules goes down to 7 m. This

configuration allows a lower energy threshold down to 10 GeV for neutrinos interactions [46].

IceTop which is located at the surface consists of 81 stations close to the top of the strings. Each station consists of two ice-filled tanks with one DOM inside of the tank to form a km^2 sized array for air shower detection. Another task of IceTop is to serve as a veto for atmospheric muons entering the detection volume [47].

With those three components the IceCube Neutrino Observatory is a multipurpose experiment. Some of the scientific questions for IceCube are the detection of astrophyscial neutrinos [48] and the identification of their sources [2] as well as indirect detection of dark matter, studies of neutrino oscillation and detection of the neutrino burst from core-collapsing SNe [49]. It is discussed the SN detection in current IceCube in the next section.

3.4 Supernova Detection in IceCube

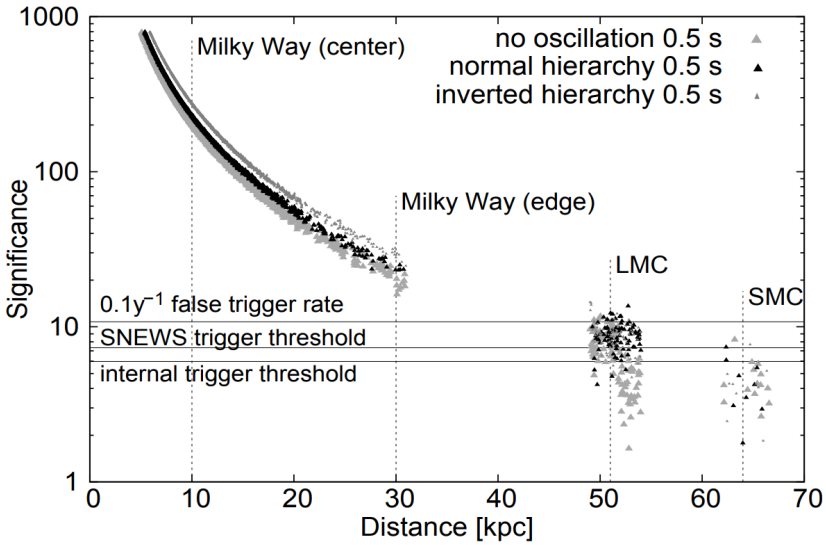

Figure 3.8: Significance of the IceCube Detector for SN versus the distance from SN simulations. Figure taken from [39].

Although the IceCube Array is optimized for high energetic neutrinos it is nevertheless possible to detect the outburst of a nearby SN (up to ~ 50 kpc distance [39]). Although secondary charged particles from MeV neutrinos travel 3 to 15 cm through ice before they have lost all their energy more than 1000 Cherenkov photons in the visible light range with a large fraction of higher energetic photons in the wavelength range of 300 to 500 nm were emitted as it was shown in Sec. 3.1 (see also Fig. 3.6). Those more energetic

photons travel more than 50 m and thereby have a higher probability to hit at least one DOM. This produces a rate of hits in all DOMs in the array which dominates the background noise [39]. The significance with which IceCube can identify a SN is depicted in Fig. 3.8.

Further information about a SN, like the direction or the energy spectra of SNe, is not obtainable with IceCube as a stand-alone neutrino detector. Via triangulation of the arrival time of SN neutrinos with other neutrino detectors the direction can be evaluated [52]. For neutrino spectra the idea is to measure coincidences of hits at neighbouring DOMs. After one DOM in the IceCube array was hit a time window of 150 ns opens and if a neighbouring DOM also gets hit by a photon this is called a "double coincidence". The ratio of double and triple coincident hits versus single hits gets used in a χ^2 fit to extract the $\langle E \rangle$ and α simultaneously [51]. An example of this method is depicted in Fig. 3.9.

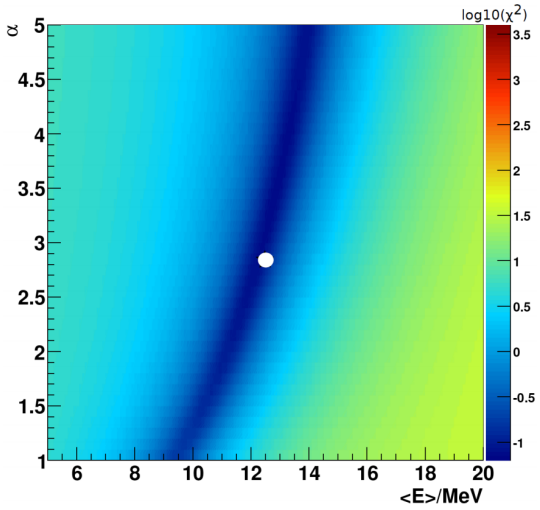

Figure 3.9: Map to determine the neutrino mean energy $\langle E \rangle$ and the pinching parameter α from an O-Ne-Mg 8.8 $M_\odot$ progenitor star [50] for IceCube using a χ^2 method. The input value ($\langle E \rangle$ = 12.6 MeV, α = 2.84) is denoted by a white circle. Figure taken from [51].

3.5 The IceCube-Upgrade & IceCube-Gen2

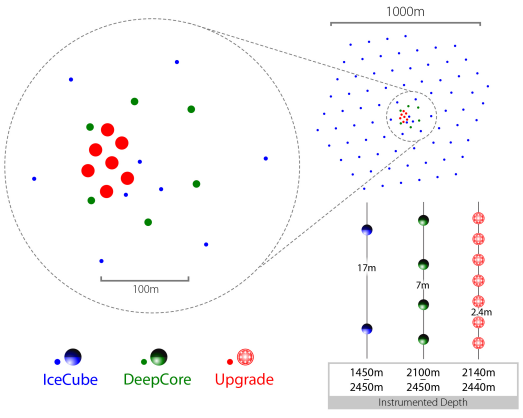

Figure 3.10: Layout of the new strings of the IceCube-Upgrade (red). Courtesy of the IceCube collaboration [53].

The IceCube Collaboration has plans for a larger, improved neutrino detector. The next extension to IceCube is the IceCube-Upgrade [53]. Its layout is depicted in Fig. 3.10. It contains 7 new strings inside of DeepCore, 25 m apart from each other. The 125 modules per string are proposed to have a 2.4 m horizontal spacing. In total IceCube will deploy 875 new modules in a depth between 2140 to 2440 m. The physics plan with these new strings is to dramatically

boost IceCube's sensitivity to lower neutrino energies ($< 10\,\mathrm{GeV}$). Furthermore, the increase of statistics for atmospheric neutrinos which are important to investigate neutrino oscillation and the enhancement of the directional sensitivity for astrophysical neutrinos are two further aims. New implemented calibration devices will also refine the calibration of the present DOMs and allow a reanalysis of IceCube's data to increase the discovery potential of neutrino sources.

Another proposed extension is IceCube-Gen2 [54]. One of the conceivable layouts is shown in Fig. 3.11. The major part is the expansion of the detector array also called the high-energy array (HEA) to $\sim 10\,\mathrm{km}^3$. To instrument this volume ~ 80 new strings, each with ~ 125 modules, are planed. This yields an array size of a total $\sim$ 10000 modules. The optimal spacing between two strings is ~ 240 to 300 m to maintain high efficiency to astrophysical neutrinos [54].

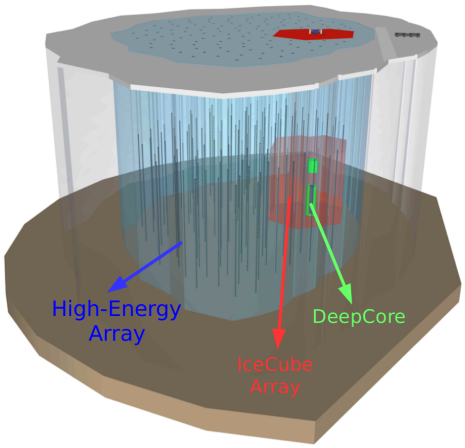

Figure 3.11: Layout of a proposed IceCube-Gen2 layout including the High-Energy Array (blue). Courtesy of the IceCube collaboration [44].

The extensions of the current IceCube detector opens up the possibility to apply new calibration methods and give the opportunity to deploy new, technologically advanced modules. One candidate module is described in the next section.

3.6 The multi-PMT Digital Optical Module (mDOM)

One of modules that will be used for the future IceCube extensions is the multi-PMT Digital Optical Module (mDOM) [10]. The concept of the mDOM is adapted from the KM3NeT DOM [55]. A representation of the mDOM is shown in Fig. 3.12. Due to an extension of the middle part to provide enough space for the electronic components it is not a perfect spherical as the KM3NeT DOM. The cylindrical middle part has also the advantage that the holding structure does not cover any of the PMTs when the mDOM is deployed into the ice.

Figure 3.12: Representation of the multi-PMT Digital Optical Module (mDOM). Courtesy of IceCube collaboration [44].

The main differenece of the mDOM in comparison to the current IceCube DOM is the change from one 25 cm PMT looking downwards to 24 PMTs with 8 cm diameter facing in all directions. Each PMT is surrounded by a reflector to maximize the photon capture. The 24 PMTs in the mDOM results in a larger photocathode area than with one bigger PMT in the DOM. Furthermore, since there are several PMTs in contrary to one large PMT two incident photons can encounter different PMTs what leads to less multi-photoelectron waveforms and photon counting is enhanced. The mDOM covers homogeneously 4π angular distribution due to the spacing of the PMTs. This results into an improved angular acceptance for incident photons and the directional sensitivity which is important for the event reconstruction. A further advantage of the mDOM is the possibility to detect local coincidences. Local coincidences are photon hits of different PMTs in the same module in a certain time window. With this feature, newly-developed algorithms can suppress background by local coincidences [10]. Furthermore, local coincidences can be used for the module calibration [56]. In this thesis local coincidences are of high importance as well. They are used for the reconstruction of MeV neutrino signals, as such from SN neutrinos. This reconstruction is discussed in the next chapter.

3.7 Supernova Detection in a Detector Equipped with mDOMs

For detecting SNe with the help of mDOMs the advantage of local coincidences between several PMTs in one module is utilized. The way to register a SN signal is described in [57]. Two conditions are used to determine a signal induced by SN neutrinos; a local and a global condition. The local condition starts when the first photon hits one PMT. Since 99 % of the coincident hits in different PMTs occur in 10 ns [57], the amount of local coincidences is counted in such a time window. To identify a signal from a SN neutrino, a minimal number of local coincidences in this local time window is requested. To trigger the global condition, a specific number of SN neutrino signals in the whole detector during the time of the SN burst which lasts 10 s (see Sec. 2.3) is required.

Due to a better understanding of background noise of the PMTs, radioactive sources in the glass vessel, and solar neutrinos the most recent results for SN detection in the IceCube-Gen2 configuration with 10000 mDOMs contain a local condition of ≥ 6 local coincidences in a time window of 20 ns and at least 9 detected SN neutrinos during the SN burst time of 10 s [58]. With these two conditions the probability of SN detection depending on the distance to Earth is calculated [57] and depicted in Fig. 3.13.

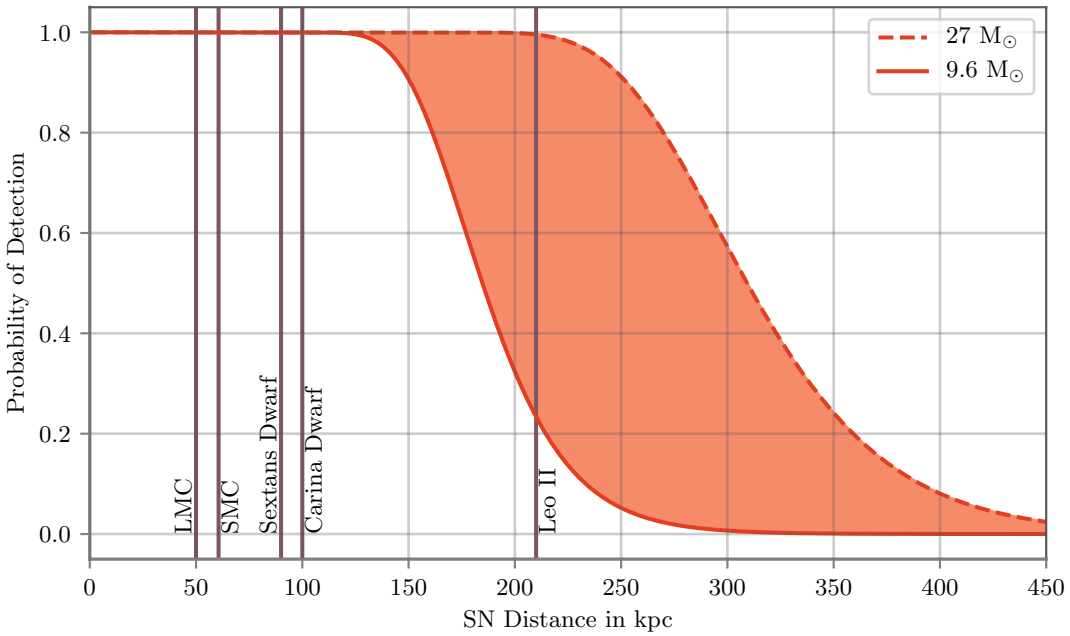

Figure 3.13: Supernova (SN) detection probability versus the distance in kpc for heavy ($27\,M_\odot$) and light ($9.6\,M_\odot$) progenitor stars. The distances of our next neighbouring galaxies are given as vertical lines. Figure taken and modified from [58].

4 Supernova Simulation with mDOMs

Simulations are required to produce SN neutrino spectra with particular parameters (see Sec. 2.4). The investigation of the mDOM sensitivity to the SN neutrino spectrum is done by comparing the simulated spectra to each other. In this chapter a simulation of SN neutrino spectra for mDOMs in South Pole ice is introduced. This simulation is written in Geant4 which is a C++ based toolkit to simulate particles passing through matter by using Monte-Carlo methods. It is widely used in many different fields, such as medical science, particle physics, and astrophysics [59].

In this work, a simulation of the geometry of the mDOM in a surrounding ice medium is used. The simulated detection of SN neutrinos uses this mDOM geometry and detection volume. For the SN neutrino simulations, trigger conditions using local coincidences in the mDOM will be introduced in order to distinguish MeV neutrino events to background events. Therefore, knowledge about the expected background is necessary. In this work three types of background are taken into consideration: uncorrelated noise, correlated noise, and solar neutrinos. The simulations of these get introduced in the following subchapter.

4.1 mDOM Simulation in Geant4

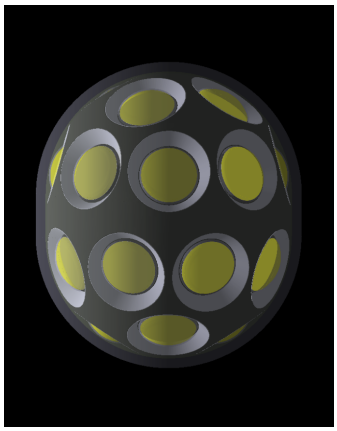

Figure 4.1: Initial geometry of the mDOM in the Geant4 simulation.

The simulation of the mDOM with Geant4 was at first written in two PhD theses [10, 60] and modified to a simulation for SN neutrino detection with the mDOM in [57]. Fig. 4.1 shows the mDOM inside the simulated ice volume. Since the mDOM was firstly planned to have an asymmetry between the two half-vessels, the simulated mDOM has this asymmetry as well. During the work of this thesis the simulation of the mDOM was changed to a symmetric layout, as was the mDOM (see Fig. 3.12). This half vessel rotation is not expected to significantly change any of the results since local

Particle	Class	Description
Optical Photon	G4OpAbsorption	Absorption of optical photons
	G4OpBoundaryProcess	Boundary interactions when photons changes medium
	G4OpMieHG	Mie scattering of photons
Gamma	G4Livermore GammaConversionModel	Electron-positron pair production of gammas
	G4Livermore ComptonModel	Compton effect for gammas
	G4Livermore PhotoElectricModel	Photoelectric effect for gammas
Electron	G4eMultipleScattering	Electron scattering in medium
	G4Livermore IonisationModel	Ionisation of the medium by electrons
	G4eBremsstrahlung	Bremsstrahlung of electrons
Positron	G4eMultipleScattering	Positron scattering in medium
	G4eIonisation	Ionisation of the medium by positrons
	G4eBremsstrahlung	Bremsstrahlung of positrons
	G4eplusAnnihilation	Annihilation of positrons with electrons of medium

Table 4.1: The physics list with the used interaction classes of Geant4 in this simulation for the occurring particles.

coincidences have the same probability because they do not depend on the PMT directions.

Geant4 is developed to cover interactions of particles in materials within a certain volume. For that, it provides fundamental components of a physical simulation such as elementary particles for primary events, particle interaction processes, the tracking of particles, a selection of diverse materials, and the visualization of the simulated volume [61]. Particles and their interactions in the simulation are given by Geant4 in provided classes. The processes for particle interaction in this simulation are given in the physics list in Tab. 4.1. Since there is no neutrino physics included in Geant4 and since the use of neutrinos as primary particles would be highly inefficient due to their low cross sections, the primary particles used in the simulation are positrons, which are generated as secondary particles in the

IBD. In order to do this, the events must be weighted by the detection probability which will be discussed in detail in Sec. 5.1.2.

The simulation contains the geometry of the mDOM which means all outside parts of the mDOM are simulated individually: the holding structure, the PMTs, the reflectors, the optical gel, and the pressure glass vessel. The holding structure acts simply as an absorber of photons. The PMTs are modelled as solid glass tubes each containing a photocathode. When a photon hits a photocathode it is counted as one hit with a certain probability according to the quantum efficiency of the PMT by using Monte-Carlo methods. For different usages of the simulation different types of the other components can be included into the simulation. Since the only purpose of the simulation in this work is the simulation of SN neutrino energy spectra, the gel, the reflectors, and the glass are chosen those ones which will be most likely in the final mDOM. These are Wacker SilGel 612 A/B gel, Alemco V95 reflector cones, and Vitrovex glass.

The medium which surrounds the mDOM in the simulation is ice whose light propagation is described by two parameters: the absorption and the scattering length. The Antarctic follows a layer structure in dependence of depth originated by the deposition of dust particles in the ice over the year. The ice properties have been therefore parametrized as a function of the depth [62].

The absorption coefficient $a(\lambda)$ is parametrized by [63]:

$$a(\lambda) = a_{\text{dust}}(400)\left(\frac{\lambda}{400}\right)^{-\kappa} + A\exp\left(-B/\lambda\right)\cdot(1+0.01\delta\tau), \tag{4.1}$$

where λ is the wavelength of the photon given in nm, $a_{\text{dust}}(400)$ the absorption caused by dust at 400 nm and $\delta\tau = T(d) - T(1730)$ the temperature difference relative to the depth of 1730 m [64]. The other parameters have been evaluated in [62] to $A = (6954 \pm 973)\ \text{m}^{-1}$, $B = (6618 \pm 71)\,\text{nm}$, and $\kappa = 1.08 \pm 0.01$. The reciprocal $1/a(\lambda)$ is the average distance before a photon gets absorbed.

The scattering in ice is due to the dust grain size mainly Mie scattering [65, 62]. The Mie scattering coefficient $b(\lambda)$ is given by [63]:

$$b(\lambda) = \frac{b_e(\lambda)}{1-\langle\cos\theta\rangle} = b_e(400)\left(\frac{\lambda}{400}\right)^{-\alpha}, \tag{4.2}$$

where $b_e(\lambda)$ is the effective scattering coefficient and θ the deflection angle of the scattering with $\langle\cos\theta\rangle = 0.9$ [63]. The exponent of the power law is $\alpha = 0.90 \pm 0.03$ [62]. The average Mie scattering length is given as $1/b_e(\lambda)$.

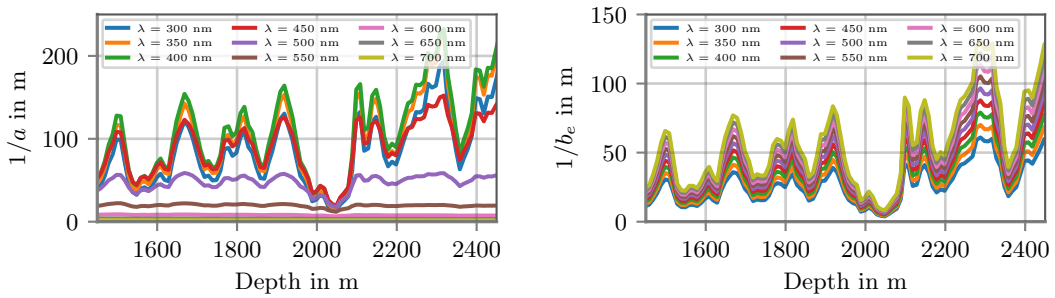

Figure 4.2: Average absorption length $1/a$ (left) and Mie scattering length $1/b_e$ (right) for photons with different wavelength versus the depth of South Pole ice.

The average adsorption length and Mie scattering length is calculated by using Eq. 4.1 and 4.2 with data for $a_{\text{dust}}(400)$ and $b_e(400)$ taken from [63]. Both are depicted for different wavelengths in the visible range in Fig. 4.2. The average absorption and Mie scattering length diverge dramatically from layer to layer.

For simplification, the ice in the simulation is treated as uniform which means the simulation contains one layer of ice and no drilling hole with different ice properties around the modules. An ice layer of 2278.2 m depth was chosen as simulation medium since this layer has one of the largest length for absorption ($1/a(400) = 227.2\,\text{m}$) and Mie scattering ($1/b_e(400) = 76.8\,\text{m}$).

The size of the simulated volume limits the simulation time. On the other hand the volume must cover every interaction from which Cherenkov photons get detected. In [57] it is shown that the simulated volume has to have a radius of $\sim 10\,\text{m}$ to fulfill both demands for SN neutrinos of 25 MeV. In order to cover SN neutrinos with higher energies, the radius in this simulation is 20 m.

4.2 Supernova Simulation

The first step of the SN neutrino detection is the generation of a single positron inside the ice volume. The positron has a certain energy which is derived from the neutrino energy via Eq. 3.4 which is chosen from the neutrino energy distribution given into the simulation. The neutrino energy distribution follows either Eq. 2.10 or a flat energy distribution which emphasizes higher energies in contrast to $f_\alpha(E)$. The generated positron then has a certain direction which is chosen from the angular distribution in [38].

In this work, local coincidences are defined as the detection of Cherenkov photons of one MeV SN neutrino in several PMTs within one module.

Parameter	**Function**
$\bar{\nu}_e$ Mean Energy $\langle E \rangle$	Input parameter for given $E_{\bar{\nu}_e}$ distribution
$\bar{\nu}_e$ Energy $E_{\bar{\nu}_e}$	Antineutrino energy
$\cos\theta$	Angle between the generated positron and antineutrino direction
e^+ Energy E_{e^+}	Positron energy
Event Weight	Event probability depending on cross section and size of the volume
Vertex Position (x,y,z)	Event position
Primary Direction (p_x,p_y,p_z)	Direction of outgoing positron
Total Hits	Total number of photons reaching all photocathodes
Total Hit PMTs	Total number of PMTs get hit
Module Number	ID of module in which PMT got hit
PMT Number	ID of the PMT in the module
Hits in that PMT	Number of photons hitting that PMT
Hit Time	Arrival time of photon

Table 4.2: Table of all saved parameters and their function in the simulation.

For that, when at least one photon hits a photocathode different event parameters are saved. The output parameters are given in Tab. 4.2. When a second hit is detected in a different photocathode within the time window Δt, it is called a coincidence hit meaning the two hits are registered together. Since more than 99 % of all registered hits happen already within 10 ns [57], the time window Δt for coincidence hits is chosen in this work to be 20 ns.

4.3 Background Simulations

Among all the background that the modules detect in the IceCube detector, the most relevant ones that can be confused with SN neutrino signals are uncorrelated noise from the PMTs, detections from radioactive decays in the vessel glass, and incoming neutrinos from the sun. Therefore, these sources will be the ones included in the background expectations in this work.

Even a PMT which is not illuminated by photons always counts some signal. The frequency of these signals is called the dark rate of a PMT. Since these counts are uncorrelated to the hits of other PMTs, it contributes to uncorrelated noise. The method to estimate local coincidences of the dark rate f_{noise} is derived in [66]. It consists of three components:

$$f_{\text{noise}} = P_{\text{noise}} \cdot f_{\text{PMT}} \cdot N_{\text{mDOM}}, \tag{4.3}$$

where N_{mDOM} is the total number of mDOMs and f_{PMT} the dark rate for a single PMT. P_{noise} is the probability that at least $n_{\text{coinc}} - 1$ PMTs detect photons within the chosen time window Δt and can be expressed as:

$$P_{\text{noise}} = 1 - B_{\text{cum}}(n_{\text{coin}} - 2 | N_{\text{PMT}}, P_{\text{PMT}}), \tag{4.4}$$

where $B_{\text{cum}}(m|n,p) = \sum_{k=0}^{m} \binom{n}{k} p^k (1-p)^{n-k}$ is the cumulative binomial probability for up to m successes out of n tries taking into account a probability p [67] and $P_{\text{PMT}} = 1 - \exp(-f_{\text{PMT}} \Delta t_{\text{coin}})$ the Poisson probability for at least one signal in the PMT [66]. In this work a dark rate of $f_{\text{PMT}} = 50\,\text{Hz}$ was used which was found experimentally in [68] for the assumed PMTs.

Radioactive decays in the glass vessel of the mDOM produce scintillation and Cherenkov photons. These photons can hit different PMTs and thereby produce a coincident signal. Since coincidence hits from these decays are from the same event, this background is correlated. The simulation of this noise was done by [68] using the same Geant4 mDOM simulation as in this work and therefore its data is used here. To derive the rate of coincidence hits from the correlated noise, the decay activities of the glass vessel have to be known. The activities for the radioactive decays from [68] that are presented in Tab. 4.3 are used in this work.

Radioactive Decay	**Activities**
^{238}U chain	$(4.61 \pm 0.07)\,\text{Bq/kg}$
^{235}U chain	$(0.59 \pm 0.05)\,\text{Bq/kg}$
^{232}Th chain	$(1.28 \pm 0.06)\,\text{Bq/kg}$
^{40}K	$(61 \pm 1)\,\text{Bq/kg}$

Table 4.3: Activities from [69] used for radioactive decays in this work.

Coincidence hits from solar neutrinos mainly originate from neutrinos produced by $^8\text{B} \rightarrow {}^8\text{Be} + e^+ + \nu_e$, because these neutrinos have the highest energies from solar neutrinos [8]. The spectrum of these neutrinos is

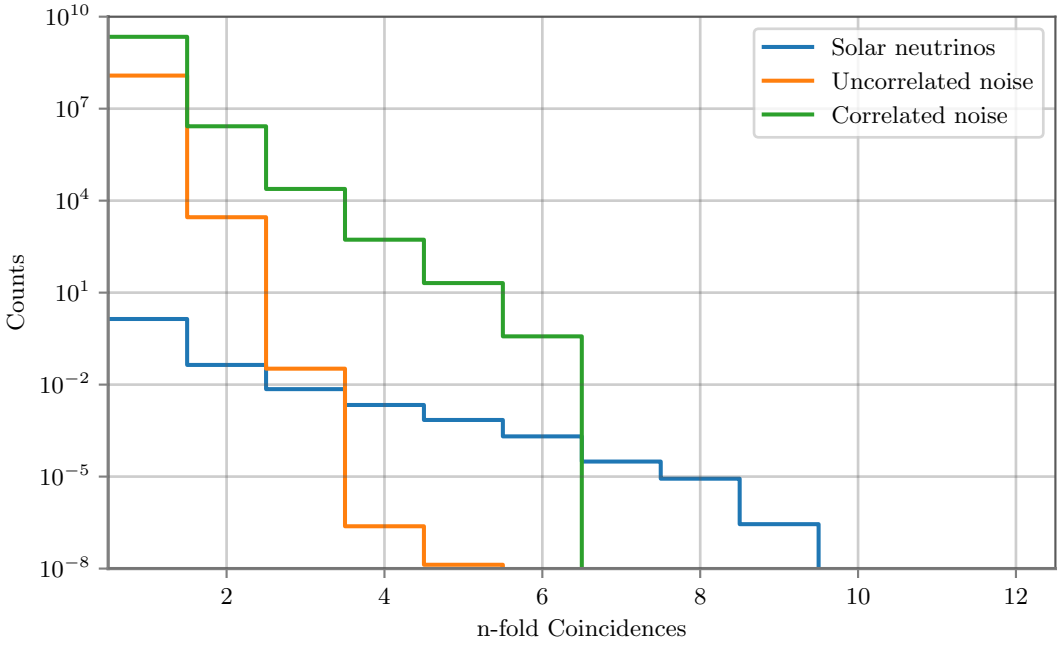

Figure 4.3: Counts of coincidence hits in 20 ns for three background sources: solar neutrinos (blue), uncorrelated noise from the PMTs (orange), and correlated noise from radioactive decays in the mDOM (green).

given in [70]. The simulation is nearly the same as the one described for SN neutrinos in Sec. 4.2 with the difference that there are no solar antineutrinos. This means elastic scattering is the dominant interaction and not the IBD which leads to a lower interaction rate in ice. The simulation data of the correlated noise is taken from [69].

The n-fold coincidence hits for the background sources within the time window $\Delta t = 20\,\text{ns}$ are given in Fig. 4.3. The main contribution of the background comes from radioactive decays inside the vessel glass. The drop betwen 6- and 7-fold coincidence hits is due to the lack of radioactive decays producing such a signal. Due to the facts that there is a finite simulation time and that such a signal occurs very rarely per decay, no decay giving such a signal was found. However, it is to be expected that increasing the simulation time the the histogram would continue steadily as it does for lower than 6-fold coincidence hits. Since the random noise is uncorrelated, the probability vanishes for higher coincidences. The reason for the small rate is the low cross section (see. Sec. 3.1) of electron scattering in ice.

5 Neutrino Energy Spectra with Intra-Module Coincidences

The main purpose of this work is to investigate the SN neutrino energy spectrum sensitivity of the IceCube-Gen2 configuration (see Sec. 3.5) which is done with the simulations described in the previous chapter. The results of these simulations are given in the next subchapter and the method of how to study the sensitivity to SN neutrino spectrum via sensitivity maps is derived. The combination of those sensitivity maps will be then studied. The investigations of the sensitivity maps contain also results for different SN distances and module configurations.

5.1 Simulations of Intra-Module Coincidences

For investigating coincidences within one module, the simulation described in Sec. 4.1 is used with one asymmetric mDOM in the center. The input parameters vary from 8.0 to 18.0 MeV with 0.5 MeV stepsize for the mean energy $\langle E \rangle$ and α from 1.5 to 5.0 with a step size of 0.5. This gives in total 168 single simulations. Each of them is done with 1 000 000 generated particles and a detection volume of 20 m diameter and 40 m height.

The position of each n-fold coincidence event is investigated in the next subchapter. The formalism to reach n-fold coincidence histograms is shown in a further subchapter. Afterwards the effect of systematic uncertainties is discussed.

5.1.1 Positions of Coincidence Events

Neutrino can interact anywhere in the ice, but events which lead to n-fold coincidences likely occur only in the vicinity of the mDOM. In this section it is checked whether the simulated volume covers all event positions for different n-fold coincidences. Up to 50 randomly chosen event positions are displayed in the simulated volume in Fig. 5.1. The gray dotted volume shows the area of the most distant event. The events of 1- and 2-fold

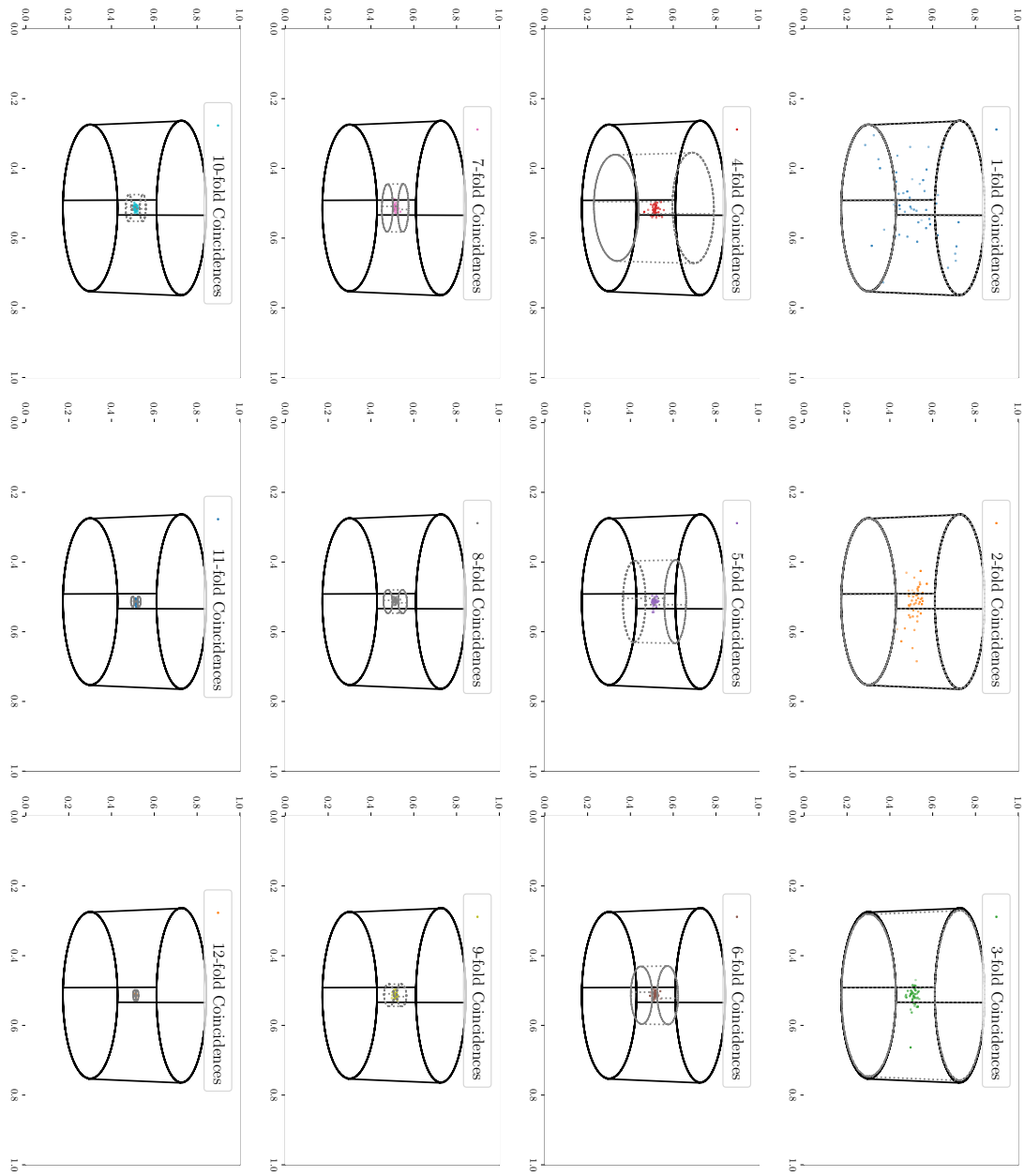

Figure 5.1: Event positions for n-fold coincidence in the simulated volume (black). The volume of the most distant event is depicted in gray.

coincidence hits are distributed in the whole simulated volume. From 3-fold coincidence hits on, the interaction volume lays completely inside the simulated volume.

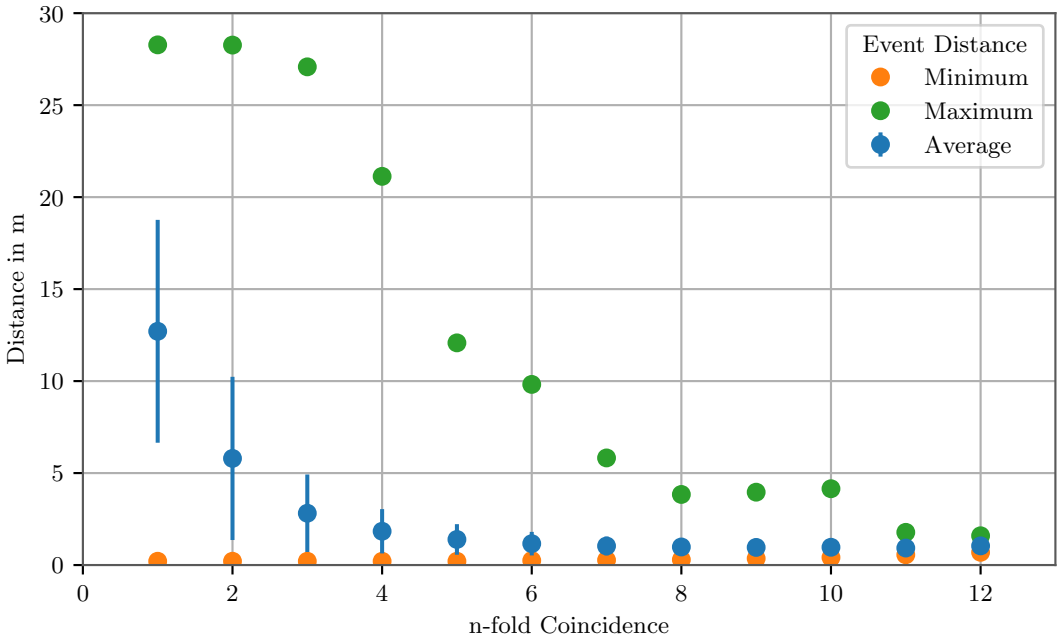

Figure 5.2: The average (blue), minimum (orange) and maximum (green) event distance for the different n-fold coincidence hits.

The average event distance for n-fold coincidence events is depicted in Fig. 5.2. In this figure the maximum and minimum distance are also shown. The maximum event distance for 1- and 2-fold coincidence hits are at the most outer point of the simulated volume which is 28.3 m from the center away. Although the event volume of 3- and 4-fold coincidence hits are covered by the simulated volume, the maximum distance of these coincidence hits is more distant than the 20 m radius of the simulated volume. Nevertheless, the average event distance for all-fold coincidence hits is shorter than 20 m which means that most of the events are covered by the simulated volume. The minimum event distance shows a different effect. For higher n-fold coincidence hits it gets more distant which can be explained by the angle of the Cherenkov cone. Since the Cherenkov light has a defined angle under which it is emitted, photons from events which take place at short distance from the mDOM can reach fewer PMTs than photons from further events.

5.1.2 Event Weighting

Because the simulation of SN energy spectra starts directly with secondary particles, each event needs to be weighted. The weights will be divided

into three parts: the general weight, the event weight, and the distributed weight.

The general weight W_T scales the detected events according to the flux of the SN neutrinos across the simulated and the number of generated events. It is given as:

$$W_\mathrm{T} = \frac{N_\mathrm{mDOM}}{N_\mathrm{generated}} \cdot 4\pi r^2 \cdot \int_{t=0\,\mathrm{s}}^{t=10\,\mathrm{s}} \Phi(t)dt. \tag{5.1}$$

The simulation sets the radius of the simulated volume r, the amount of mDOMs N_mDOM and generated events $N_\mathrm{generated}$. Φ is the flux from the SN model. As shown in Eq. 2.9 it depends on the distance d of the SN. This means the distance of the assumed SN can be directly changed by recalculating the general weight with a different distance.

The event weight ω_e stands for the probability of each interaction to take place in the ice:

$$\omega_\mathrm{e}(E) = \sigma_\mathrm{tot}(E) \cdot N_\mathrm{target} \cdot r_\mathrm{path}. \tag{5.2}$$

It consists of the interaction cross section σ_tot which depends on the neutrino energy E_ν given in Eq. 3.3 for IBD events. The number of possible targets N_target is given in Eq. 3.5. The parameter r_path represents the length of the neutrino's path through the simulated ice. The neutrino energy E_ν and the event position is different for each event, thus the event weight needs to be calculated for each event separately.

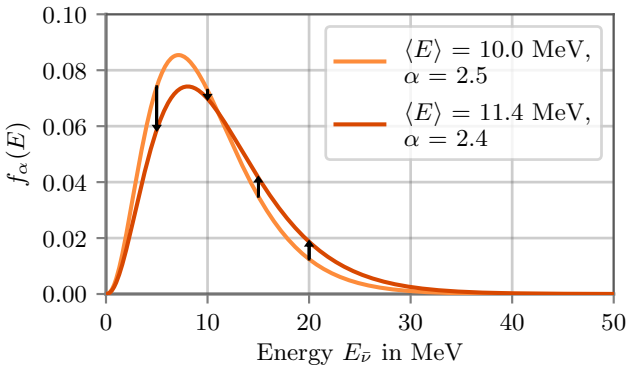

Figure 5.3: Example for the distributed weight w_dist. Out of a simulated SN spectra (orange) an unknown SN spectra (red) gets calculated. Black arrows indicate w_dist for several energies.

The distributed weight ω_dist allows to scale the detected signal from a particular ($\langle E \rangle$, α) to any other combination. In Fig. 5.3 one example of the basic mechanism is outlined. Each detected event is therefore weighted with a factor corresponding to its energy.

$$\omega_\mathrm{dist}(E) = \frac{f_\mathrm{calc}(E)}{f_\mathrm{sim}(E)} \tag{5.3}$$

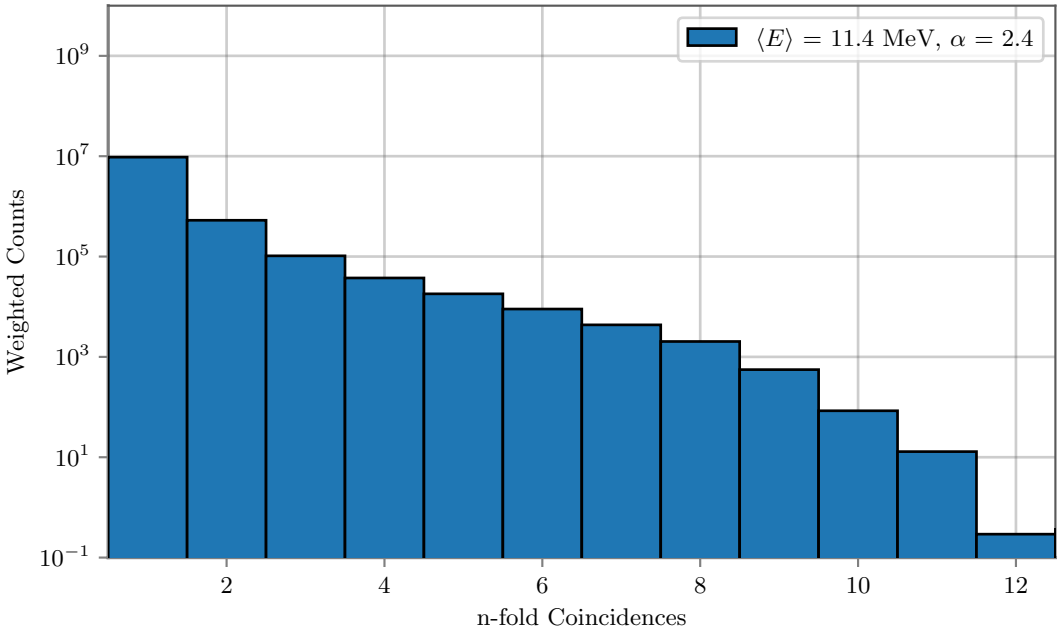

Figure 5.4: Example of a n-fold coincidence histogram for $\langle E \rangle = 11.4\,\mathrm{MeV}$ and $\alpha = 2.4$.

Applying these three different weights on the raw data gives n-fold coincidence histograms for each SN spectrum with a defined ($\langle E \rangle$, α) combination. One example of such histograms is depicted in Fig. 5.4. For studying the sensitivity towards the SN neutrino spectrum, the different spectra have to be compared. The method for comparing these histograms to each other is outlined from Sec. 5.2 on.

5.1.3 Systematic Uncertainties

The entries of the generated histograms are treated as a representative data set which assumes infinite data simulation. Since this is not possible, this could lead to biases in the data [71]. These biases are systematic uncertainties of such simulations. To estimate these systematic uncertainties each entry could be investigated as done in [71], but this goes beyond the scope of this work.

Instead the effect of statistic uncertainties is estimated in this work. The comparison of the uncertainties arising from the weighting process

$$\sigma_{\text{weights}} = \sqrt{\sum_i \omega_{\text{e},i}^2 \, W_{\text{T},i}^2 \, \omega_{\text{dist},i}^2} \tag{5.4}$$

to the statistic uncertainties

$$\sigma_{\text{stat}} = \sqrt{\sum_i \omega_{\text{e},i} W_{\text{T},i} \omega_{\text{dist},i}}. \tag{5.5}$$

The requirement is that the statistic uncertainties are much larger:

$$\frac{\sqrt{\sum_i \omega_{\mathrm{e},i}^2 W_{\mathrm{T},i}^2 \omega_{\mathrm{dist},i}^2}}{\sqrt{\sum_i \omega_{\mathrm{e},i} W_{\mathrm{T},i} \omega_{\mathrm{dist},i}}} \ll 1. \tag{5.6}$$

For both uncertainties, $\sigma_{\mathrm{weights}}$ and σ_{stat}, the general weight $W_{\mathrm{T}} = 9.22 \times 10^{12}$ is the same. To simplify the division further, only a single distributed weight ω_{dist} and a single event weight ω_{e} for a specific energy E are taken into account. Then the minimum number of generated particles can be calculated by

$$N_{\mathrm{generated}} \gg \omega_e \cdot \omega_{\mathrm{dist}} \cdot N_{\mathrm{mDOM}} \cdot 4\pi r^2 \cdot \int_{t=0\,\mathrm{s}}^{t=10\,\mathrm{s}} \Phi(t) dt. \tag{5.7}$$

The minimum number of $N_{\mathrm{generated}}$ is depicted for different cases in Fig. 5.5. Although there are energies for which the condition does not hold true, a reasonable upper limit of the calculated entries is $\langle E \rangle = 20\,\mathrm{MeV}$ and $\alpha = 10.0$, because the maximum of Eq. 2.10 $f_{\alpha,\mathrm{max}}(E_{\mathrm{max}})$ is at

$$E_{\mathrm{max}} = \frac{\alpha}{\alpha + 1} \langle E \rangle, \tag{5.8}$$

which means $E_{\mathrm{max}} \leq \langle E \rangle$.

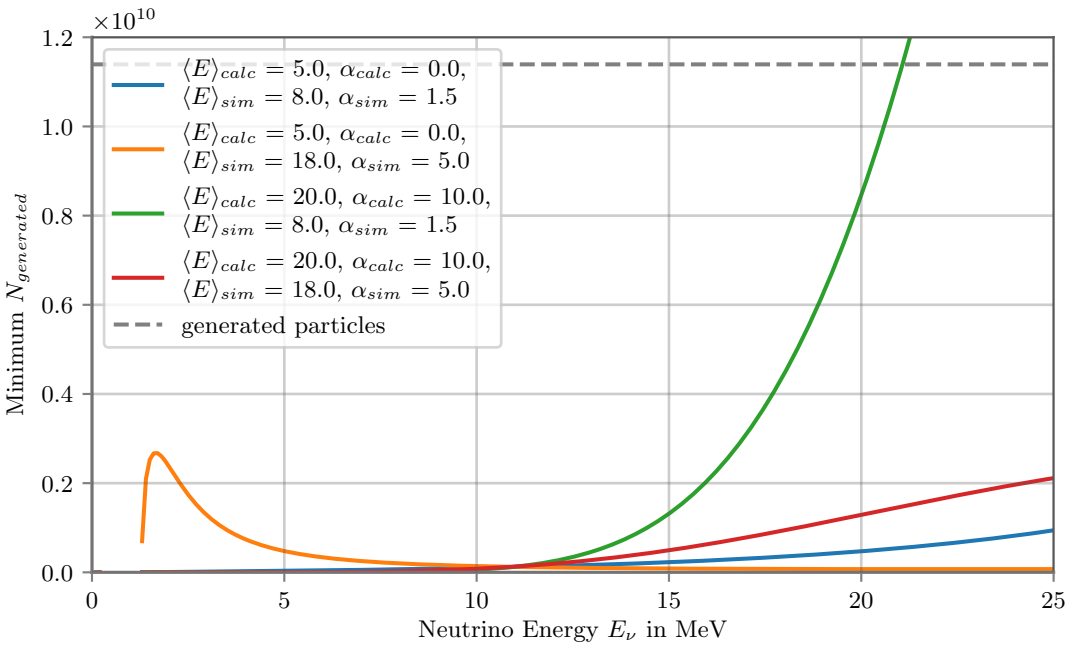

Figure 5.5: Comparison of the energy and the minimum amount of $N_{\mathrm{generated}}$ events to keep the effect of the systematic uncertainty small. $N_{\mathrm{generated}}$ is calculated by Eq. 5.7.

5.2 Single χ^2 Method of Energy Extraction

From the simulations and through the weighting process, a histogram for several parameter combination is created. To investigate the sensitivity from these histograms, in a first step a ratio map is created (Sec. 5.2.1). In in this ratio map each point corresponds to one parameter combination. To compare these points to a reference point, a χ^2 method is implemented which will be explained in Sec. 5.2.3. Therefore, it is necessary to know the number of degrees of freedom of each point which is investigated in Sec. 5.2.2.

5.2.1 Ratio Map from Parameter Histograms

Histograms of different $\langle E \rangle$ and α combinations differ in the counts of the n-fold coincidence hits. Ratios of different n-fold coincidence hits can therefore be used to compare different histograms to each other. The histograms of the extreme values of $\langle E \rangle$ and α are shown in Fig. 5.6 and compared to the background coincidence hits and the 1σ fluctuation of this background. The counts for histograms of larger $\langle E \rangle$ and lower α are higher. Since the different count rates of $\langle E \rangle = 20\,\mathrm{MeV}$ and $\langle E \rangle = 5\,\mathrm{MeV}$ of the same α are much more similar other than the different count rates of same $\langle E \rangle$ with $\alpha = 10$ and $\alpha = 0$, the α parameter seems to have a larger influence on the count rate than the $\langle E \rangle$ parameter. This effect stems from neutrinos with higher energies which are favored for lower α (see Eq. 2.10).

In a first approach, the ratios of 3-fold coincidence hits versus 4 and more-fold coincidence hits

$$R_{3,\geq 4} = \frac{N_3}{N_{\geq 4}} \tag{5.9}$$

are calculated for all $\langle E \rangle$ and α combinations and plotted into a ratio map because all events of these coincidences are covered by the simulations as shown in Sec. 5.1.1. The uncertainty of each point in this map is given by

$$\sigma(R_{3,\geq 4}) = \sqrt{\left(\frac{\sigma(N_3)}{N_{\geq 4}}\right)^2 + R^2 \left(\frac{\sigma(N_{\geq 4})}{N_{\geq 4}}\right)^2}, \tag{5.10}$$

where the uncertainty of j-fold coincidence hits is calculated by

$$\sigma(N_j) = \sqrt{(\sqrt{N_j})^2 + \sigma^2(\mathrm{BG}_j)}. \tag{5.11}$$

This means the ratios are calculated out of the signal while the uncertainty of each ratio contains the statistical uncertainty of the signal and the the

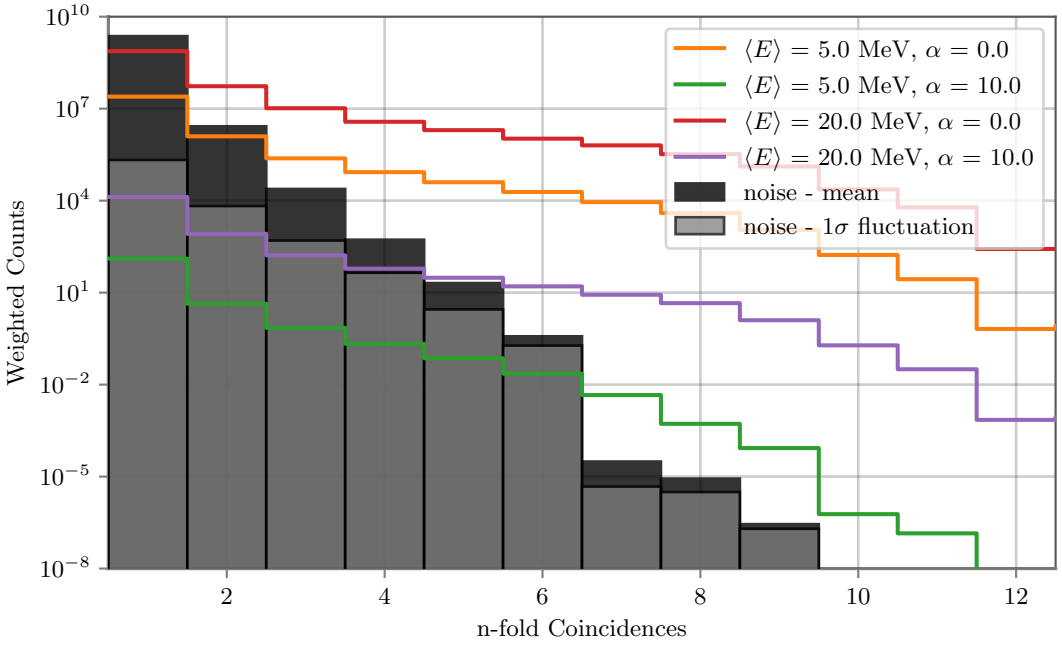

Figure 5.6: Comparison of the histograms at the corner points of the ratio map (orange, green, red, purple) with the background (black). The 1σ fluctuation of the background is shown in gray.

1σ fluctuation of the background. For the real measurement of a SN signal the mean background is assumed to be totally known and that it can be subtracted from the incoming SN signal whereas the uncertainty of the signal will still have the uncertainty of the background variation.

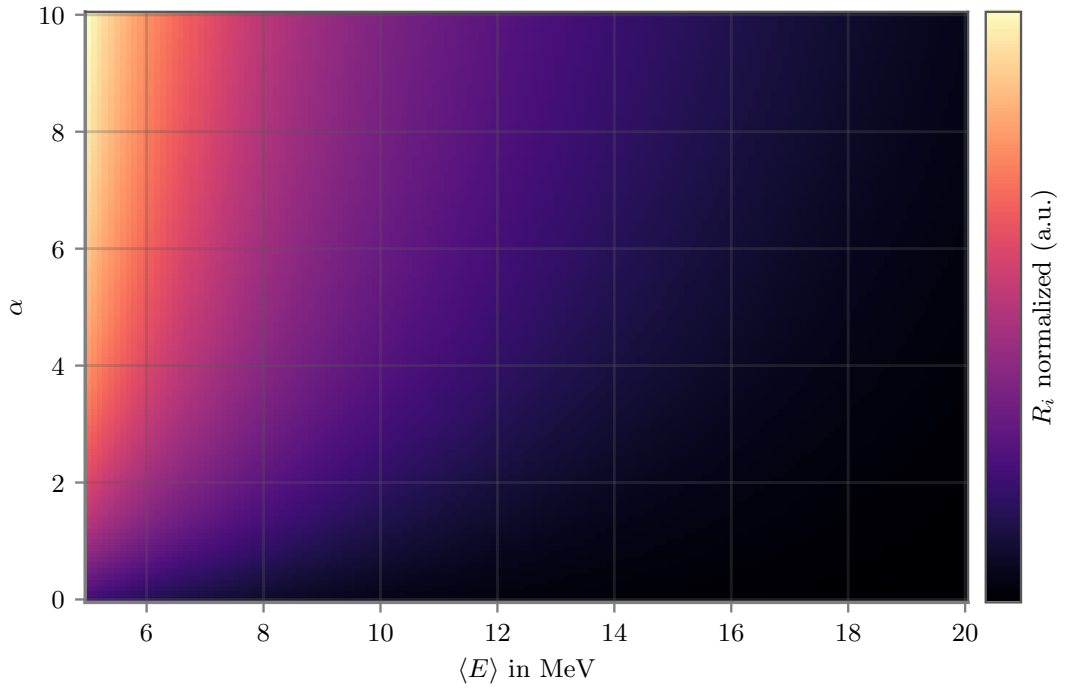

Figure 5.7: Map of the ratio $R_{3,\geq 4}$. A pattern of same color can be identified which gets steeper for higher α.

The ratio map for $R_{3,\geq 4}$ is shown in Fig. 5.7. The color pattern shows that points of different $\langle E \rangle$, α combination have the same value. This color pattern gets steeper as α is larger.

5.2.2 Degrees of Freedom of Ratio Points

To check the degrees of freedom n for each point in the ratio map whose probability density function $P(\chi^2; n)$ is given by [67]

$$P(\chi^2; n) = \frac{2^{-n/2}}{\Gamma(n/2)} \chi^{n-2} \exp\left(-\chi^2/2\right), \tag{5.12}$$

each n-fold coincidence rate r is newly generated using the Poisson distribution [67]

$$P(r; \lambda) = \frac{\lambda^r \exp\left(-\lambda\right)}{r!} \tag{5.13}$$

with the actual rate as expectation value λ. This generation is done 10000 times. Each Poisson generated histogram gets compared with the actual value by

$$\chi^2 = \frac{(R_{\text{Poisson}} - R_{\text{ref}})^2}{\sigma^2(R_{\text{ref}})}. \tag{5.14}$$

The distribution of the χ^2 gives the Poisson distribution with k degrees of freedom. In this case the distribution is compared with $k = 1$ and $k = 2$. This is shown in Fig. 5.8. In Fig. 5.9 the cumulative χ^2 distribution is compared to the cumulative distribution function of $k = 1$ and $k = 2$ degrees of freedom.

Although the ratio for each point depends on two parameter ($\langle E \rangle$, α), its χ^2 distribution of Poisson generated histograms follows, with small fluctuations, a χ^2 distribution of 1 degree of freedom. The reason for this behaviour is the dependence of α on $\langle E \rangle$ (see Eq. 2.11).

5.2.3 Sensitivity Maps

The sensitivity of the mDOM towards the SN neutrino spectrum depends on how well the mDOM can distinguish between the SN spectra of different $\langle E \rangle$, α combinations. Therefore, the ratio points in the map are compared with a reference point by the χ^2 analysis as done in [72, 51]

$$\chi_i^2 = \frac{(R_i - R_{\text{ref}})^2}{\sigma^2(R_{\text{ref}})}. \tag{5.15}$$

The reference point was chosen to be the mean of the $\langle E \rangle$ distribution (Fig. 2.9) and the mean of the α distribution (Fig. 2.10) of antineutrinos

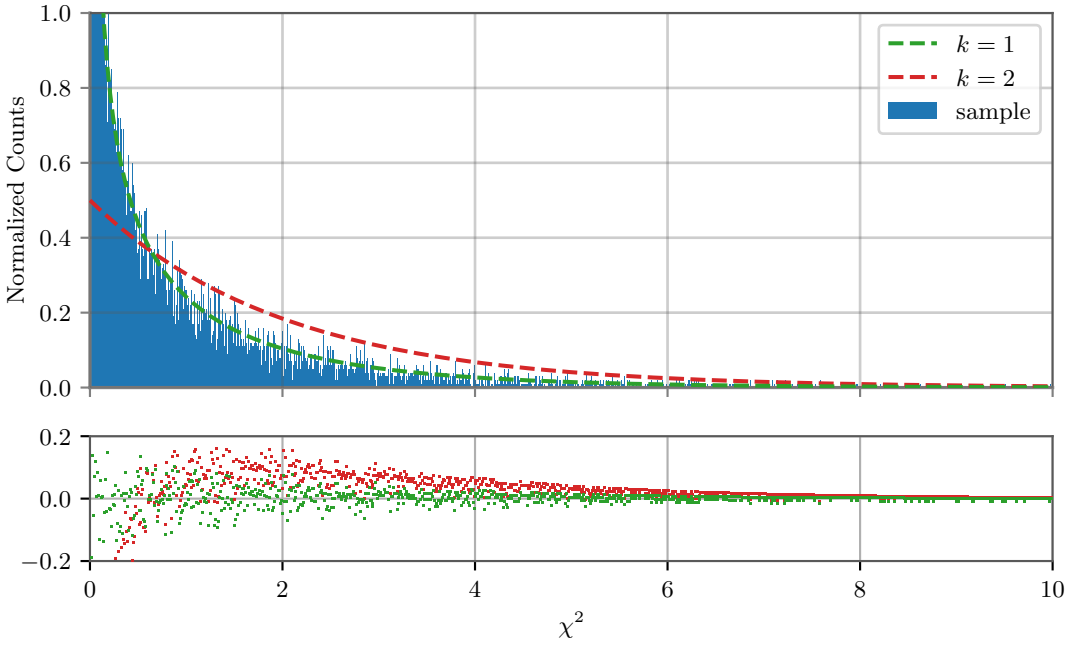

Figure 5.8: Upper: χ^2 distribution from the ratio of Poisson generated histograms compared with the probability density function of $k = 1$ (green) and $k = 2$ (red) degrees of freedom. Lower: Residuals of the χ^2 distribution with the theoretical curve of $k = 1$ (green) and $k = 2$ (red) degrees of freedom.

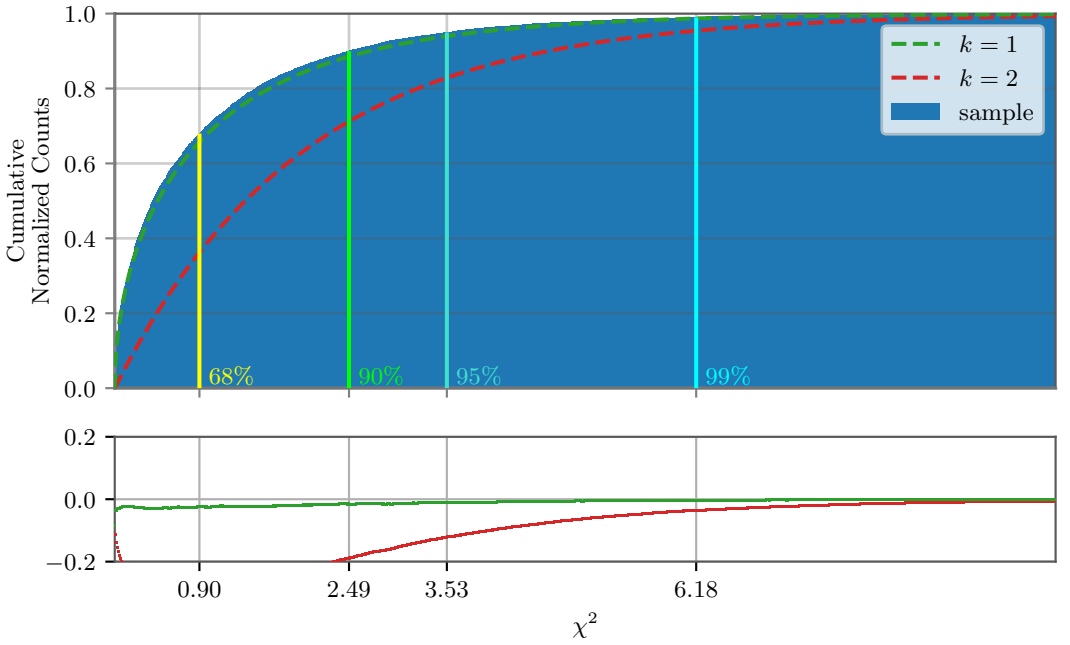

Figure 5.9: Upper: Cumulative χ^2 distribution from the ratio of Poisson generated histograms compared with the cumulative distribution function of $k = 1$ (green) and $k = 2$ (red) degrees of freedom. Lower: Residuals of the cumulative χ^2 distribution with the theoretical curve of $k = 1$ (green) and $k = 2$ (red) degrees of freedom. The values where the cumulative χ^2 distribution exceeds 68 % (yellow), 90 % (lime), 95 % (turquoise), and 99 % (cyan) are given.

from a SN of a 27.0 $M_\odot$ progenitor star (see Tab. 2.1). The parameter combination of the reference point is $\langle E \rangle = 11.4\,\text{MeV}$ and $\alpha = 2.4$.

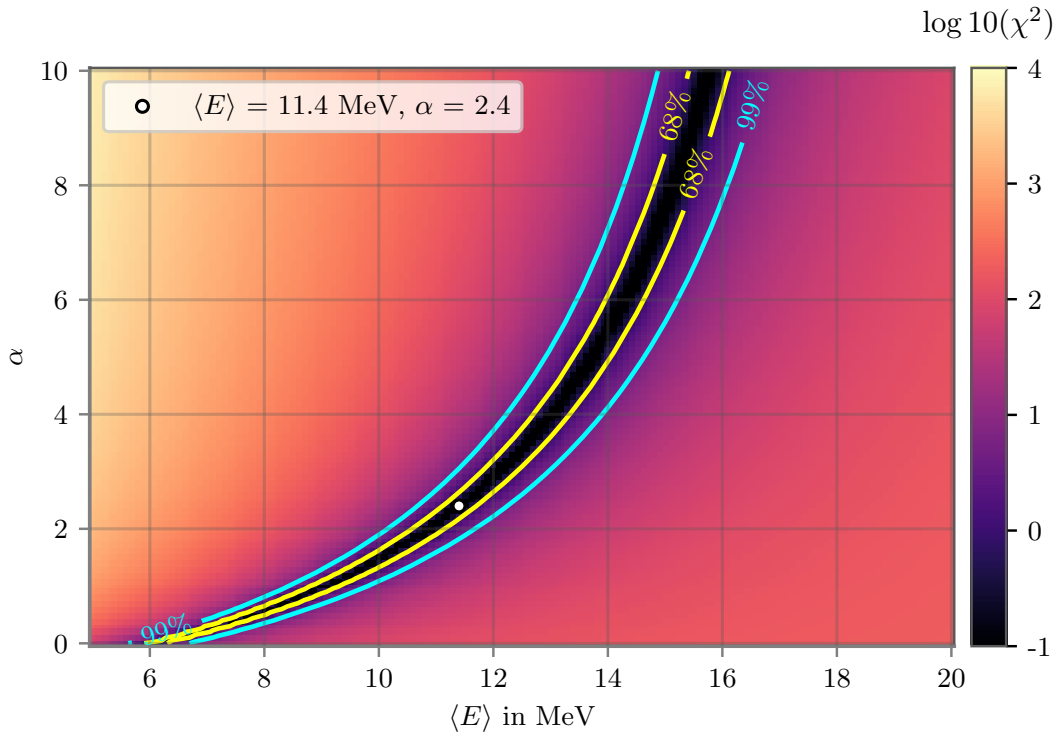

Figure 5.10: χ^2 map of the comparison between ratios $R_{3,\geq 4}$ of different parameter combinations with a reference point via a χ^2 method. The reference point ($\langle E \rangle = 11.4\,\text{MeV}$, $\alpha = 2.4$) is denoted with a white point. The 68 % confidence area is marked by a yellow line, the 99 % confidence area by a cyan line.

The resulting χ^2 map is shown in Fig. 5.10. The white point marks the reference point. It is encircled by yellow and cyan lines which show the confidence level at 68 % and 99 %. The color pattern of the ratio map (Fig. 5.7) shows a degeneracy of the values. There is no unique salient point which would be the reference point, but a "valley" of low χ^2 values. This means that the method would not have sensitivity to distinguish different SNe within the degeneracy area.

To verify the calculations in this section, a cross-check is done. Therefore, 10000 Poisson generated histograms as described in Sec. 5.2.2 are used. One example for this analysis with a generated histogram is shown in Fig. 5.11 left. In Fig. 5.11 right, the comparison between the amount that the reference point is located in the area of 68 %, 90 %, 95 %, and 99 % and the expectation is shown.

The χ^2 analysis for the ratio $R_{3,\geq 4}$ can be used to find a valley including the reference point. Reversely, when the parameter combination is unknown

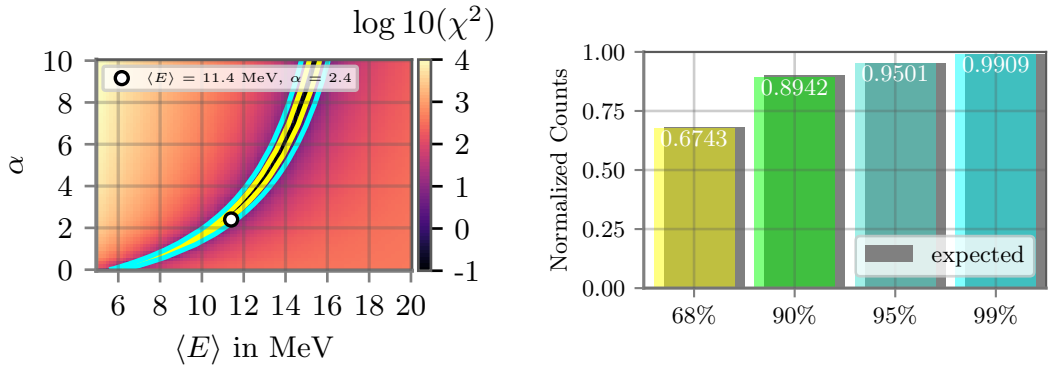

Figure 5.11: Left: χ^2 map of the comparison between ratios of different parameter combinations with a reference point via a χ^2 method. The reference point is a Poisson generated histogram with the rates of ($\langle E \rangle = 11.4\,\text{MeV}$, $\alpha = 2.4$) as expectation values which is denoted with a white point. The 68 % confidence area is marked by a yellow line, the 99 % confidence area by a cyan line. Right: Check of the coverage of the reference point with 10000 Poisson generated histograms with its rates as expectation values.

the degeneracy of the valley does not allow to find the reference point directly. The assumption of one parameter is required to find the other one. In a next step (Sec. 5.3) this problem gets investigated further.

5.3 Combined χ^2 Method

This subchapter shows an attempt to avoid the problem of the degeneracy of a single χ^2 map by using a combination of several χ^2 maps. In a further step the combination of the χ^2 maps is optimized. The performance of this method is investigated including the distance of SN and the amount of mDOMs in the detector.

5.3.1 Combination of Sensitivity Maps

To break the degeneracy of the smallest χ^2 values, different cases or the combination of different sensitivity maps are required, thus the ratios of Sec. 5.2) are modified. For this approach, firstly the columns from 3-fold coincidence hits to 12-fold coincidence hits, which contains all higher coincidence hits as well, are used. Each single column is normalized by the total number of counts of all used columns. This means the new ratios R_j are given by:

$$R_j = \frac{N_j}{\sum_{i=3}^{12} N_i}, \qquad j = 3, \ldots, 12. \tag{5.16}$$

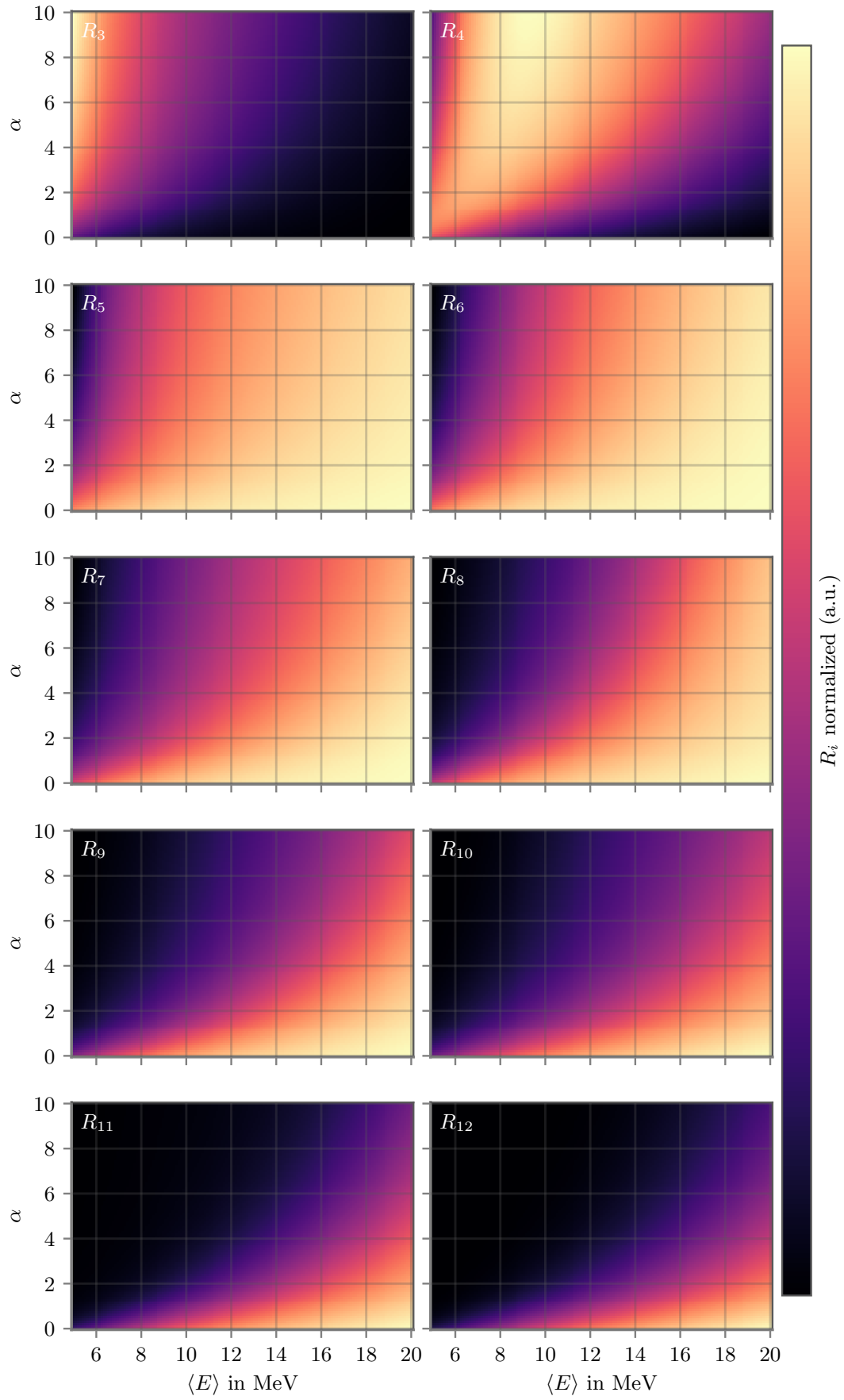

Figure 5.12: Single ratio maps of R_j for $j = 3, \ldots, 12$. In R_4 a transition for lower ratios takes place from lower right to upper left.

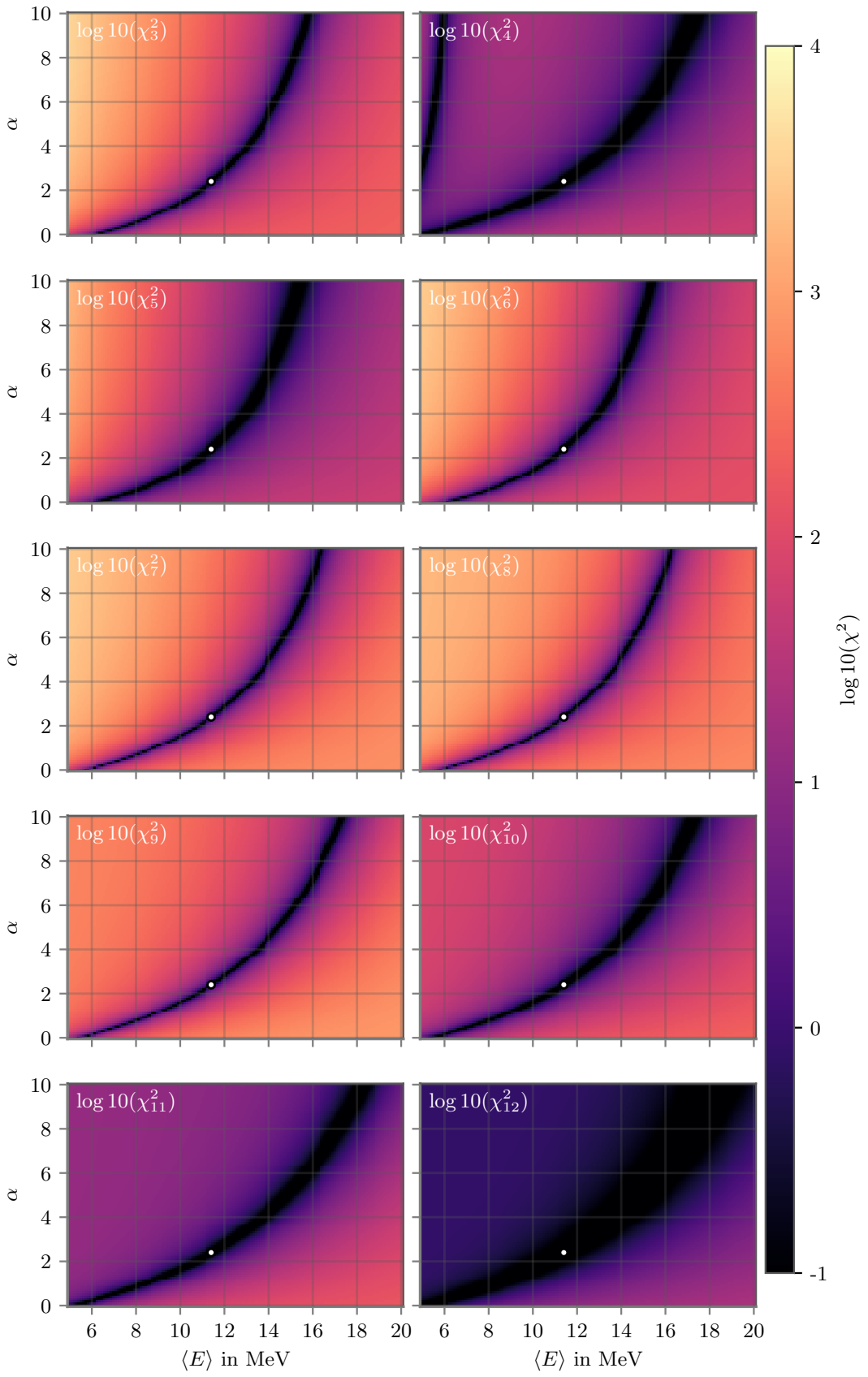

Figure 5.13: Single χ^2_j maps for $j = 3, \ldots, 12$. The transition of the ratio map R_4 results into a double valley structure in χ^2_4.

The uncertainty of the ratios is given by:

$$\sigma(R_j) = \sqrt{\left(\frac{\sigma(N_j)}{\sum_{i=3}^{12} N_i}\right)^2 + R_j^2 \left(\frac{\sigma(\sum_{i=3}^{12} N_i)}{\sum_{i=3}^{12} N_i}\right)^2 + \mathrm{cov}(N_j, \sum_{i=3}^{12} N_i)}, \tag{5.17}$$

where the covariance $\mathrm{cov}(N_j, \sum_{i=3}^{12} N_i))$ is

$$\mathrm{cov}(N_j, \sum_{i=3}^{12} N_i)) = -2R_j \left(\frac{\sigma(N_j)}{\sum_{i=3}^{12} N_i}\right)^2. \tag{5.18}$$

The different ratio maps are shown in Fig. 5.12. The map of R_3 shows a similar color pattern as Fig. 5.7, because the ratios R_3 and the ratios $R_{3,\geq 4}$ are simply shifted by the factor $\frac{N_{\geq 4}}{N_3+N_{\geq 4}}$ relative to each other. The ratio map of R_4 is a transition phase from low ratio values in the lower right corner to the upper left corner. The following ratio maps show how the lower values extend over the map.

As reference point for the comparison was $\langle E \rangle_{\mathrm{ref}} = 11.4\,\mathrm{MeV}$, $\alpha_{\mathrm{ref}} = 2.4$ chosen as before. The single χ^2 maps of the different R_j is shown in Fig. 5.13. The χ^2 map of R_3 is identical to the χ^2 map of the ratio $R_{3,\geq 4}$ (see Fig. 5.10). This is reasonable since in both χ^2 maps the same information is used. The χ^2 map of R_4 shows a transition with two valleys. From the ratio map of R_4 one could assume that the valley on the right correspond to the valley of the χ^2 map of R_3, while the valley on the left correspond to the valley of the χ^2 maps of R_5 and so on. This assumption gets supported by the fact that the valley at $\alpha = 10$ moves to higher $\langle E \rangle$.

Combination of the single χ^2 maps

$$\chi^2 = \sum_{j=3}^{12} \chi_j^2 \tag{5.19}$$

means that each points' number of degrees of freedom is also a combination of the single number of degrees of freedom. The number of degrees of freedom for a single point is determined as described in Sec. 5.2.2. The combined number of degrees of freedom is shown in Fig. 5.14. The number of degrees of freedom is 10 for the combination of ~ 10 χ^2 maps, therefore each map brings 1 degree of freedom into the new map.

Accordingly, the combined χ^2 map is the sum of the single χ^2 maps:

$$\chi_i^2 = \sum_{j=3}^{12} \frac{(R_{j,i} - R_{j,\mathrm{ref}})^2}{\sigma^2(R_{j,\mathrm{ref}})} \tag{5.20}$$

The χ^2 map for the combination of the ratios from 3-fold coincidence hits to 12 and higher fold coincidence hits is shown in Fig. 5.15. As the area of 68 % uncertainty region shows, the degeneracy of the single χ^2 maps is broken. The uncertainty regions are distributed around the true value.

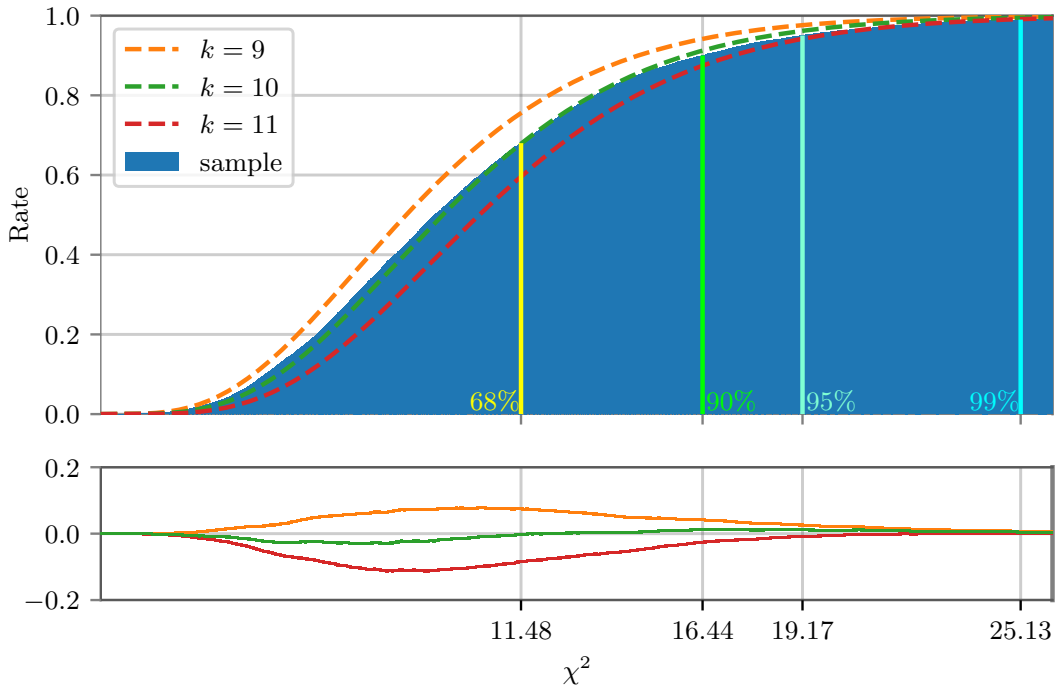

Figure 5.14: Upper: Cumulative χ^2 distribution for a point in the combined χ^2 map compared with the cumulative distribution function of $k = 9$ (orange), $k = 10$ (green) and $k = 11$ (red) degrees of freedom. Lower: Residuals of the cumulative χ^2 distribution with the theoretical curve of $k = 9$ (orange), $k = 10$ (green) and $k = 11$ (red) degrees of freedom. The values where the cumulative χ^2 distribution exceeds 68 % (yellow), 90 % (lime), 95 % (turquoise), and 99 % (cyan) are given.

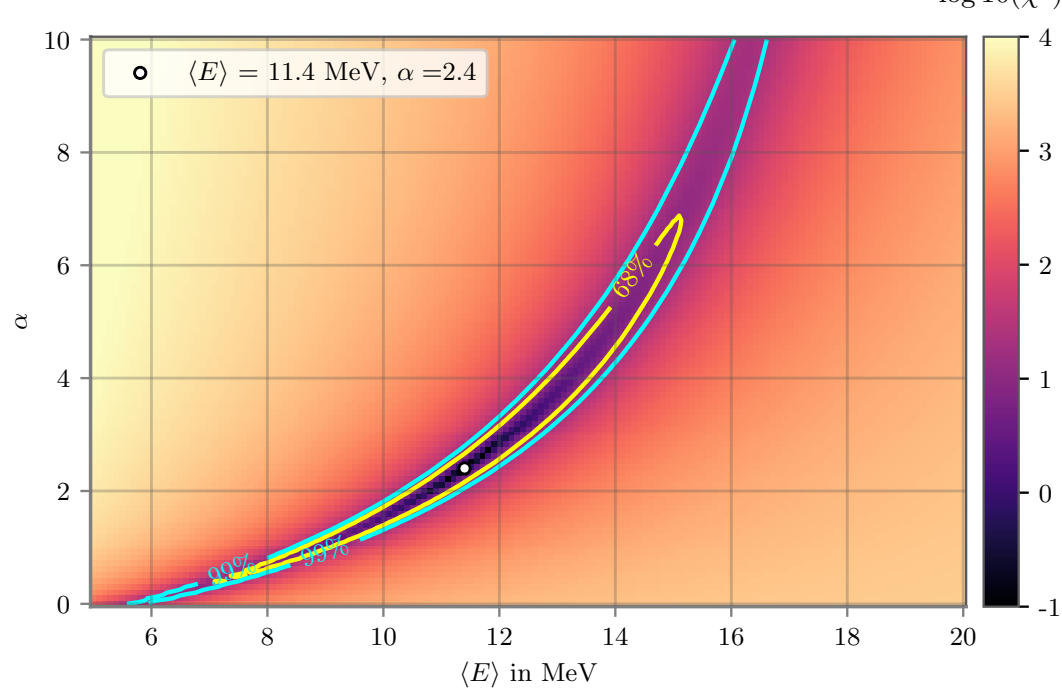

Figure 5.15: Combined χ^2 map of the comparison between the ratios from 3-fold coincidence hits to $\geq$ 12-fold coincidence hits of different parameter combinations with a reference point via a χ^2 method. The reference point ($\langle E \rangle = 11.4\,\text{MeV}$, $\alpha = 2.4$) is denoted with a white point. The 68 % confidence area is marked by a yellow line, the 99 % confidence area by a cyan line.

As in Sec. 5.2.3, the coverage gets verified as a cross-check for correct calculations. The results for 10000 Poisson generated samples the same way as described in Sec. 5.2.3 is shown in Fig. 5.16.

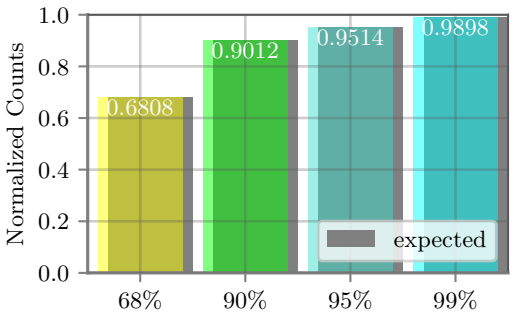

Figure 5.16: Check of the coverage of the reference point with 10000 Poisson generated histograms with its ratios as expectation values.

A further point of interest is the behaviour of the uncertainty areas at different reference points. This is studied by varying the reference point between three different reference mean energies ($\langle E \rangle_{\text{ref}} = 10.0\,\text{MeV}, 13.0\,\text{MeV}, 16.0\,\text{MeV}$) and two different reference α ($\alpha_{\text{ref}} = 2.0, 4.0$). The χ^2 maps of these six reference combinations is shown in Fig. 5.17.

A comparison of the different χ^2 maps shows that with larger $\langle E \rangle$ and smaller α the confidence areas are smaller, which means there is a better sensitivity. Hereby, the effect of the α parameter seems to be larger than the effect of $\langle E \rangle$. This phenomena is reasonable, because the larger $\langle E \rangle$ and smaller α lead to higher counts in the n-fold coincidence histogram (see Fig. 5.6) and furthermore the neutrino distribution $f_\alpha(E)$ is thinner for smaller α which means the differentiation between the spectra is easier.

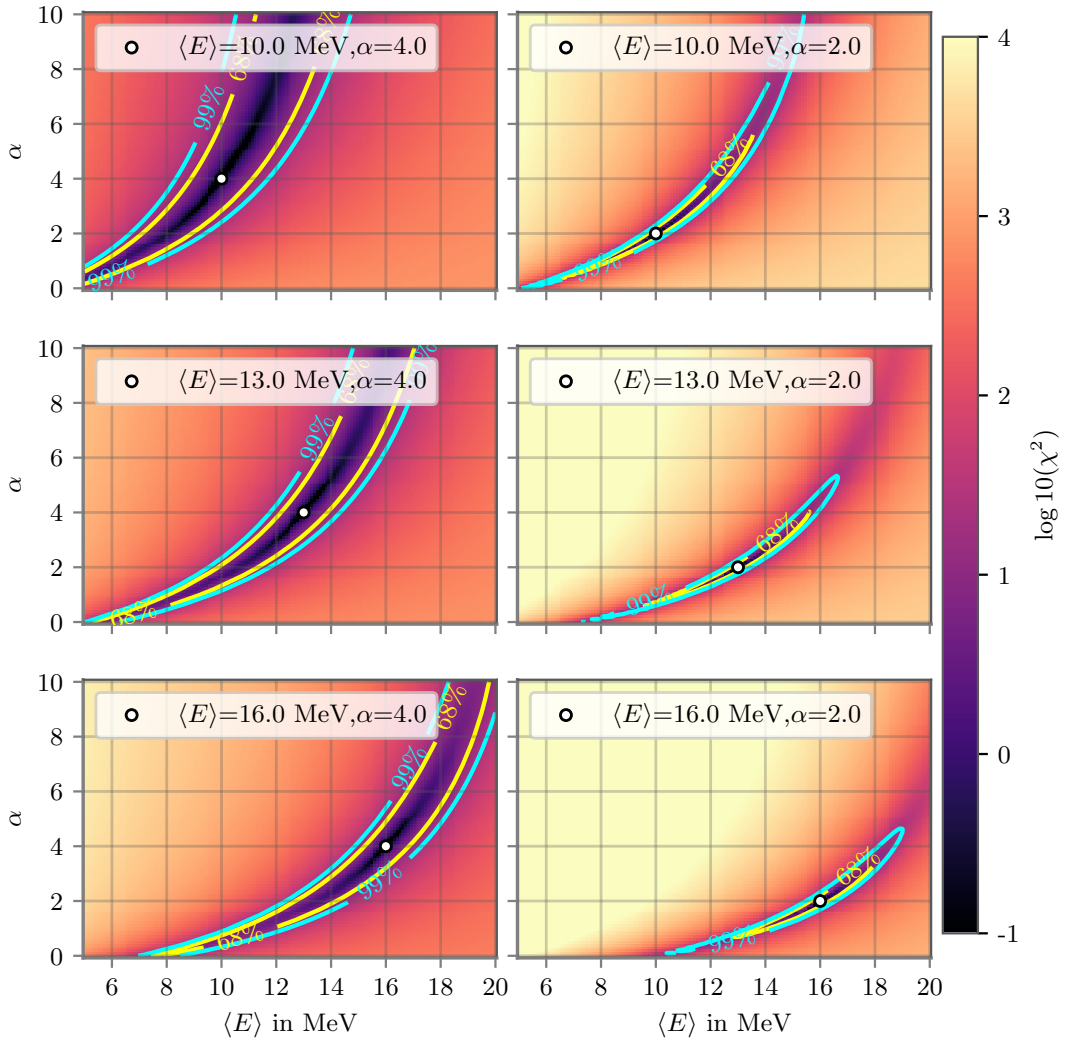

Figure 5.17: Combined χ^2 maps for different reference points. $\langle R \rangle_{\text{ref}}$ varies between 10.0 MeV (top), 13.0 MeV (center) and 16.0 MeV (bottom). α varies between 2.0 (right) and 4.0 (left). The 68 % confidence area is marked by a yellow line, the 99 % confidence area by a cyan line.

5.3.2 Marginalization for Optimization of Sensitivity Map

To determine the goodness of the used combination it is necessary to introduce a reasonable method to characterize the confidence area. For that the χ^2 map is cut along each $\langle E \rangle$ and α. From each cut the minimum is taken individually. The result of this method, which in this work is named marginalization process, is shown in Fig. 5.18. This marginalization leads to a curve of minima for both parameters. Both curves have their minimum at the reference point. The confidence level intervals also hold true for both curves. The 68 % confidence level interval will be called $\sigma_{\langle E \rangle}$, respectively σ_α.

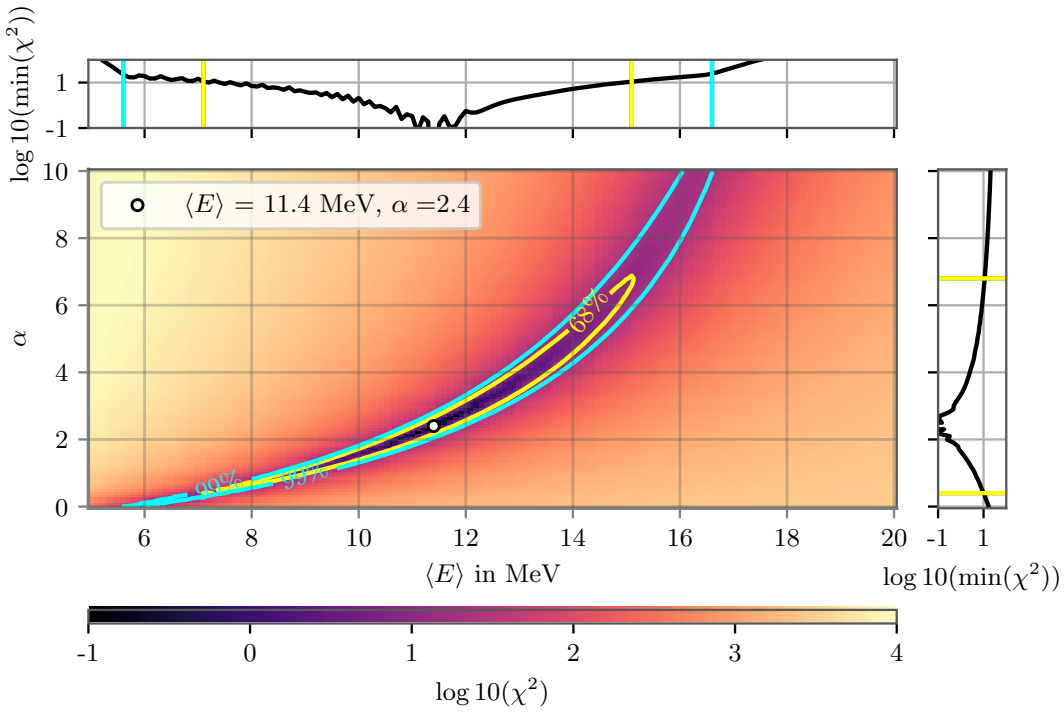

Figure 5.18: Combined χ^2 map of the comparison between the ratios from $x = 3$-fold coincidence hits to $y \geq 12$-fold coincidence hits of different parameter combinations with a reference point via a χ^2 method. The reference point ($\langle E \rangle = 11.4\,\text{MeV}$, $\alpha = 2.4$) is denoted with a white point. Above the map the marginalization of $\langle E \rangle$, right to the map the marginalization of α are depicted. The 68 % confidence area is marked by a yellow line, the 99 % confidence area by a cyan line.

Different combinations of x- and y-fold coincidence hits, where x is the lowest and y the highest coincidence hits, can be now classified by their goodness using this marginalization process. All χ^2 maps with marginalization of different combinations give a value for $\sigma_{<E>}$ and for σ_α which are denoted in Tab. 5.1 and depicted in Fig. 5.19. Since the χ^2 map is limited to $\alpha = 10.0$ the values for $\sigma_{\langle E \rangle}$ can be cut off. So $\sigma_{\langle E \rangle}$ can only be treated as lower boundary in these cases.

For all different x-fold coincidences the best combination is with the $y \geq 9$-fold coincidence followed by larger y coincidences up to $y \geq 12$-fold coincidences. The only exception appears for $x = 2, y \geq 7$ and $x = 2, y \geq 8$ which have lower $\sigma_{\langle E \rangle}$ than $x = 2, y \geq 12$. For $x = 3$-fold coincidences it shows that the $y \geq 7$ coincidence has lower $\sigma_{\langle E \rangle}$ and σ_α than $y \geq 8$. With exception of $x = 1$- and $x = 7$-fold coincidences, the $\sigma_{\langle E \rangle}$ and σ_α values of the same y coincidence follow $x = 2$ smaller than $x = 3$ smaller than $x = 4$ and so on. The best performing combination is $x = 2, y \geq 9$, which is shown in Fig. 5.20. As comparison $x = 3, y \geq 9$ is shown in Fig. 5.21. It shows the same form of the confidence areas. The difference between the two combinations are the extensions of the confidence areas. They are

Comb. x, y	$\sigma_{\langle E \rangle}$ **in MeV**	σ_α	**Comb.** x, y	$\sigma_{\langle E \rangle}$ **in MeV**	σ_α	**Comb.** x, y	$\sigma_{\langle E \rangle}$ **in MeV**	σ_α
$1, \geq 3$	≥ 10.0	≥ 10.0	$2, \geq 12$	7.1	5.5	$5, \geq 9$	9.6	6.6
$1, \geq 4$	≥ 9.9	≥ 10.0	$3, \geq 5$	≥ 10.3	≥ 10.0	$5, \geq 10$	10.0	7.2
$1, \geq 5$	≥ 9.8	≥ 10.0	$3, \geq 6$	≥ 10.4	≥ 10.0	$5, \geq 11$	10.2	7.5
$1, \geq 6$	≥ 9.8	≥ 10.0	$3, \geq 7$	8.1	6.9]	$5, \geq 12$	10.4	8.1
$1, \geq 7$	9.6	9.7	$3, \geq 8$	8.6	7.4	$6, \geq 8$	≥ 11.9	≥ 10.0
$1, \geq 8$	8.8	7.9	$3, \geq 9$	6.8	5.3	$6, \geq 9$	10.3	7.0
$1, \geq 9$	6.9	5.7	$3, \geq 10$	7.3	5.8	$6, \geq 10$	10.7	7.8
$1, \geq 10$	7.2	6.0	$3, \geq 11$	7.7	6.1	$6, \geq 11$	11.0	8.2
$1, \geq 11$	7.4	6.1	$3, \geq 12$	8.0	6.4	$6, \geq 12$	11.4	9.0
$1, \geq 12$	7.5	6.4	$4, \geq 6$	≥ 10.8	≥ 10.0	$7, \geq 9$	9.8	5.8
$2, \geq 4$	≥ 9.4	≥ 10.0	$4, \geq 7$	≥ 10.7	≥ 10.0	$7, \geq 10$	10.4	6.6
$2, \geq 5$	8.9	8.7	$4, \geq 8$	≥ 10.8	≥ 10.0	$7, \geq 11$	10.7	7.1
$2, \geq 6$	8.2	7.5	$4, \geq 9$	8.2	6.2	$7, \geq 12$	11.1	7.8
$2, \geq 7$	6.5	5.4	$4, \geq 10$	8.9	6.8	$8, \geq 10$	≥ 15.0	≥ 10.0
$2, \geq 8$	7.0	5.6	$4, \geq 11$	9.4	7.1	$8, \geq 11$	≥ 15.0	≥ 10.0
$2, \geq 9$	6.1	4.6	$4, \geq 12$	9.9	7.7	$8, \geq 12$	15.0	≥ 10.0
$2, \geq 10$	6.5	5.0	$5, \geq 7$	≥ 11.1	≥ 10.0	$9, \geq 11$	≥ 15.0	≥ 10.0
$2, \geq 11$	6.6	5.1	$5, \geq 8$	≥ 11.3	≥ 10.0	$9, \geq 12$	≥ 15.0	≥ 10.0

Table 5.1: Table of $\sigma_{\langle E \rangle}$ and σ_α for different x, y combinations. x, y indicate the lowest and highest coincidence hits taken into account.

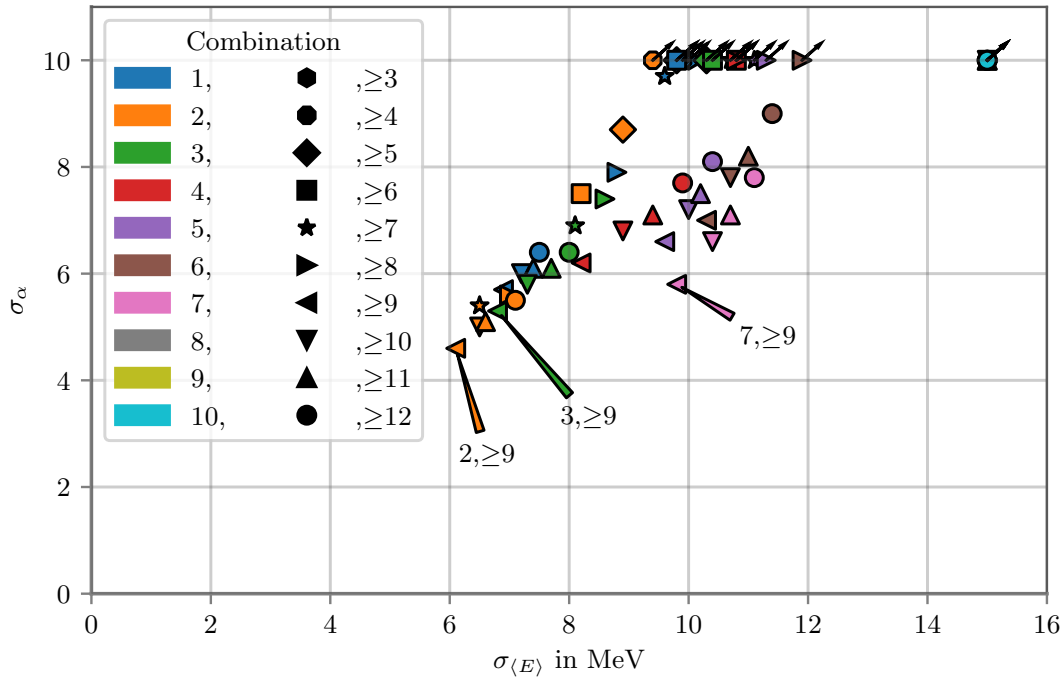

Figure 5.19: Scatter plot of $\sigma_{\langle E\rangle}$ and σ_α for different combinations. The x-fold coincidence hits are coloured differently, while the y-fold coincidence hits are depicted in different symbols. The arrows indicate that the given values are only a lower boundary. The combination $2, \geq 9$, $3, \geq 9$, and $7, \geq 9$ are marked.

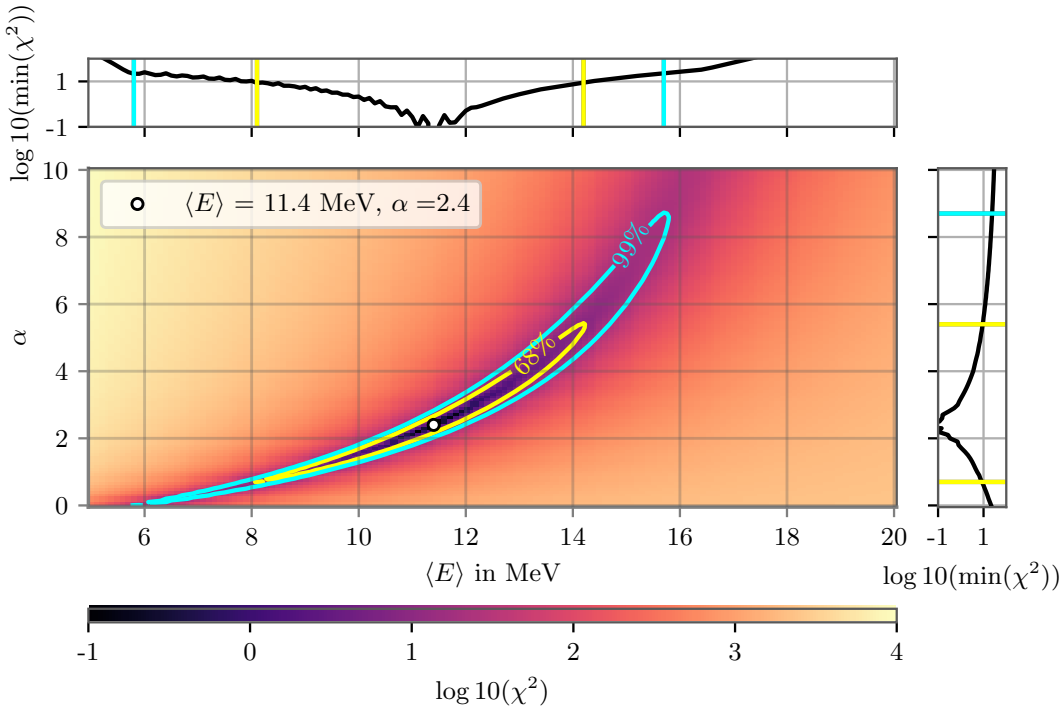

Figure 5.20: Combined χ^2 map of the comparison between the ratios from $x = 2$-fold coincidence hits to $y \geq 9$-fold coincidence hits with a reference point ($\langle E\rangle = 11.4\,\text{MeV}$, $\alpha = 2.4$, denoted by a white circle) via a χ^2 method. $\sigma_{\langle E\rangle}$ and σ_α are depicted above and right of the map.

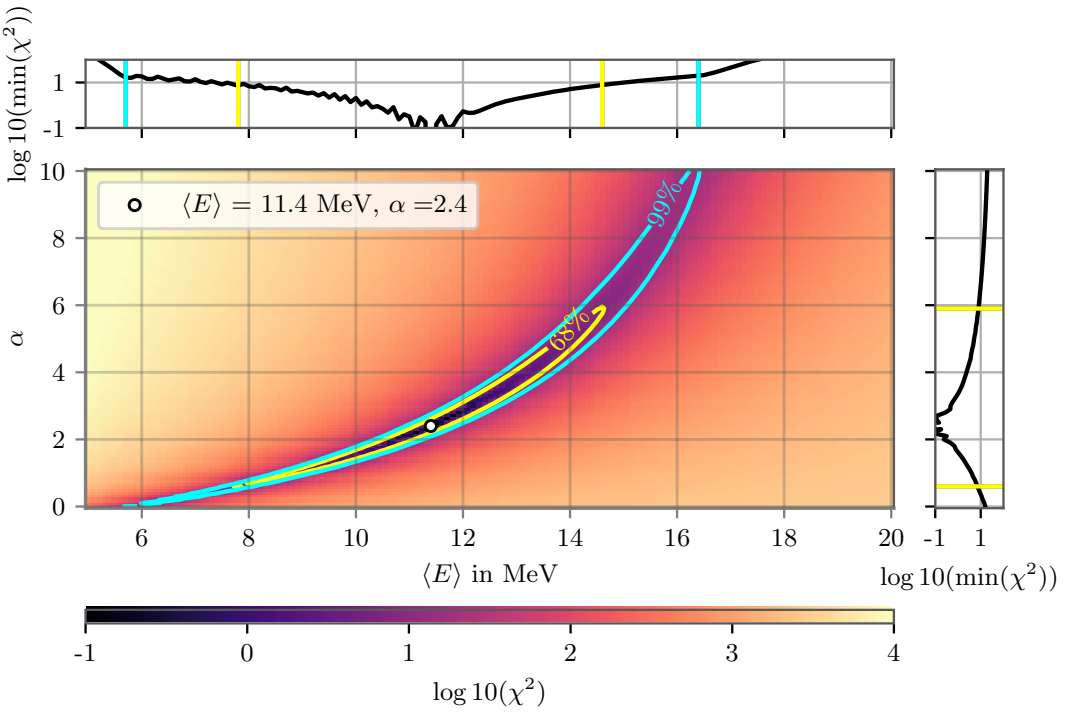

Figure 5.21: Combined χ^2 map of the comparison between the ratios from $x = 3$-fold coincidence hits to $y \geq 9$-fold coincidence hits with a reference point ($\langle E \rangle = 11.4\,\text{MeV}$, $\alpha = 2.4$, denoted by a white circle) via a χ^2 method. $\sigma_{\langle E \rangle}$ and σ_α are depicted above and right of the map.

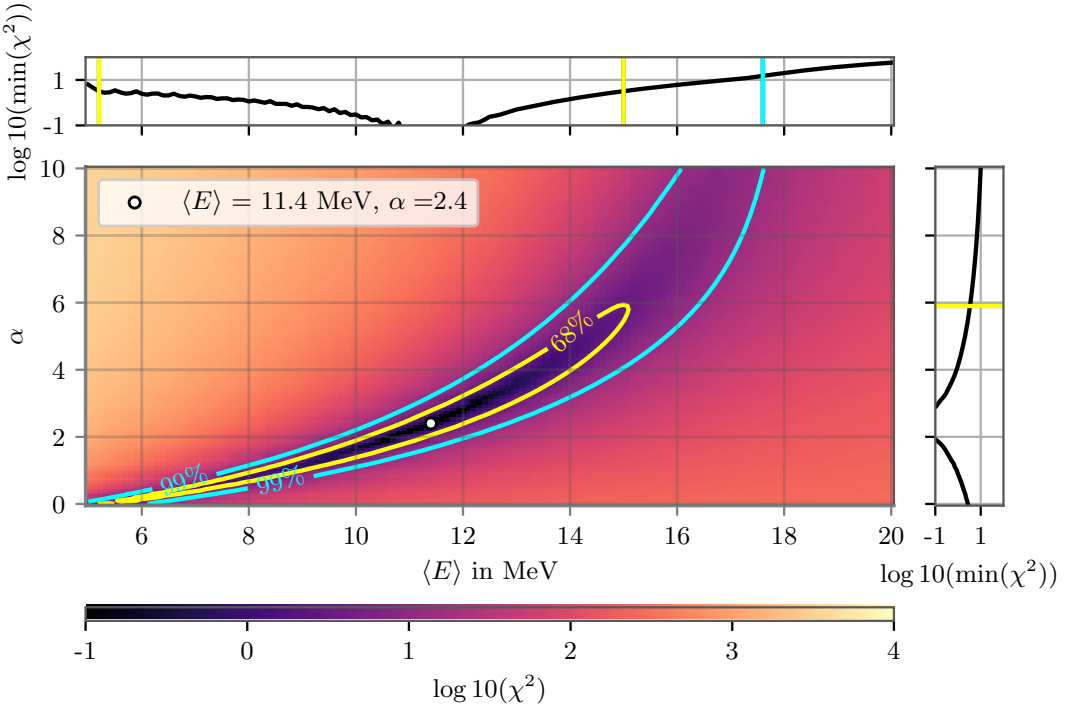

Figure 5.22: Combined χ^2 map of the comparison between the ratios from $x = 7$-fold coincidence hits to $y \geq 9$-fold coincidence hits with a reference point ($\langle E \rangle = 11.4\,\text{MeV}$, $\alpha = 2.4$, denoted by a white circle) via a χ^2 method. $\sigma_{\langle E \rangle}$ and σ_α are depicted above and right of the map.

more stretched for $x = 3, y \geq 9$ which results into larger $\sigma_{\langle E \rangle}$ and larger σ_α. The special case $x = 7, y \geq 9$, which breaks the rule of larger σ_α for the same stop coincidence, is shown in Fig. 5.22 as well. Its confidence areas have a wider form than the ones from the combinations before, which results into a larger $\sigma_{\langle E \rangle}$. Besides, the σ_α is cut away at the lower end of the map and it might therefore be larger.

Since $x = 2, y \geq 9$ is the best performing combination, the further studies were done with this combination.

5.3.3 Performance for Different SN Distances and Detector Configurations

With the best performing combination the distance of the SN and the amount of mDOMs in a detector can be varied and the behaviour of the χ^2 maps compared. It is done as in Sec. 5.3.2 using $\sigma_{\langle E \rangle}$ and σ_α. First, it is checked whether χ^2 maps depend on the distance of the ratio maps. Therefore, the ratio maps and the χ^2 maps of 10.0 kpc and 20.0 kpc are shown in Fig. 5.23, 5.24, 5.25, and 5.26. The ratio maps of the different SN distances do not differ from each other, but the χ^2 maps do. This means that different distances do not influence the ratios, only the χ^2 resolution since the signal of the reference point differs. The same holds for different amounts of mDOMs in a detector.

To check the influence of the SN distance to the resolution of this method, SN distances from 5.0 to 20.0 kpc with a step size of 1.0 kpc and a SN distance of 50.0 kpc were studied. The scatter plot for $\sigma_{\langle E \rangle}$ and σ_α is shown in Fig. 5.27.

Up to a SN distance of 14.0 kpc, $\sigma_{\langle E \rangle}$ and σ_α can be determined with the used method. There is a decrease of $\sigma_{\langle E \rangle}$ and σ_α when the SN is nearer. Although this decrease looks for SNe between 14.0 kpc and 10.0 kpc quite steady, it becomes less as closer the SN is. To compare the sensitivity for a 5.0 kpc distant SN, the χ^2 map with marginalization is shown in Fig. 5.28.

In order to study the effects of a different amount of mDOMs in the detector on the sensitivity, $\sigma\langle E \rangle$ and σ_α from the marginalization of χ^2 maps from 500 to 15 000 modules were considered while the SN distance is 10 kpc in all cases. The overview is given in Fig. 5.29. This method results in defined $\sigma_{\langle E \rangle}$ and σ_α up to a detector configuration with 2000 mDOMs. The χ^2 map with marginalization of a detector where the amount of mDOMs would be increased by 50 % of the original 10 000 modules is shown in Fig. 5.30. Its $\sigma_{\langle E \rangle}$, σ_α would not be smaller than for a detector with 10 000 modules where the SN has been 9.0 kpc distant (see Fig. 5.27).

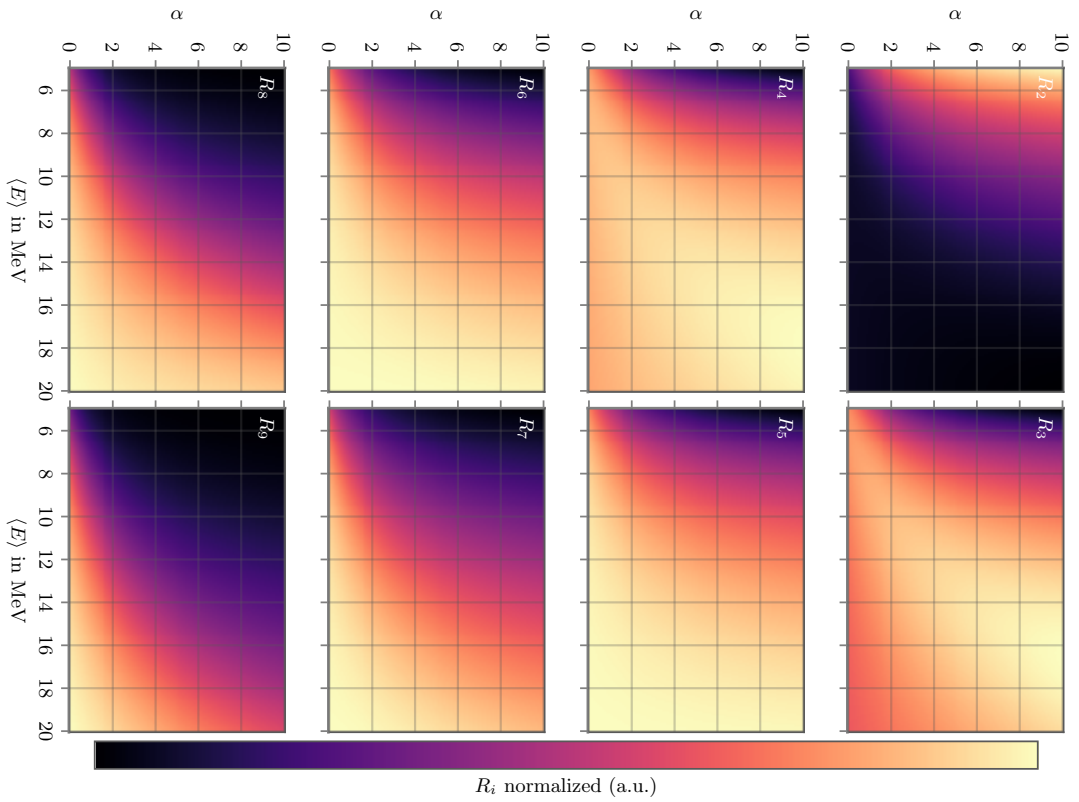

Figure 5.23: Single ratio maps of R_j for $j = 2, \ldots, 9$ for a SN distance of 10.0 kpc.

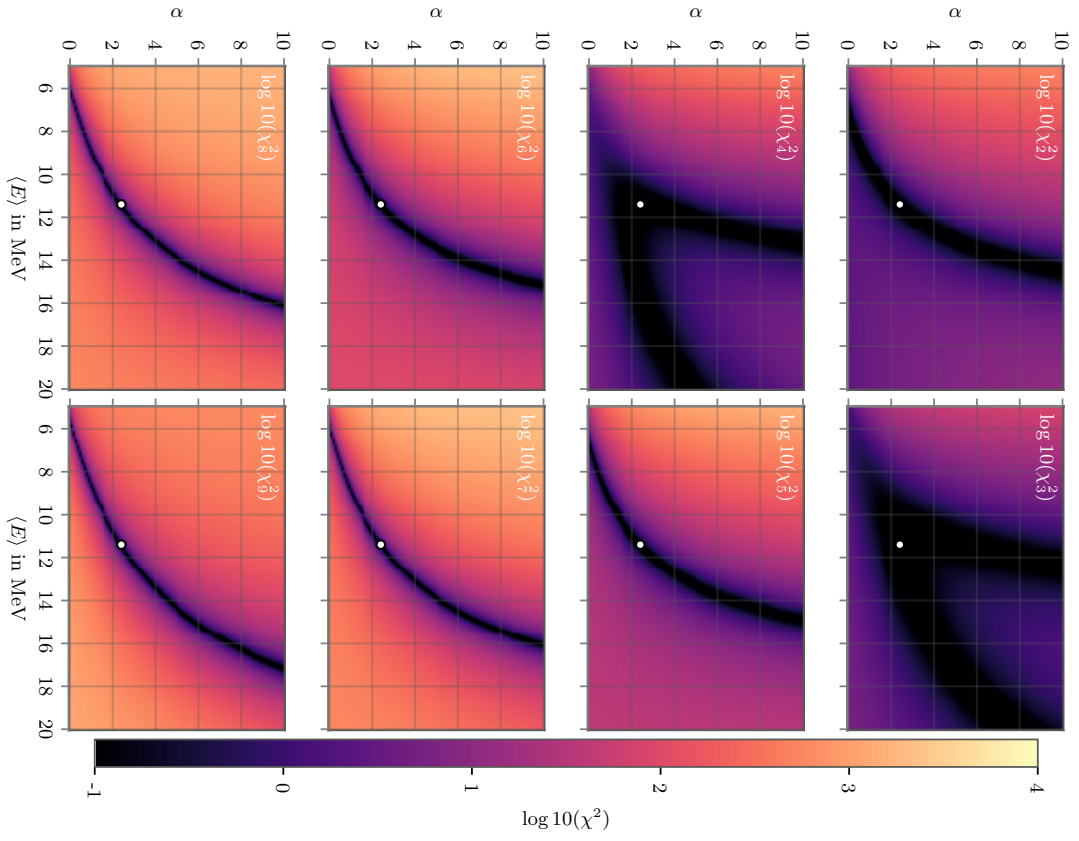

Figure 5.24: Single χ^2 maps of R_j for $j = 2, \ldots, 9$ for a SN distance of 10.0 kpc.

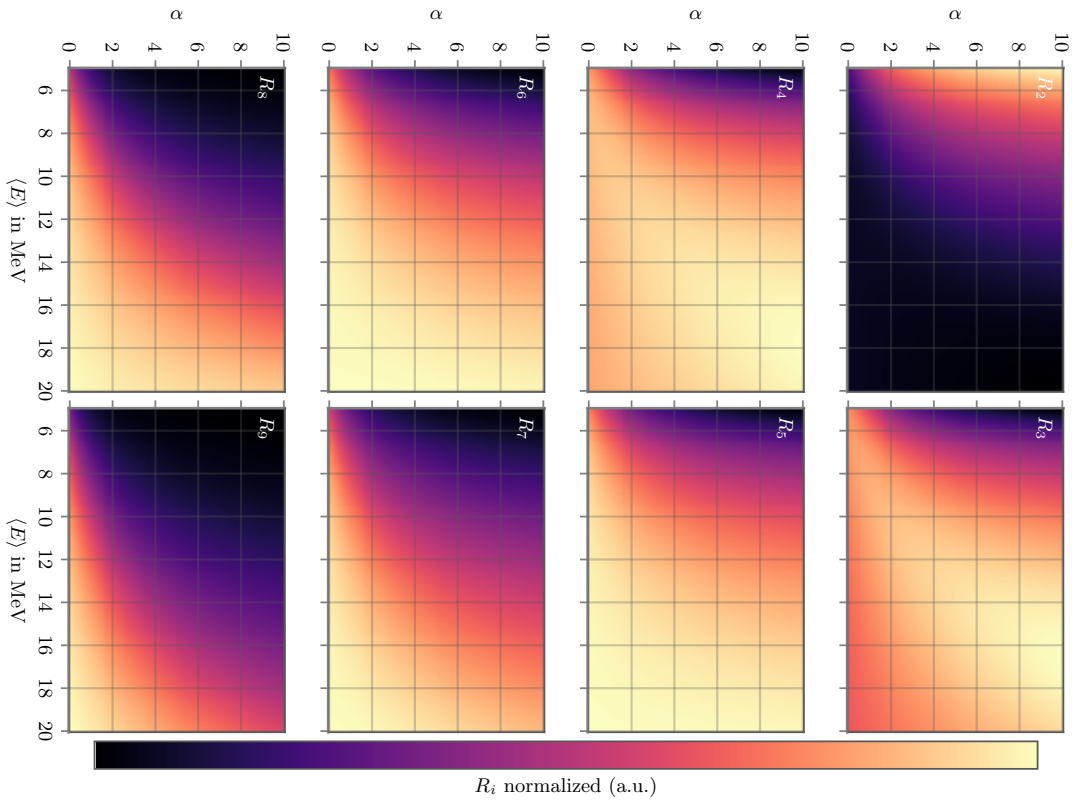

Figure 5.25: Single ratio maps of R_j for $j = 2, \ldots, 9$ for a SN distance of 20.0 kpc.

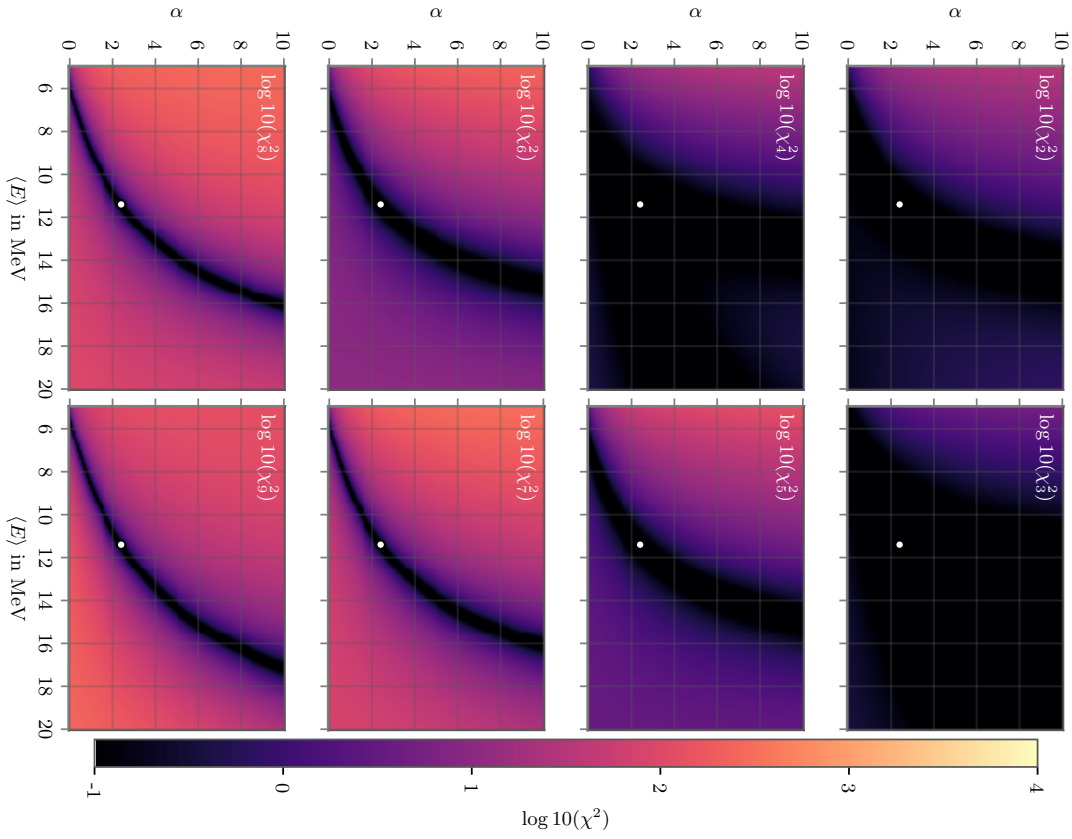

Figure 5.26: Single χ^2 maps of R_j for $j = 2, \ldots, 9$ for a SN distance of 20.0 kpc.

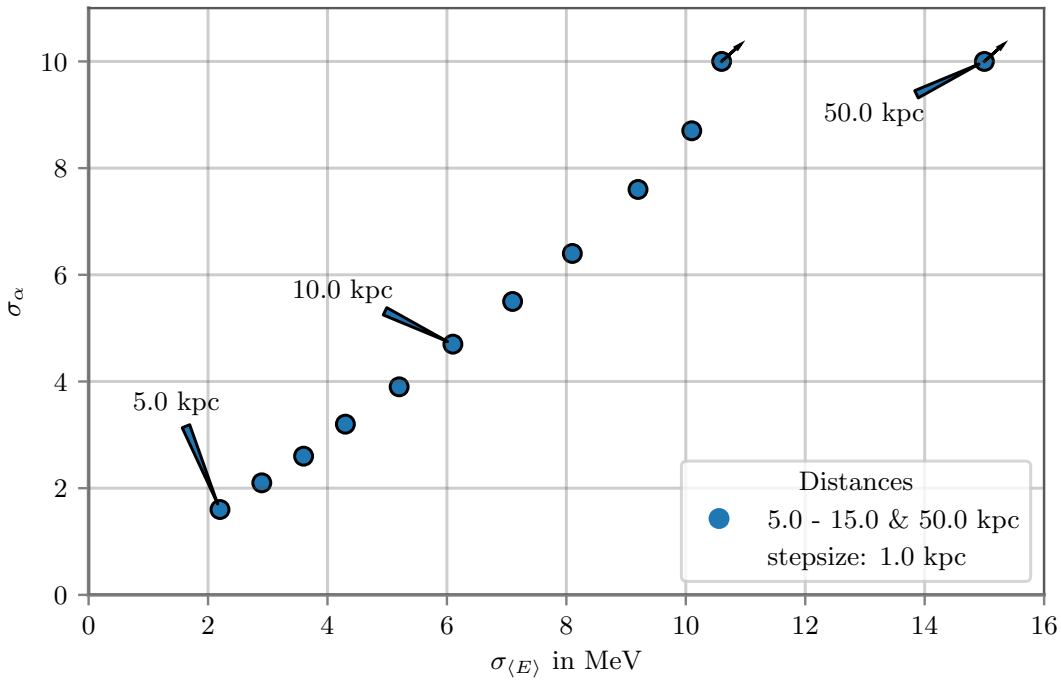

Figure 5.27: Scatter plot of $\sigma_{\langle E\rangle}$ and σ_α for SN distances between 5.0 kpc and 20.0 kpc with step size of 1.0 kpc, and a SN distance of 50.0 kpc. The SN distances of 5.0 kpc, 10.0 kpc, and 50.0 kpc are marked.

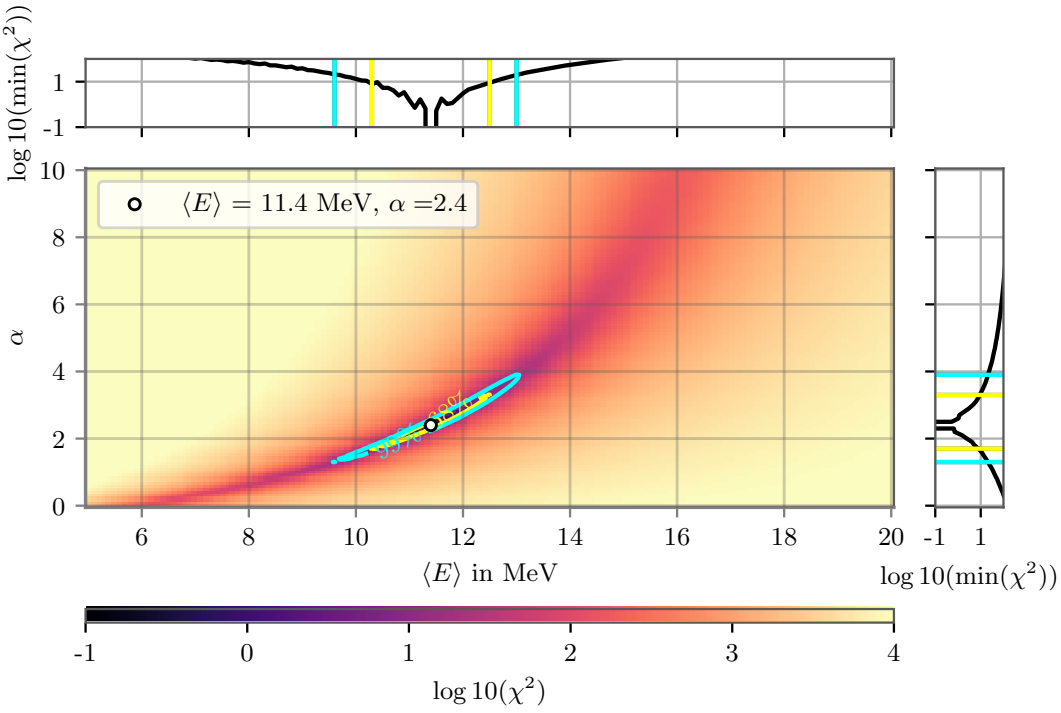

Figure 5.28: Combined χ^2 map of the comparison between the ratios from $x = 2$-fold coincidence hits to $y \geq 9$-fold coincidence hits with a reference point ($\langle E\rangle$ = 11.4 MeV, $\alpha = 2.4$, denoted by a white circle) of a SN in 5.0 kpc distance via a χ^2 method. $\sigma_{\langle E\rangle}$ and σ_α are depicted above and right of the map.

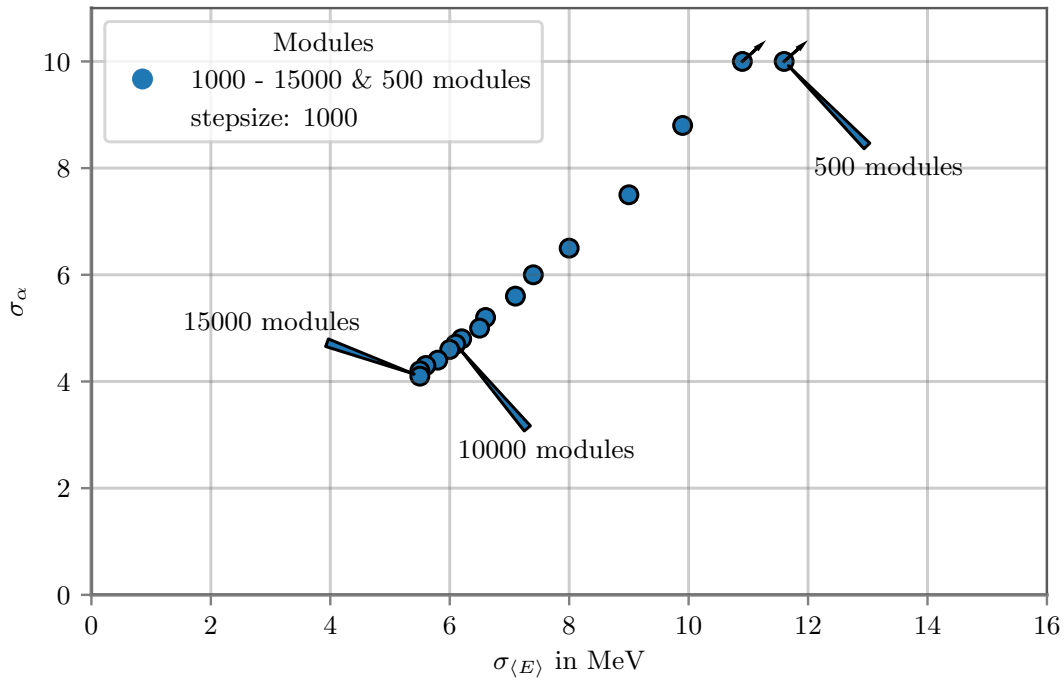

Figure 5.29: Scatter plot of $\sigma_{\langle E\rangle}$ and σ_α for detectors with 1000 to 15 000 modules with step size of 1000 modules, and a detector with 500 modules. Detectors with 15 000, 10 000, and 500 modules are marked.

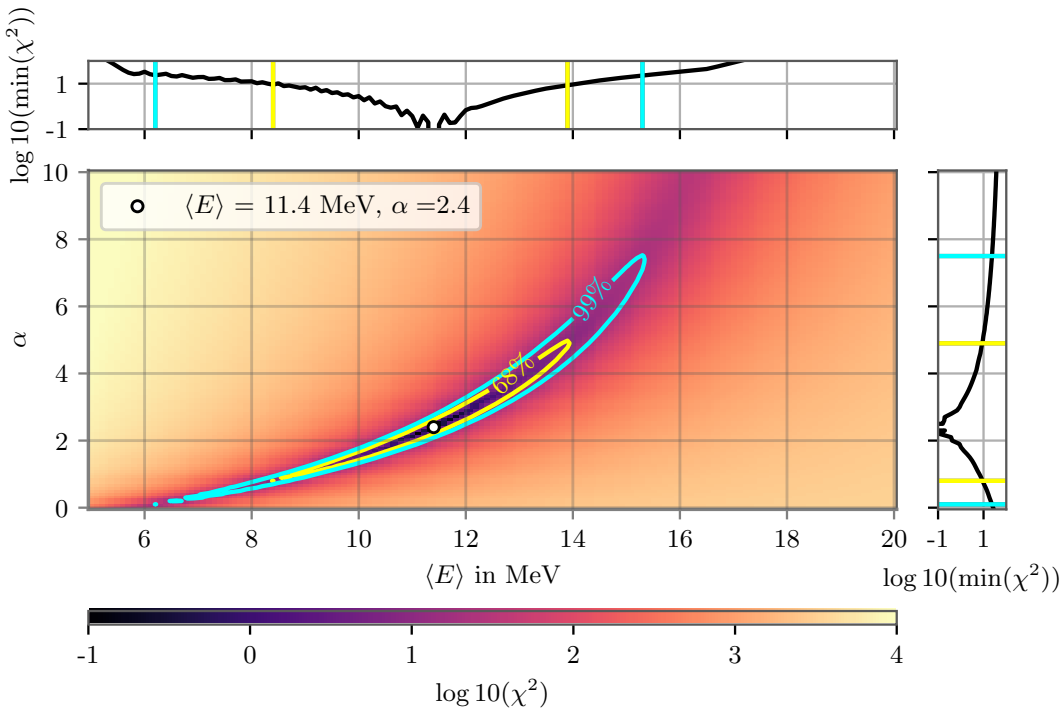

Figure 5.30: Combined χ^2 map of the comparison between the ratios from $x = 2$-fold coincidence hits to $y \geq 9$-fold coincidence hits with a reference point ($\langle E\rangle$ = 11.4 MeV, $\alpha = 2.4$, denoted by a white circle) for a detector with 15 000 mDOMs via a χ^2 method. $\sigma_{\langle E\rangle}$ and σ_α are depicted above and right of the map.

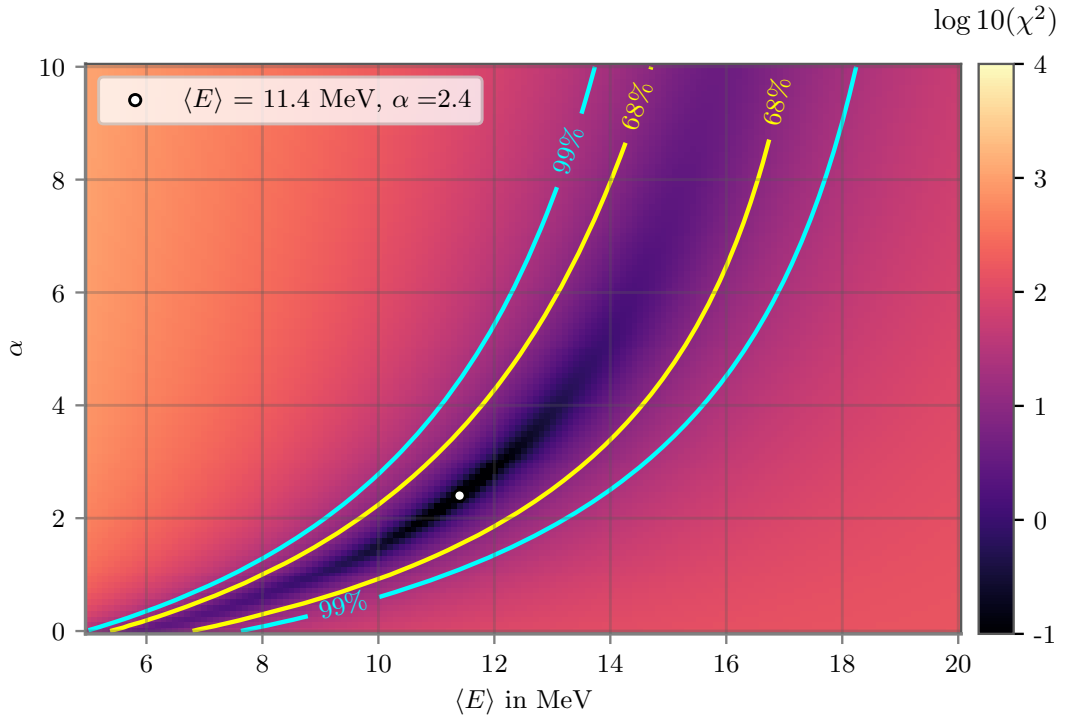

Figure 5.31: Combined χ^2 map of the comparison between the ratios from $x = 2$-fold coincidence hits to $y \geq 9$-fold coincidence hits with a reference point ($\langle E \rangle = 11.4\,\text{MeV}$, $\alpha = 2.4$, denoted by a white circle) for a detector with 500 mDOMs and a SN in 10 kpc distance via a χ^2 method.

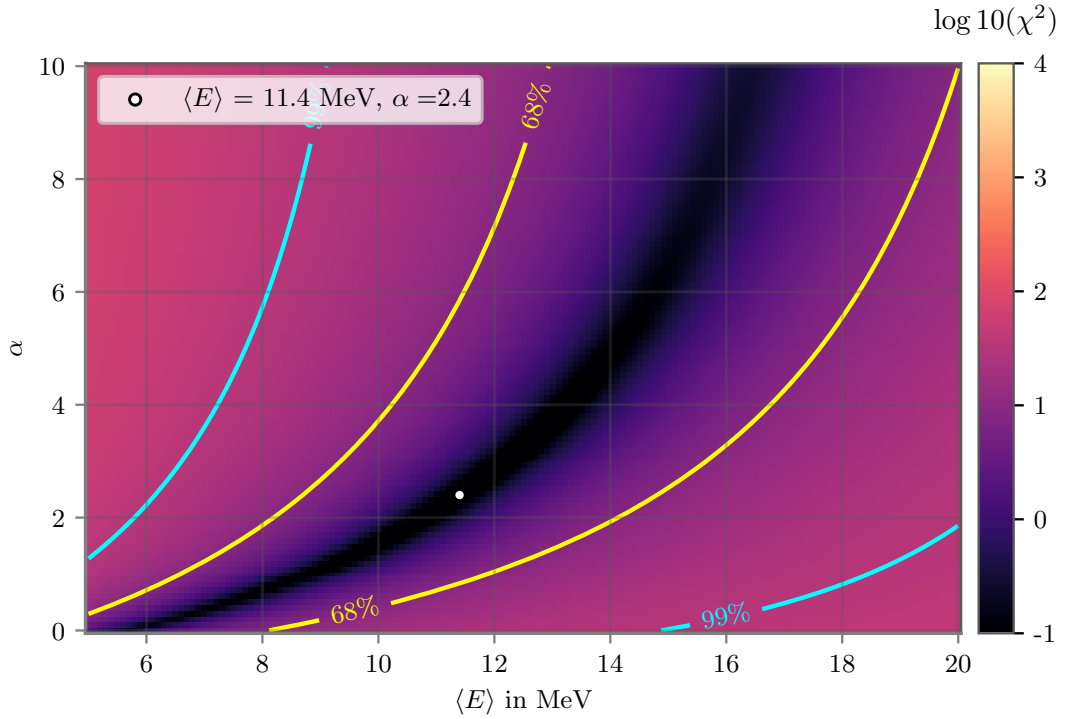

Figure 5.32: Combined χ^2 map of the comparison between the ratios from $x = 2$-fold coincidence hits to $y = 9$-fold coincidence hits with a reference point ($\langle E \rangle = 11.4\,\text{MeV}$, $\alpha = 2.4$, denoted by a white circle) for a detector with 1000 mDOMs and a SN in 45 kpc via a χ^2 method.

Of special interest is a detector with 500 mDOMs as it is proposed for the IceCube-Upgrade (see Sec. 3.5). Its χ^2 map (Fig. 5.31) does not give either a defined $\sigma_{\langle E \rangle}$, nor a defined σ_α within the used boundaries.

The comparison of a detector with 500 mDOMs for a SN in 10.0 kpc distance with a detector with 10 000 mDOMs for a SN in 45.0 kpc distance is reasonable to see the influence of both on the resolution, because the signal height of the SN neutrino histograms is approximately the same:

$$\begin{aligned} \sum_i \omega_{e,i} \cdot W_T(d = x) \cdot \omega_{\text{dist},i} &= \sum_i \omega_{e,i} \cdot W_T(n_{\text{mDOM}} = 500) \cdot \omega_{\text{dist},i} \\ W_T(d = x) &= W_T(n_{\text{mDOM}} = 500) \\ \frac{n_{\text{mDOM}}}{x^2} &= \frac{500}{d^2} \\ x &= 44.7\,\text{kpc}. \end{aligned} \tag{5.21}$$

The χ^2 map of a SN distance of 45 kpc is given in Fig. 5.32. The higher resolution for the χ^2 map of a detector 500 modules stems from the influence of the background which is smaller for less modules.

6 Neutrino Energy Spectra with Inter-Module Coincidences

The IceCube-Upgrade is planned to be composed of 500 modules. As shown in Sec. 5.3.3 the resolution to the SN neutrino energy spectra is poor in this configuration. Nevertheless its configuration allows not to consider only local coincidences, but at coincidences between different mDOMs, too. In this chapter the simulation for the inter-module coincidences is explained, and a possible method to determine the SN neutrino energy spectra resolution is studied.

6.1 Simulation of Inter-Module Coincidences

The simulation of SN neutrino spectrum in different mDOMs is as described in Ch. 4, with the only difference of the number of mDOMs. A string of 15 mDOMs was simulated in the same sized volume. Part of the string is shown in Fig. 6.1. Since the configuration earmarks 2 strings for 500 mDOMs, effects at the edges of both strings have to be taken into account. The ice properties are the same as in Ch. 4.

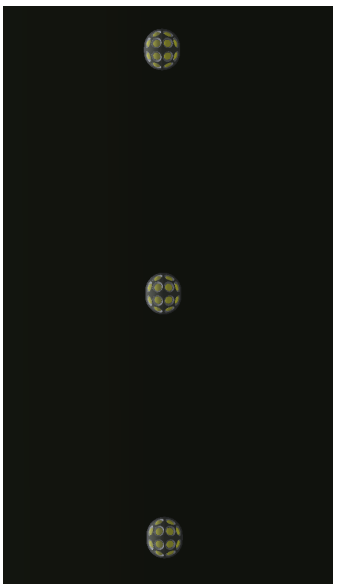

Figure 6.1: Example of 3 mDOMs on one string inside the simulation volume.

Positrons were directly generated as Sec. 4.2 from neutrinos interacting in IBDs. A flat distribution of the neutrino energy was assumed in this case to support high energetic events more than in the single mDOM simulation, therefore the events must be weighted according to the spectrum as explained in Sec. 5.1.2 using a changed distributed weight ω_{dist}:

$$\omega_{\text{dist}}(E) = A \cdot f_{\text{calc}}(E), \tag{6.1}$$

where A is a constant factor which depends on the generated events. For simplification it was chosen in such a way that the single coincidence hit of

the centered mDOM is the same as the single coincidence hit in the single mDOM simulation. This must be the case since the coincidence hits in the centered mDOM are from the same order as the coincidence hits when a single mDOM is simulated.

Events are triggered when at least one hit is detected in the centered mDOM (denoted as mDOM 0). Coincidences in the same mDOM are counted within the same time window as in the simulation for one mDOM, but for the neighbouring mDOMs new time windows need to be applied. Those time windows depend on their distance from the centered mDOM. Since the mDOMs are 2.4 m distant from each other, photons travel from mDOM to mDOM in about 10 ns. Since particles traveling with speed of light in vacuum would need around 8 ns from mDOM to mDOM, a time window of 8 to 28 ns for the nearest neighbouring mDOM was applied, because the time window stays 20 ns. Since positrons travel only some centimeters (see Sec. 3.2) giving Cherenkov photons, the time window of the next neighbouring module goes from 18 to 38 ns and so on for the further distant mDOMs.

The simulation of background was beyond the scope of this work. The calculation of coincidence hits of uncorrelated noise would be the same as described in Sec. 4.3. Background from solar neutrinos would be simulated in the same setup as the SN neutrino spectra. But for the correlated noise further investigations are required since it is unclear whether photons from radioactive decays are able to induce coincidence hits in neighbouring mDOMs.

6.2 Parameter Histograms with Neighbour Modules

For the coincidence hits in neighbouring modules a 3D representation is used. An example of the histograms including coincidence hits in neighbouring modules is shown in Fig. 6.2. The centered mDOM is noted as module number 0 (mDOM 0). A comparison with Fig. 5.4 shows the entries of mDOM 0 to be a factor of 1/20 lower which is due to the factor of 500 modules in this configuration divided by 10000 modules in the single mDOM configuration. Module number 1 and -1 are the nearest neighbours, whereas the minus sign indicates the mDOMs above mDOM 0, respectivally the + sign the ones below mDOM 0. For mDOMs above and below the centered mDOM the coincidences are symmetric because of the isotropic emitted angles of positrons from IBD, even though all neutrinos are coming from the same direction.

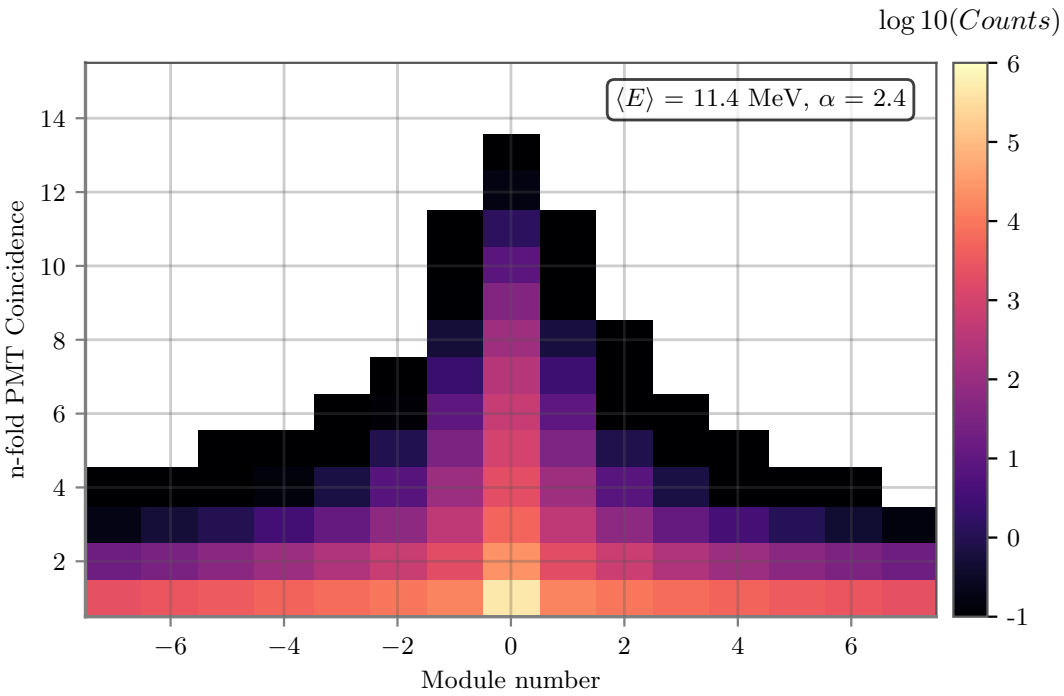

Figure 6.2: Histogram for PMT coincidence hits in neighbouring modules for $\langle E \rangle = 11.4\,\text{MeV}$, $\alpha = 2.4$. Module number 0 (the centered mDOM) indicates the trigger mDOM. The - sign stands for modules above mDOM 0, while the + sign stands for moduels below mDOM 0.

Since the mDOM 0 is the trigger mDOM, every PMT coincidence hit at the neighbouring modules requires at least one hit in mDOM 0. This means there exists no 1-fold coincidence hit as it was defined in the single mDOM configuration for the neighbouring modules.

6.3 Performance for IceCube-Upgrade Configuration

Since for a single mDOM the best performing combination is $x = 2, y \geq 9$, in the study for the neighbouring mDOMs all hits are included which have at least 2 coincidences as first approach. The best performing x and y combination might be different in this case, since the background in the inter-module case will be probably different. This means as discussed before all coincidences of the neighbouring mDOM histograms except of the mDOM 0 1-fold coincidence hits. As upper border the coincidence hits of the neighbouring mDOMs which are in the same order as the 9-fold coincidence hits from mDOM 0 are chosen. All hits that are considered in this analysis are summed up as divisor of the ratios. To distinguish the ratios from mDOM number n with m PMT coincidence hits, they are denoted as $R_{n,m}$. This gives in total 40 ratio maps which are shown

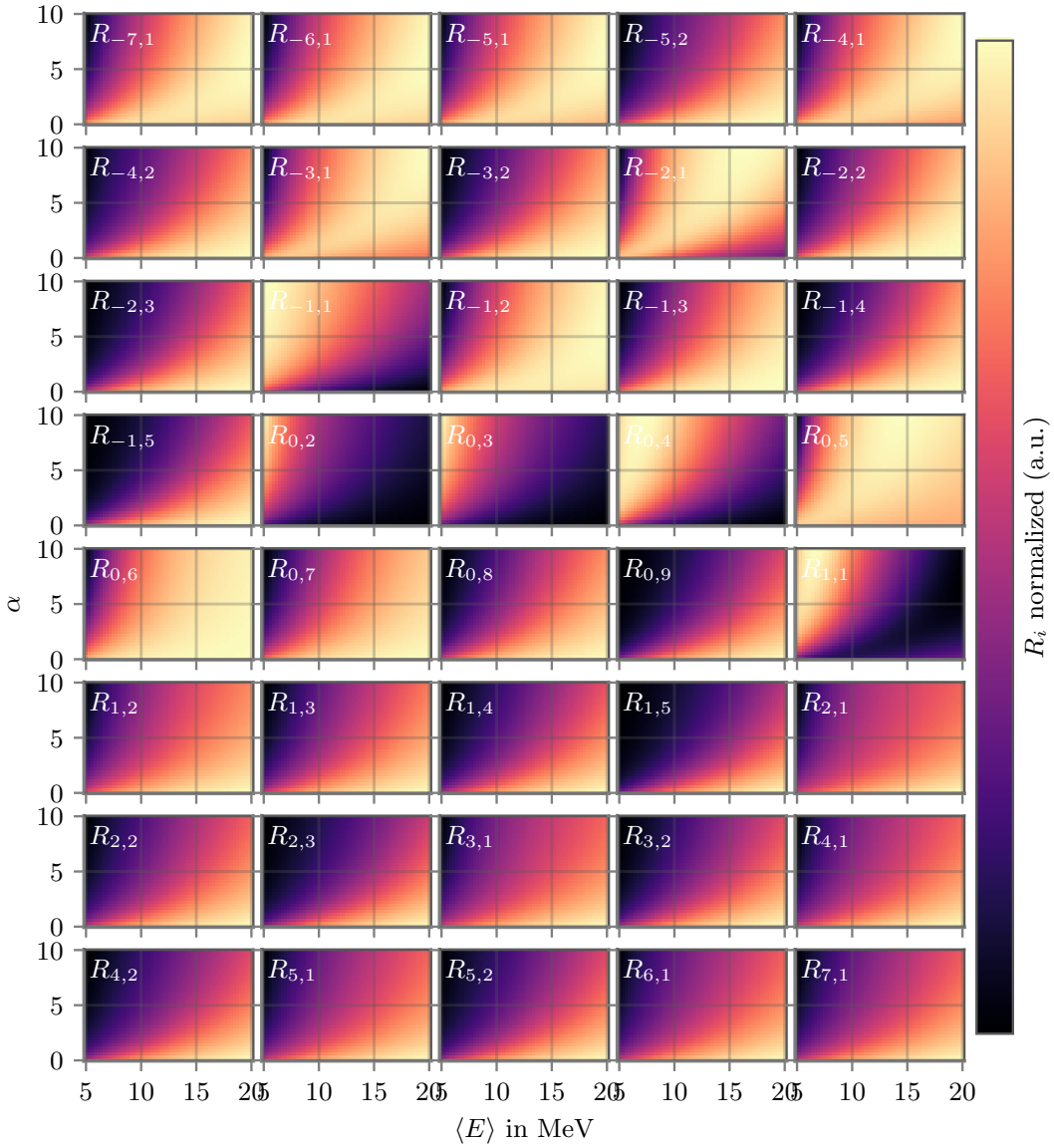

Figure 6.3: Single ratio maps of $R_{\text{mDOM,PMT Coincidence}}$. The ratios of symmetric mDOMs and same PMT coincidence hits shows different behaviours as $R_{-2,1}$ and $R_{2,1}$. Transition phases are in $R_{-2,1}$, respectively from $R_{-1,1}$ to $R_{-1,2}$, from $R_{0,4}$ to $R_{0,5}$, and from $R_{1,1}$ to $R_{1,2}$.

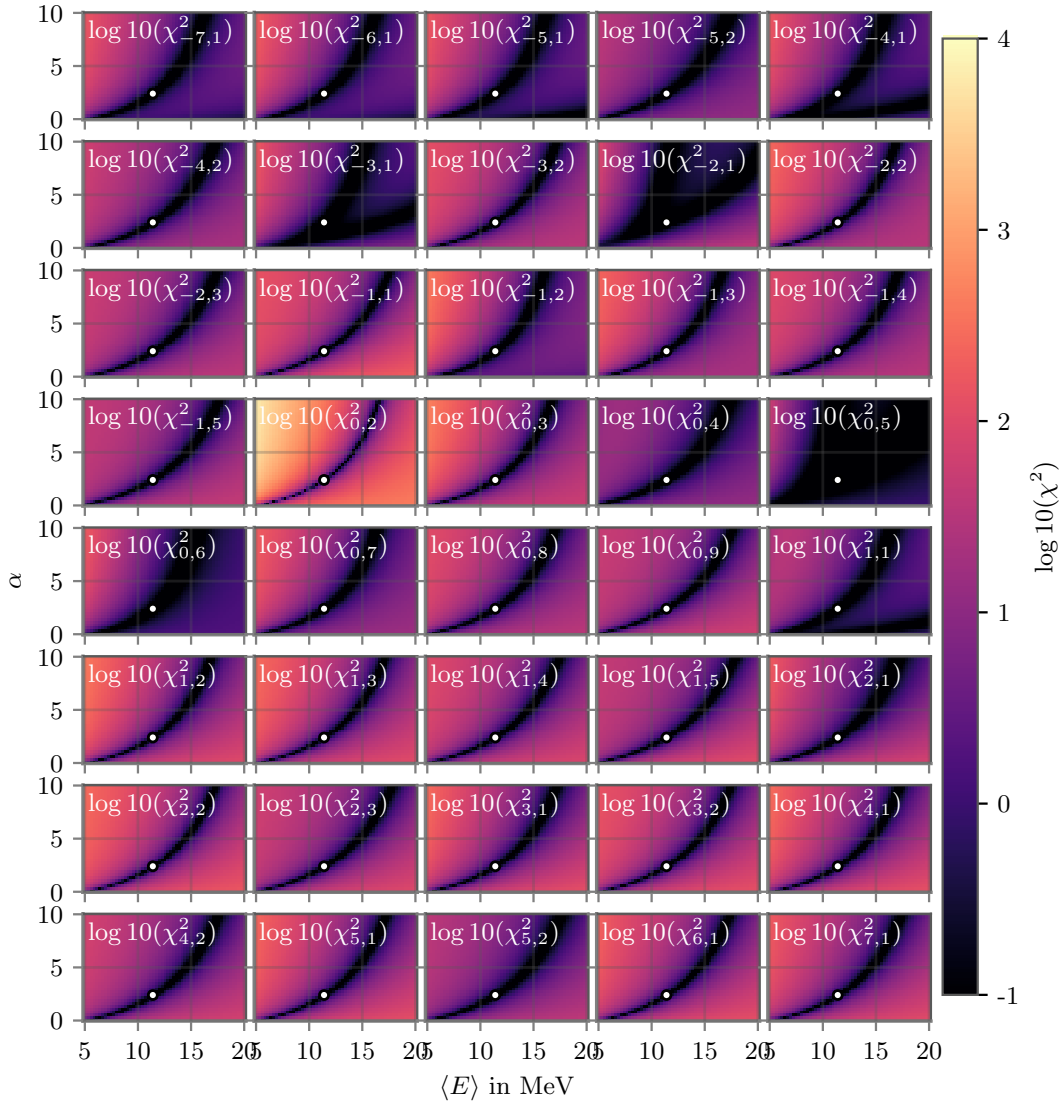

Figure 6.4: Single χ^2 maps for the different mDOMs and PMT coincidence hits. The χ^2 maps of symmetric mDOMs and same PMT coincidence hits differs as $\chi^2_{-5,1}$, $\chi^2_{-4,1}$, $\chi^2_{-3,1}$, $\chi^2_{-2,1}$, and $\chi^2_{1,1}$ show a double valley structure while their symmetric counterparts do not. The χ^2 map of 2 PMT coincidence hits in mDOM 0 shows the best resolution. The χ^2 maps of the highest chosen PMT coincidence hits of neighbouring modules show a similar resolution as $\chi^2_{0,9}$.

in Fig. 6.3. Comparing symmetric coincidence hits of the histogram shows some differences in the ratio maps for the further distant modules. So $R_{-2,1}$ shows in comparison to $R_{2,1}$ signs of a transition as R_4 does in Fig. 5.12. This transition also takes place from $R_{-1,1}$ to $R_{-1,2}$, from $R_{0,4}$ to $R_{0,5}$, and from $R_{1,1}$ to $R_{1,2}$.

As reference point the parameter $\langle E \rangle = 11.4\,\text{MeV}$, $\alpha = 2.4$ was chosen as in Ch. 6. The single χ^2 maps (Fig. 6.4) show even less symmetry between the same PMT coincidence hits. As example the width of the valley differs between $\chi^2_{-7,1}$ and $\chi^2_{7,1}$ or the double structure of the valley in $\chi^2_{-3,1}$ is vanished in $\chi^2_{3,1}$. The χ^2 maps of higher PMT coincidence hits in mDOM -1 and mDOM 1 are similar from their structure, but this breaks when it comes to the $\chi^2_{-1,1}$ and $\chi^2_{1,1}$ maps. This asymmetry is strange, because the counts of Fig. 6.2 seems to be totally symmetric. A reason for this structure might be that more likely Cherenkov light from positrons generated in interactions with higher energetic neutrinos can reach the more distant mDOMs. The interactions for these higher energetic neutrinos is no longer symmetric [57] and PMTs from mDOMs below (+ sign) the trigger module mDOM 0 are more likely hit than PMTs from mDOMs above (- sign). A justification of this hypothesis was not possible in the scope of this work.

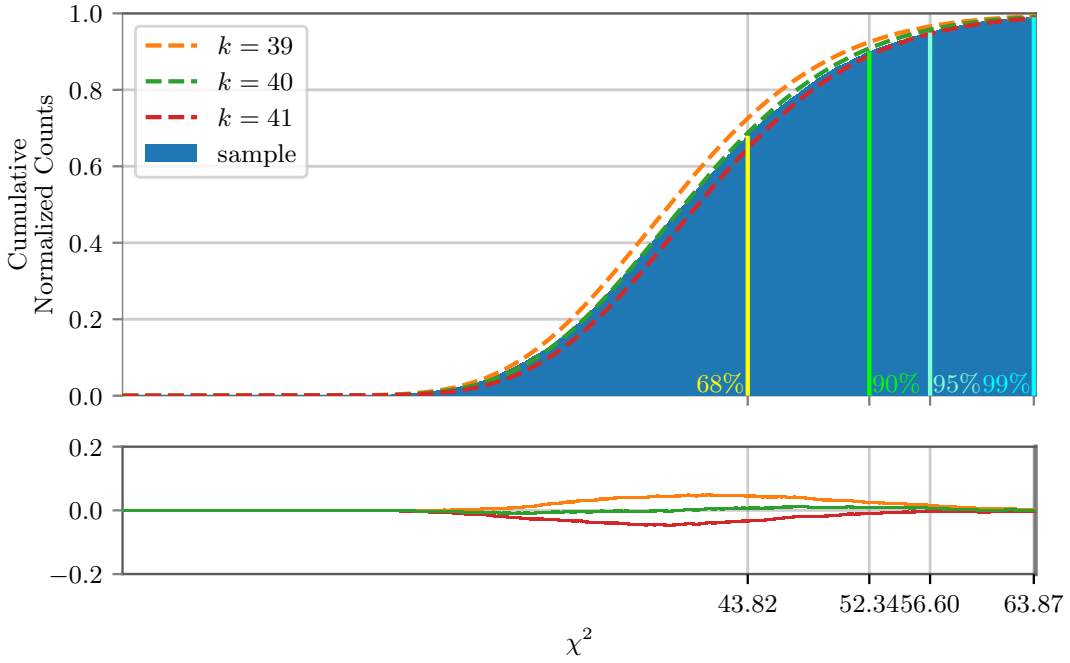

Figure 6.5: Upper: Cumulative χ^2 distribution for a point in the combined χ^2 map compared with the cumulative distribution function of $k = 39$ (orange), $k = 40$ (green) and $k = 41$ (red) degrees of freedom. Lower: Residuals of the cumulative χ^2 distribution with the theoretical curve of $k = 39$ (orange), $k = 40$ (green) and $k = 11$ (red) degrees of freedom. The values where the cumulative χ^2 distribution exceeds 68 % (yellow), 90 % (lime), 95 % (turquoise), and 99 % (cyan) are given.

The best resolution brings the χ^2 map of 2-fold coincidence hits in mDOM 0 into the analysis. One might expect this since the ratios of this case are the highest which results into larger differences between the ratios from different histograms. Since the resolution of the highest PMT coincidence χ^2 maps of the different mDOMs, as for example $\chi^2_{-7,1}$, are from a similar goodness as $\chi^2_{0,9}$, the choice of the upper limits seems to be reasonable.

In total, 40 different ratios are included in this analysis. As before, the different χ^2 maps are summed up, which gives 40 degrees of freedom to the final map which is verified in Fig. 6.5. This combined χ^2 map including inter-module coincidence hits without noise is shown in Fig. 6.6. To check how the inter-module coincidence hits improve the sensitivity of the method, this χ^2 map is compared to the combined χ^2 map including only mDOM 0 coincidence hits. This χ^2 is shown in Fig. 6.7. Since this χ^2 map is also without background noise, it differs from 5.31. The sensitivity of both single mDOM χ^2 maps does not seem to vary as much as the χ^2 map when including inter-module coincidences. This means that including the information of neighbouring modules gives a higher sensitivity towards SN neutrino energy spectra. Nevertheless, the sensitivity is way lower than the obtained one with 10 000 modules and no inter-module coincidences.

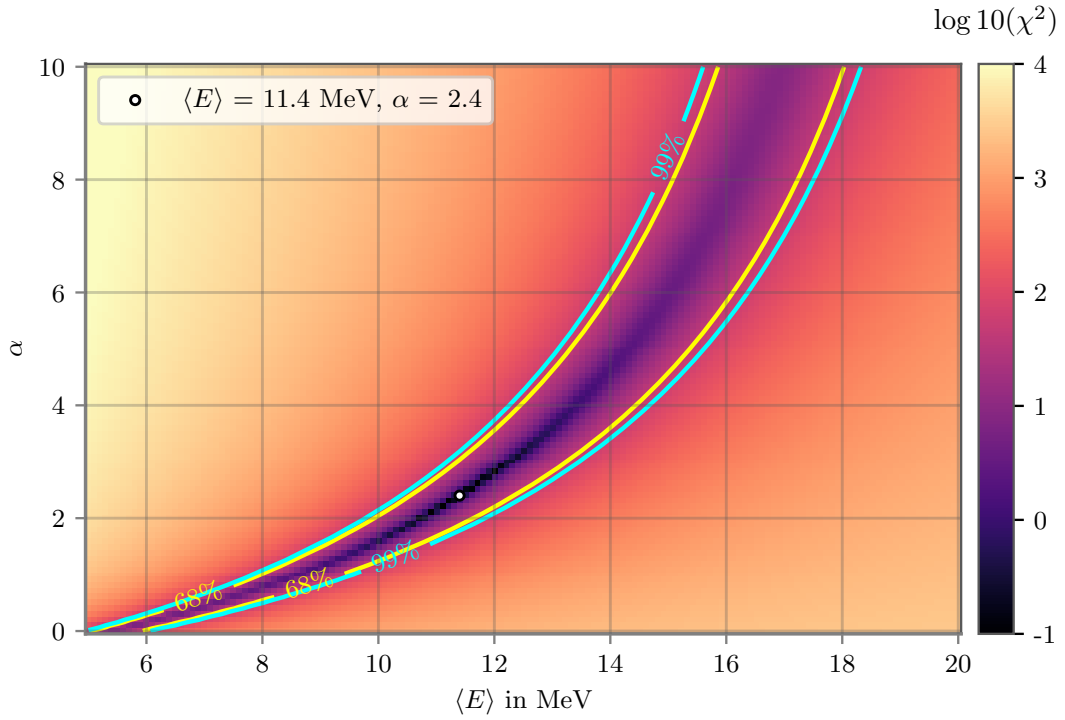

Figure 6.6: Combined χ^2 map of the comparison between the ratios of inter-module coincidence hits with a reference point ($\langle E \rangle = 11.4\,\text{MeV}$,$\alpha = 2.4$, denoted by a white circle) without background for a detector with 500 mDOMs and a SN in 10 kpc distance via a χ^2 method.

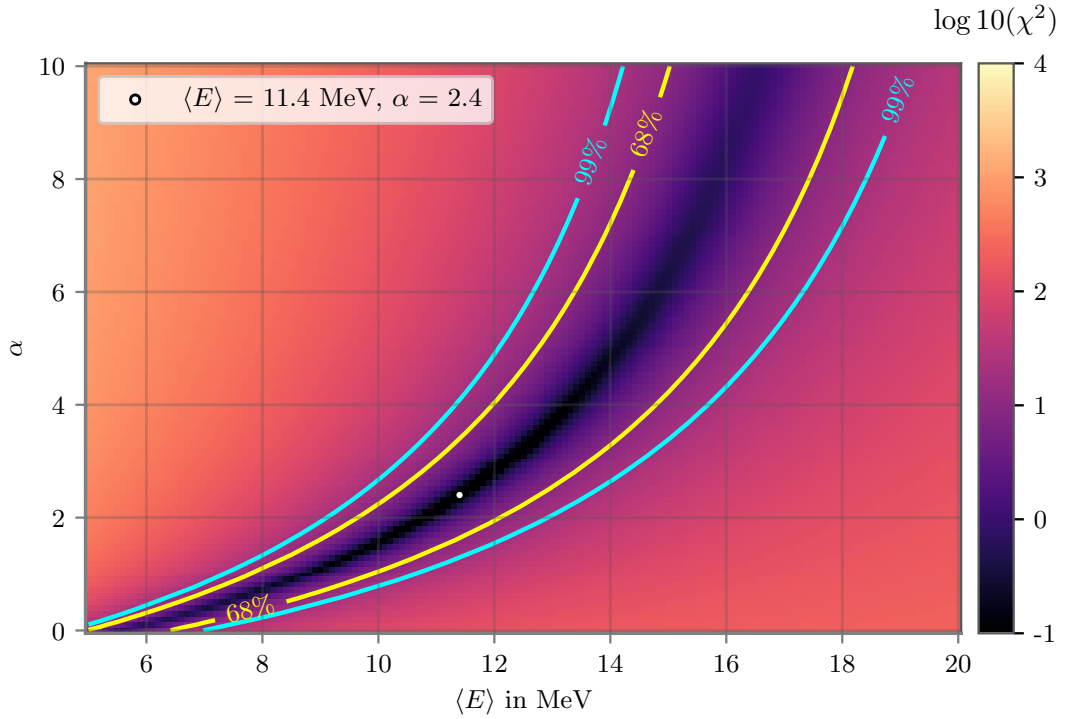

Figure 6.7: Combined χ^2 map of the comparison between the ratios of single mDOM coincidence hits with a reference point ($\langle E \rangle = 11.4\,\text{MeV}$,$\alpha = 2.4$, denoted by a white circle) without background for a detector with 500 mDOMs and a SN in 10 kpc distance via a χ^2 method.

7 Summary & Outlook

This thesis presents studies on the sensitivity of the mDOM to the energy spectrum of MeV SN neutrinos. Since the mDOM provides new features as the possibility of using local coincidences which may result in a better energy resolution than the current IceCube DOM, the potential of the mDOM motivates to investigate its energy resolution towards MeV neutrinos. SN neutrinos are essential for the explosion mechanism of a core-collapse SN and transport a multitude of information from the dense core. The LS220 EoS was used to simulate neutrinos from the SN of a heavy ($27.0\,\mathrm{M}_{\odot}$) progenitor star. The simulation only included electron antineutrinos since those have the highest interaction rate in the South Pole ice for MeV neutrinos.

The energy spectrum of SN neutrinos is described by a function with two parameters: the mean energy $\langle E \rangle$ and the pinching parameter α. The difficulty to investigate the SN neutrino spectrum is therefore to be sensitive to both parameters simultaneously.

The mDOM is one of the modules that will be used for future IceCube extensions as the IceCube-Upgrade and IceCube-Gen2. It provides 24 PMTs in one module which allows local coincidence hits in different PMTs of the same module. These local coincidences were used to distinguish between the SN neutrino energy spectra with different $\langle E \rangle$ and α. It was studied whether all different coincidence hits are taken into account in the simulated volume. To cover all 1-fold and 2-fold coincidence hits, a larger simulated volume would have been implemented which would have increased the simulation time. Another aspect of the simulation are the different neutrinos that could be investigated. Electron antineutrinos covers around 96 % of all neutrino interactions in ice due to its cross section of the Inverse Beta Decay. Nevertheless, a full study would require the simulation of different interactions for all types of neutrinos and antineutrinos.

The mDOM simulations of this thesis used some simplification as it left out the harness around each mDOM and the ropes connecting the mDOMs. The ice was treated as uniform in the simulation what it is not in reality since for the deployment of the modules in the ice a drill hole is required. The ice in this drill holes have different properties than ice layers. The effects of all these simplification should be studied in the future.

As background noise three different types of background were presented: uncorrelated noise from the PMTs, correlated noise from radioactive decays in the mDOM glass vessel, and solar neutrinos which are slightly less energetic than SN neutrinos. The average coincidence rate from these background was assumed to be well known for this study, so that it only influences the uncertainty of the signal, but not the signal itself.

For the investigation of the SN neutrino spectrum, histograms of n-fold coincidence hits of different ($\langle E \rangle$,α) combinations were compared using the ratio of 3-fold coincidence hits divided by the sum of all coincidence hits larger than 4 and a χ^2 method with a reference point of one $\langle E \rangle$, α combination. The χ^2 map showed a degenerated valley of same χ^2.

The degeneracy of that single χ^2 could be prevented by a combination of several χ^2 maps for different rates. By using a marginalization to extract the confidence range for each $\langle E \rangle$, respectively each α, a 68 % confidence interval $\sigma_{\langle E \rangle}$, respectively σ_α could be defined. The combination from $x =$ 2-fold coincidences up to $y \geq$ 9-fold coincidence hits has the smallest $\sigma_{\langle E \rangle}$ and σ_α.

Further investigations were made over the performance of this marginalization method for different SN distances and detector configurations. A $\sigma_{\langle E \rangle}$ and σ_α could be determined within the simulated range of $\langle E \rangle$ and α to a distance of 14.0 kpc and down to 2000 mDOMs. These studies showed that smaller distances have a larger influence on the sensitivity than detectors with a higher amount of mDOMs.

For a detector configuration with 500 modules, which will be constructed in the next years as the IceCube-Upgrade, the degeneracy of the χ^2 valley could not be prevented. But including coincidences in different mDOMs to the local coincidences, the resolution of the χ^2 method was improved. Since the degeneracy could not be prevented in this configuration, one has to assume one parameter, e.g. α, to determine the other one. In the study of inter-module coincidences, the background was still ignored. For future studies, it will be necessary to investigate how radioactive decays influence coincidences in different neighbour mDOMs. With the knowledge of the background a new optimization of the coincidence ratios of the inter-module coincidences can be done.

During the analysis of inter-module coincidences with neighbouring modules there appeared an unsolved riddle of asymmetric ratio maps during the scope of this work. This riddle needs to be investigated further and the hypothesis of influence of asymmetric interaction angles of higher energetic neutrinos needs still to be justified. A method to avoid these asymmetric ratios could be, not to use directly the neighbouring models, but using besides the coincidence hits in PMTs also coincidence hits of mDOMs. A

histogram for this approach is shown in Fig. 7.1. This method could be further studied and compared to the method of neighbouring modules.

Since there are found coincidence hits in mDOM −7 and mDOM 7, it can further be studied up to which mDOM above and below the centered mDOM coincidence hits can be detected. Also coincidence hits in different strings, which are planned in the case of the IceCube-Upgrade to feature a vertical distance of 24 m, might be possible and should be investigated.

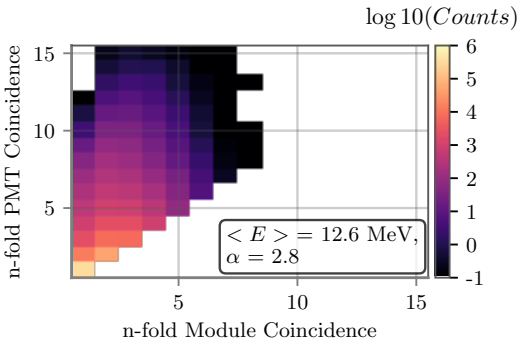

Figure 7.1: Histogram of a different approach for inter-module coincidences using the total number of involved mDOMs.

In these studies only histograms of a single ($\langle E \rangle$,α) combination were investigated. A real SN spectrum consists of a mixture of different $\langle E \rangle$ and α combinations which makes the determination of the average $\langle E \rangle$ and α more complicated. One solution might be to subdivide the total SN burst into smaller phases, e.g. as neutronization burst, accretion phase, and neutrino-driven wind, in which $\langle E \rangle$ and α vary less. The signal for these phases would be smaller which would cause a lower sensitivity, but combining the information of the different phases might increase it. This is something that can be studied in future works.

Bibliography

[1] B. P. Abbott, et al. (Virgo, LIGO Scientific Collaboration), *GW170817: Observation of gravitational waves from a binary neutron star inspiral*, Physical Review Letters 119 (16). URL https://doi.org/10.1103/physrevlett.119.161101

[2] M. G. Aartsen, et al. (Liverpool Telescope, MAGIC, H.E.S.S., AGILE, Kiso, VLA/17B-403, INTEGRAL, Kapteyn, Subaru, HAWC, Fermi-LAT, ASAS-SN, VERITAS, Kanata, IceCube, Swift NuSTAR Collaboration), *Multimessenger observations of a flaring blazar coincident with high-energy neutrino IceCube-170922a*, Science 361 (6398) (2018) 146. URL https://doi.org/10.1126/science.aat1378

[3] M. G. Aartsen, et al. (IceCube Collaboration), *Neutrino emission from the direction of the blazar TXS 0506+056 prior to the IceCube-170922a alert*, Science 361 (6398) (2018) 147–151. URL https://doi.org/10.1126/science.aat2890

[4] K. Hirata, et al. (Kamiokande-II Collaboration), *Observation of a neutrino burst from the supernova SN1987a*, Physical Review Letters 58 (14) (1987) 1490–1493. URL https://doi.org/10.1103/physrevlett.58.1490

[5] R. M. Bionta, et al., *Observation of a neutrino burst in coincidence with supernova 1987a in the large magellanic cloud*, Physical Review Letters 58 (14) (1987) 1494–1496. URL https://doi.org/10.1103/physrevlett.58.1494

[6] E. N. Alekseev, et al., *Detection of the neutrino signal from SN 1987A using the INR Baksan underground scintillation telescope*, in: I. J. Danziger (Ed.), European Southern Observatory Conference and Workshop Proceedings, Vol. 26 of *European Southern Observatory Conference and Workshop Proceedings*, 1987, pp. 237–247.

[7] K. Scholberg, *Supernova neutrino detection*, Annual Review of Nuclear and Particle Science 62 (1) (2012) 81–103. URL https://doi.org/10.1146/annurev-nucl-102711-095006

[8] A. Bellerive, *Review of solar neutrino experiments*, International

Journal of Modern Physics A 19 (08) (2004) 1167–1179. URL https://doi.org/10.1142/s0217751x04019093

[9] P. Antonioli, et al., *SNEWS: the SuperNova early warning system*, New Journal of Physics 6 (2004) 114–114. URL https://doi.org/10.1088/1367-2630/6/1/114

[10] L. Classen, *Prototyping a novel optical module for the icecube-gen2 neutrino telescope*, Ph.D. thesis, Friedrich-Alexander-Universität Erlangen-Nürnberg (2017). URL https://www.uni-muenster.de/imperia/md/content/physik_kp/agkappes/abschlussarbeiten/doktorarbeiten/1702-phd_lclassen.pdf

[11] M. Tanabashi, et al. (Particle Data Group Collaboration), *Review of particle physics*, Physical Review D 98 (3). URL https://doi.org/10.1103/physrevd.98.030001

[12] H.-T. Janka, *Neutrino-driven explosions*, in: Handbook of Supernovae, Springer International Publishing, 2017, pp. 1095–1150. URL https://doi.org/10.1007/978-3-319-21846-5_109

[13] J. Chadwick, *The existence of a neutron*, Proceedings of the Royal Society A: Mathematical, Physical and Engineering Sciences 136 (830) (1932) 692–708. URL https://doi.org/10.1098/rspa.1932.0112

[14] L. M. Brown, *The idea of the neutrino*, Physics Today 31 (9) (1978) 23–28. URL https://doi.org/10.1063/1.2995181

[15] C. L. Cowan, et al., *Detection of the free neutrino: a confirmation*, Science 124 (3212) (1956) 103–104. URL https://doi.org/10.1126/science.124.3212.103

[16] G. Danby, et al., *Observation of high-energy neutrino reactions and the existence of two kinds of neutrinos*, Physical Review Letters 9 (1) (1962) 36–44. URL https://doi.org/10.1103/physrevlett.9.36

[17] K. Kodama, et al. (DONUT Collaboration), *Observation of tau neutrino interactions*, Physics Letters B 504 (3) (2001) 218–224. URL https://doi.org/10.1016/s0370-2693(01)00307-0

[18] S. P. Mikheyev, A. Y. Smirnov, *Resonant amplification of* ν *oscillations in matter and solar-neutrino spectroscopy*, Il Nuovo Cimento C 9 (1) (1986) 17–26. URL https://doi.org/10.1007/bf02508049

[19] Y. Suzuki, *Solar neutrinos*, International Journal of Modern Physics A 15 (supp01a) (2000) 201–228. URL https://doi.org/10.1142/s0217751x00005164

[20] U. Katz, C. Spiering, *High-energy neutrino astrophysics: Status and*

perspectives, Progress in Particle and Nuclear Physics 67 (3) (2012) 651–704. URL https://doi.org/10.1016/j.ppnp.2011.12.001

[21] M. G. Aartsen, et al. (IceCube Collaboration), *First observation of PeV-energy neutrinos with IceCube*, Physical Review Letters 111 (2). URL https://doi.org/10.1103/physrevlett.111.021103

[22] M. G. Aartsen, et al. (IceCube Collaboration), *Atmospheric and astrophysical neutrinos above 1 TeV interacting in IceCube*, Physical Review D 91 (2). URL https://doi.org/10.1103/physrevd.91.022001

[23] G. Eder, *Terrestrial neutrinos*, Nuclear Physics 78 (3) (1966) 657–662. URL https://doi.org/10.1016/0029-5582(66)90903-5

[24] R. A. Serway, J. W. Jewett, Physics for Scientists and Engineers with Modern Physics -, 9th Edition, Cengage Learning, Clifton Park, NY, 2013.

[25] S. Ekström, et al., *Grids of stellar models with rotation*, Astronomy & Astrophysics 537 (2012) A146. URL https://doi.org/10.1051/0004-6361/201117751

[26] S. Woosley, T. Janka, *The physics of core-collapse supernovae*, Nature Physics 1 (3) (2005) 147–154. URL https://doi.org/10.1038/nphys172

[27] S. E. Woosley, A. Heger, *The deaths of very massive stars*, in: Very Massive Stars in the Local Universe, Springer International Publishing, 2014, pp. 199–225. URL https://doi.org/10.1007/978-3-319-09596-7_7

[28] H.-T. Janka, other, *Theory of core-collapse supernovae*, Physics Reports 442 (1-6) (2007) 38–74. URL https://doi.org/10.1016/j.physrep.2007.02.002

[29] H. A. Bethe, *Supernova mechanisms*, Reviews of Modern Physics 62 (4) (1990) 801–866. URL https://doi.org/10.1103/revmodphys.62.801

[30] H. A. Bethe, J. R. Wilson, *Revival of a stalled supernova shock by neutrino heating*, The Astrophysical Journal 295 (1985) 14. URL https://doi.org/10.1086/163343

[31] L. Walk, et al., *Identifying rotating core-collapse supernovae with a neutrino gyroscope*, ArXiv e-prints Preprint 1807.02366.

[32] T. Sukhbold, T. Ertl, S. E. Woosley, J. M. Brown, H.-T. Janka, *Core-collapse supernovae from 9 to 120 solar masses based on neutrino-*

powered explosions, The Astrophysical Journal 821 (1) (2016) 38. URL https://doi.org/10.3847/0004-637x/821/1/38

[33] J. M. Lattimer, F. D. Swesty, *A generalized equation of state for hot, dense matter*, Nuclear Physics A 535 (2) (1991) 331–376. URL https://doi.org/10.1016/0375-9474(91)90452-c

[34] S. E. Woosley, T. A. Weaver, *The evolution and explosion of massive stars. II. explosive hydrodynamics and nucleosynthesis*, The Astrophysical Journal Supplement Series 101 (1995) 181. URL https://doi.org/10.1086/192237

[35] I. Tamborra, B. Müller, L. Hüdepohl, H.-T. Janka, G. Raffelt, *High-resolution supernova neutrino spectra represented by a simple fit*, Physical Review D 86 (12). URL https://doi.org/10.1103/physrevd.86.125031

[36] M. T. Keil, G. G. Raffelt, H.-T. Janka, *Monte carlo study of supernova neutrino spectra formation*, The Astrophysical Journal 590 (2) (2003) 971–991. URL https://doi.org/10.1086/375130

[37] C. Giunti, C. W. Kim, Fundamentals of neutrino physics and astrophysics, Oxford University Press, 2015.

[38] P. Vogel, J. F. Beacom, *Angular distribution of neutron inverse beta decay, $\bar{\nu}_e + p \rightarrow e^+ + n$*, Physical Review D 60 (5). URL https://doi.org/10.1103/physrevd.60.053003

[39] R. Abbasi, et al. (IceCube Collaboration), *IceCube sensitivity for low-energy neutrinos from nearby supernovae*, Astronomy & Astrophysics 535 (2011) A109. URL https://doi.org/10.1051/0004-6361/201117810

[40] P. A. Cherenkov, *Visible emission of clean liquids by action of γ radiation*, Doklady Akademii Nauk SSSR 2 (1934) 451+. URL http://ufn.ru/en/articles/2007/4/g/

[41] J. V. Jelley, Cerenkov Radiation and its Application, Pergamon, 1958.

[42] C. Grupen, *Astroparticle Physics*, Springer, 2005.

[43] M. G. Aartsen, et al. (IceCube Collaboration), *The IceCube neutrino observatory: instrumentation and online systems*, Journal of Instrumentation 12 (03) (2017) P03012–P03012. URL https://doi.org/10.1088/1748-0221/12/03/p03012

[44] *Icecube gallery*, https://gallery.icecube.wisc.edu/internal/main.php, accessed: 05.12.2018.

[45] R. Abbasi, et al. (IceCube Collaboration), *The IceCube data acquisi-*

tion system: Signal capture, digitization, and timestamping, Nuclear Instruments and Methods in Physics Research Section A: Accelerators, Spectrometers, Detectors and Associated Equipment 601 (3) (2009) 294–316. URL https://doi.org/10.1016/j.nima.2009.01.001

[46] R. Abbasi, et al., *The design and performance of IceCube DeepCore*, Astroparticle Physics 35 (10) (2012) 615–624. URL https://doi.org/10.1016/j.astropartphys.2012.01.004

[47] R. Abbasi, et al., *IceTop: The surface component of IceCube*, Nuclear Instruments and Methods in Physics Research Section A: Accelerators, Spectrometers, Detectors and Associated Equipment 700 (2013) 188–220. URL https://doi.org/10.1016/j.nima.2012.10.067

[48] M. G. Aartsen, et al. (IceCube Collaboration), *Evidence for high-energy extraterrestrial neutrinos at the IceCube detector*, Science 342 (6161) (2013) 1242856–1242856. URL https://doi.org/10.1126/science.1242856

[49] F. Halzen, S. R. Klein, *Invited review article: IceCube: An instrument for neutrino astronomy*, Review of Scientific Instruments 81 (8) (2010) 081101. URL https://doi.org/10.1063/1.3480478

[50] L. Hüdepohl, B. Müller, H.-T. Janka, A. Marek, G. G. Raffelt, *Neutrino signal of electron-capture supernovae from core collapse to cooling*, Physical Review Letters 104 (25). URL https://doi.org/10.1103/physrevlett.104.251101

[51] L. Köpke (IceCube Collaboration), *Improved detection of supernovae with the IceCube observatory*, Journal of Physics: Conference Series 1029 (2018) 012001. URL https://doi.org/10.1088/1742-6596/1029/1/012001

[52] T. Mühlbeier, H. Nunokawa, R. Z. Funchal, *Revisiting the triangulation method for pointing to supernova and failed supernova with neutrinos*, Physical Review D 88 (8). URL https://doi.org/10.1103/physrevd.88.085010

[53] S. Bravo (IceCube Collaboration), *Icecube upgrade for precision neutrino physics and astrophysics kicks off*. URL https://icecube.wisc.edu/news/view/605

[54] M. G. Aartsen, et al. (IceCube-Gen2 Collaboration), *Icecube-gen2: A vision for the future of neutrino astronomy in antarctica* Preprint 1412.5106.

[55] S. Adrián-Martínez, et al., *Letter of intent for KM3net 2.0*, Journal of Physics G: Nuclear and Particle Physics 43 (8) (2016) 084001. URL https://doi.org/10.1088/0954-3899/43/8/084001

[56] T. Eder, *Studies on an in-situ calibration method for the icecube multi-pmt optical module using radioactive decays*, to be published (jan 2019).

[57] C. J. Lozano Mariscal, *Studies on the sensitivity of multi-pmt optical modules to supernova neutrinos in the south pole ice* (2017). URL https://www.uni-muenster.de/imperia/md/content/physik_kp//agkappes/abschlussarbeiten/masterarbeiten/1702-ma_clozano.pdf

[58] C. J. Lozano Mariscal, *Sensitivity of multi-pmt optical modules to mev supernova neutrinos in south pole ice*. URL https://zenodo.org/record/1300863

[59] S. Agostinelli, et al. (Geant4 Collaboration), *Geant4—a simulation toolkit*, Nuclear Instruments and Methods in Physics Research Section A: Accelerators, Spectrometers, Detectors and Associated Equipment 506 (3) (2003) 250–303. URL https://doi.org/10.1016/s0168-9002(03)01368-8

[60] B. Herold, *Simulation and measurement of optical background in the deep sea using a multi-pmt optical module*, Ph.D. thesis, Friedrich-Alexander-Universität Erlangen-Nürnberg (2017).

[61] Geant4 (Geant4 Collaboration), *Introduction to Geant4*. URL http://geant4-userdoc.web.cern.ch/geant4-userdoc/UsersGuides/IntroductionToGeant4/fo/IntroductionToGeant4.pdf

[62] M. Ackermann, other, *Optical properties of deep glacial ice at the south pole*, Journal of Geophysical Research 111 (D13). URL https://doi.org/10.1029/2005jd006687

[63] M. Aartsen, et al. (IceCube Collaboration), *Measurement of south pole ice transparency with the IceCube LED calibration system*, Nuclear Instruments and Methods in Physics Research Section A: Accelerators, Spectrometers, Detectors and Associated Equipment 711 (2013) 73–89. URL https://doi.org/10.1016/j.nima.2013.01.054

[64] K. Woschnagg, P. B. Price, *Temperature dependence of absorption in ice at 532 nm*, Applied Optics 40 (15) (2001) 2496. URL https://doi.org/10.1364/ao.40.002496

[65] G. Mie, *Beiträge zur optik trüber medien, speziell kolloidaler metallösungen*, Annalen der Physik 330 (3) (1908) 377–445. URL https://doi.org/10.1002/andp.19083300302

[66] S. Böser, M. Kowalski, L. Schulte, N. L. Strotjohann, M. Voge, *Detecting extra-galactic supernova neutrinos in the antarctic ice*,

Astroparticle Physics 62 (2015) 54–65. URL https://doi.org/10.1016/j.astropartphys.2014.07.010

[67] R. J. Barlow, Statistics: A Guide to the Use of Statistical Methods in the Physical Sciences (Manchester Physics Series), John Wiley & Sons, New York, 1989.

[68] M. A. Unland Elorrieta, *Studies on dark rates induced by radioactive decays of the multi-pmt digital optical module for future icecube extensions* (2018). URL https://www.uni-muenster.de/imperia/md/content/physik_kp/agkappes/abschlussarbeiten/masterarbeiten/1712-ma_munland.pdf

[69] M. A. Unland Elorrieta, *Dark rates induced by radioactive decays in optical modules for neutrino telescopes*. URL https://zenodo.org/record/1300859

[70] J. N. Bahcall, et al., *Standard neutrino spectrum fromB8decay*, Physical Review C 54 (1) (1996) 411–422. URL https://doi.org/10.1103/physrevc.54.411

[71] T. Glüsenkamp, *Probabilistic treatment of the uncertainty from the finite size of weighted monte carlo data*, The European Physical Journal Plus 133 (6). URL https://doi.org/10.1140/epjp/i2018-12042-x

[72] R. Bruijn, *Supernova detection in IceCube: Status and future*, Nuclear Physics B - Proceedings Supplements 237-238 (2013) 94–97. URL https://doi.org/10.1016/j.nuclphysbps.2013.04.065

Acknowledgements

Firstly I want to say “Thank you!” to Prof. Dr. Alexander Kappes for giving me the opportunity to do my research for this thesis in his working group and within the IceCube collaboration in these exciting times for multi-messenger astronomy.

The whole AG Kappes deserves my gratitude for the poker and durak breaks, the game nights, DPG and astroparticle physics meeting, and of course the critical input to all my work.

Thank you Cris for helping me with stupid questions and helpful discussions about my work. Furthermore I want to thank Daniel, Lew, Martin, Markus, and once more Cris for giving their time to read the first draft of my thesis and their input in it.

我要感谢我的小花，以提高我的语言技能，当然尤其是英语。

Ich möchte meinem Bruder herzlich dafür danken, dass er mir seit meinen jüngsten Jahren verschiedenste Orte zeigt und in mir das Fernweh zu verschiedenen Kulturen entfacht hat.

Meiner Schwester gebürt der Dank für das Versprühen ihres optimistischen Lebensmuts, der ganze Räume erfüllt, sobald sie diese auch nur betritt.

Ich möchte meiner Mutter und meinem Vater einen ganz besonderen Dank zukommen lassen: für ihre nie endende Unterstützung und ihre stete Geduld.

Vielen Dank!

Declaration

I, Florian Sprenger, declare that this thesis titled, "Studies on the Sensitivity of Multi-PMT Optical Modules to the Energy Spectrum of MeV Supernova Neutrinos for Future IceCube Extensions" and the work presented in it are my own. I confirm that:

- This work was done wholly or mainly while in candidature for a research degree at this University.
- Where any part of this thesis has previously been submitted for a degree or any other qualification at this University or any other institution, this has been clearly stated.
- Where I have consulted the published work of others, this is always clearly attributed.
- Where I have quoted from the work of others, the source is always given. With the exception of such quotations, this thesis is entirely my own work.
- I have acknowledged all main sources of help.
- Where the thesis is based on work done by myself jointly with others, I have made clear exactly what was done by others and what I have contributed myself.

Münster,

_____